UNIVERSITA' DEGLI STUDI DI PADOVA

DIPARTIMENTO DI INGEGNERIA INDUSTRIALE

CORSO DI LAUREA MAGISTRALE IN INGEGNERIA DEI MATERIALI

Tesi di Laurea Magistrale in

Ingegneria dei Materiali

A STUDY OF MIXED-MODE PARTITIONING OF A CRACK IN UNIDIRECTIONAL CARBON FIBRE REINFORCE PLASTICS USING MODE DECOMPOSED INTEGRATION (J-INTEGRAL) AND DIGITAL IMAGE CORRELATION (DIC)

Relatore: ***Prof. Massimo Guglielmi***

Correlatori: ***Prof. Alojz Ivankovic***

Dr. Clemence Rouge

Laureando: Riccardo Bonato

ANNO ACCADEMICO 2016 - 2017

UNIVERSITA' DEGLI STUDI DI PADOVA

DIPARTIMENTO DI INGEGNERIA INDUSTRIALE

CORSO DI LAUREA MAGISTRALE IN INGEGNERIA DEI MATERIALI

Tesi di Laurea Magistrale in

Ingegneria dei Materiali

A STUDY OF MIXED-MODE PARTITIONING OF A CRACK IN UNIDIRECTIONAL CARBON FIBRE REINFORCE PLASTICS USING MODE DECOMPOSED INTEGRATION (J-INTEGRAL) AND DIGITAL IMAGE CORRELATION (DIC)

Relatore: ***Prof. Massimo Guglielmi***

Correlatori: ***Prof. Alojz Ivankovic***

Dr. Clemence Rouge

Laureando: Riccardo Bonato

ANNO ACCADEMICO 2016 - 2017

Abstract

In this Thesis is described the work that I did at University College Dublin, School of Materials and Mechanical Engineering as part of my MSc final year project. The work regarded the determination of the mode decomposed fracture toughness of unidirectional carbon fibre reinforced plastics using an innovative approach based on the determination of the displacement, strain and stress fields using Digital Image Correlation. The exact mode partition is known for symmetric samples, and can be determined accurately thanks to the standard tests. On the other hand, the partition of the fracture energy is not known for asymmetric samples. Many partitioning theories have been proposed over the last decades but, while they all agree in the symmetric cases, they give significantly different results in the asymmetric ones. The usage of the Digital Image Correlation for the determination of the displacement, strain and stress fields and the application of the mode decomposed J-integral would allow the determination of the exact mode partition, both for symmetric and asymmetric cases.

Contents

List of Figures

List of Tables

Introduction

As it was reported in the Abstract, I did this work as part of my final year project during the Erasmus+ mobility programme in Dublin. Two years ago I chose to do the BSc Thesis in a factory, since I was really interested in doing something practical. This time I opted for a university because I wanted to combine the desire of spending a period abroad with the understanding of what doing academic research means. The topic, which was assigned to me by my supervisor in Dublin professor Alojz Ivankovic, regarded the determination of the mode decomposed fracture toughness of unidirectional carbon fibre reinforced plastics. The standard tests allow to calculate precisely the total toughness and the mode mixity for symmetric samples, while for the asymmetic cases the mode partition is not known exactly. The idea under the project is to perform the standard test using simultaneusly the Digital Image Correlation which should allow to obtain displacement and strain fields and thus, knowing the materials' properties, the stress field. After this, all these data should be fed into a code which implements the mode decomposed J-integral therefore obtaining the mode decomposed fracture toughness. Of course the first thing to do is to work with symmetric samples and, if the results from this alternative approach are compatible with those from the standard tests, then the experiment could be extended to the asymmetric cases. While the numerical and simulation parts of this Thesis were carried out with not too many troubles, the experimental one turned out to be much more challenging. The Digital Image Correlation machine, which was new almost for everyone in the group, proved to be very difficult to use. We (my co-supervisor Clemence and I) faced and had to overcome a number of issues before obtaining something with a minimum of physical significance. Furthermore, the strains that we had to pick up were very small (i.e. three or four times the accuracy of the machine). For these reasons (and for many others, including that my time in Dublin couldn't be extended), I was not able to complete the work as in its initial plan. However, I'm very happy of what I did, maybe I didn't obtain very good results but I learnt a lot of things among which working autonomously, confronting with other people and managing the stress when everything seems to go wrong.

Chapter 1

Composite Materials

This chapter gives an introduction on composite materials. First the definition of composite material and a brief historical background are given. Then a classification is proposed and some important features are outlined. The focus is then turned on a particular class of composite materials (the FRP, Fiber Reinforced Plastics). Their industrial applications and main limitations are outlined.
The vast majority of the information provided in this chapter are taken from [1].

1.1 Definition and History

A composite material is a material where two or more materials are combine together on a *macroscopic* scale to form a third material. This means that it is always possible to distinguish by naked eye the various components. Several materials can be combined on a microscopic scale (e.g. metal alloys) but the result is, from a macroscopic point of view, that of an homogenous material.
The advantage of composite material is that they can be designed to exhibit the best qualities of their components such as strength, stiffness, weight, fatigue resistance, thermal and acoustical insulation ... Anyway not all these properties can be improved at the same time because some of them are in conflict with others.
Composite materials have long been used, and the period when they were first introduced cannot be established with accuracy. Nevertheless there are evidences that the Israelites used straw to strengthen mud bricks, and the ancient Egyptians, driven by the lacking of high quality wood, produced plywood [2]. Plywood was manufactured by cutting the wood into very thin sheets called "veneers" which were spread with an adhesive (i.e. an animal glue) and overlaid in two different orientations. Pressure was also applied during the process thanks to sandbag weights. The product was a panel with a superior strength and a good resistance to thermal expansion as well as to swelling caused by absorption of moisture. Even in the Middle Ages, composite materials were used: swords and armour were constructed with layers of different metals. An intriguing example is that one of the swords made in Damasco, whose blades were famous for being very tough. This characteristic arises from the particular manufacturing process

that these swords underwent. The blades were produced by stacking alternating layers of high and low carbon steel sheets and then by forge-welding them together [3]. Nowadays fibre-reinforced, resin-matrix composite materials are the most commonly used especially for airplanes and space vehicles.

1.2 Classification

There are several criteria that can be used to classify the types composite materials. In this work the criterion that takes into account the various constituents is used. Therefore, there are four commonly accepted types of composite materials

1. fibrous, that consist of fibre in a matrix;
2. laminated, that consist of layers of various materials;
3. particulate, that are composed of particles in a matrix;
4. combinations of the first three types.

For this work, only the types 1 and 2 are of some interest and will thus be discussed.

1.2.1 Fibrous Composite Materials

A certain material in the form of a fibre is much stiffer and stronger than in the bulk form. This is due to the fact that during the manufacturing process, the crystals are aligned along the fibre axis and therefore the fibre has a "more perfect" structure. Moreover, there are fewer internal defects in fibres than in bulk materials.
As told, fibres have in general better properties than the corresponding bulk materials. Now, if we consider the density, stiffness and tensile strength of the most common structural materials (i.e. steel and aluminium), we can see that the fibres have higher values of $\frac{E}{\rho}$ and $\frac{\sigma}{\rho}$ (Table 1.1), and this is of much great importance in weight sensitive applications such as aircrafts and space vehicles. In particular carbon fibres are of high interest in today's structures. They are made from rayon, pitch or PAN (Polyacrylonitrile) precursor fibres that are heated up to 1700 °C in an inert atmosphere in order to carbonize.
Naturally, fibres are of little use unless they are bonded together to the form of a structural element that can bear loads. The binder material is called matrix and it can be a polymer, a metal, a ceramic or carbon. The purpose of the matrix is manifold:

- support the fibres;
- protect the fibres;
- transfer the stress between broken fibres.

Table 1.1: Specific stiffness and strength for aluminium and steel wires and for glass and carbon fibres. Indicative values.

Fiber or Wire	$\frac{E}{\rho}$ [Mm]	$\frac{\sigma}{\rho}$ [km]
aluminium	$2,8$	24
steel	$2,7$	54
E-glass	$2,9$	136
carbon	14	123

Normally the matrix has a lower density, stiffness and strength than the fibres. However, the combination of fibre and matrix can lead to a material with high stiffness and strength, yet maintaining a low density.

1.2.2 Laminated Composite Materials

The basic building block of a laminate is the lamina, which is a flat arrangement of unidirectional fibres in a matrix. Regarding the stress-strain relationship, fibres generally exhibit a linear elastic behaviour while ceramic, polymeric and metallic matrices exhibit a elastic, viscoelastic and elastic-plastic behaviour respectively. Obviously there are some exceptions: reinforcing steel bars in concrete are more nearly elastic-perfectly plastic rather than linear elastic. Anyway only carbon-epoxy composite materials will be treated in this work and for them the assumption of an overall linear elastic behaviour is a good approximation (even tough some plasticity can occur for example at cracks' tips).
A laminate is a bonded stack of laminae with various orientations of principal material directions in the laminae. The fibre orientation of the layers can be symmetric or not about the middle surface of the laminate. The result is a symmetric and asymmetric laminate respectively. Usually the layers of a laminate are bonded together by the same matrix material that is used in the individual laminae. That is, some of the matrix material material in a lamina coats the surface of a lamina, and is used to bond the lamina to its adjacent laminae without the addition of more matrix material.
A major purpose of lamination is that it is possible to design a laminate with an higher strength and stiffness in a certain direction simply by orienting more laminae in that direction. Regarding this, it is important to point up that, given a certain number of laminae and their orientation, also the position those laminae in the thickness of the laminate has a great influence on the properties of the laminate itself. Anyway this topic lies outside the aim of this brief introduction. For further details please refer to [4].

1.3 FRP Composites

Concrete is, without any doubt, the most used composite material but probably not the most famous. In fact, when someone refers generally to a composite material, most of the times he is thinking to a material mede of fibres embedded in a polymeric matrix. This is exactly the definition of what FRP (Fiber Reinforced Plastics) are. A particular type of FRP are the so called "advanced fibre reinforced composite materials". The term "advanced" is used to distinguish this materials which have ultrahigh strength and stiffness and low density (e.g. carbon-epoxy) from those which, although having an improved strength and stiffness and low density as well, are considered more common (e.g. glass-polyester). For the advantages that they can potentially lead to, the advent of advanced fibre reinforced composite materials has been compared with the invention of the jet engine. This claim is amazing since the introduction of the jet engine completely revolutionized military and commercial aviation: superior performance and flying range with lower maintenance costs. However, the aerospace industry was attracted in the 1950's by titanium for reasons similar to those that now induce them to invest in the development of composite materials. After having spent a lot of money on research several problems emerged, and titanium was partially given up. That unfortunate experience with titanium caused a more cautious, yet more complete and well balanced approach to composite materials development. Anyway the advantages of the using of advanced fibre reinforced composite materials are undeniable, and the research is progressing continuously.
The following subsections describe the advantages and the main limitations of these materials. The applications will instead be discussed in a dedicated paragraph.

1.3.1 Advantages

The main advantages that arise from the use of advance fibre reinforced composite materials are three:

- strength and stiffness;
- cost;
- weight.

However, there are also others, such as an improved fatigue life and a very good corrosion resistance.

1.3.1.1 Strength and Stiffness Advantages

Typically, the fibres used in advanced composite materials are very high in strength and stiffness (modulus). On the other hand matrices are, in general, low in strength and stiffness. Suppose that we put those fibres into a matrix. What we obtain is a unidirectionally reinforced lamina. Such a lamina exhibits a strength and a stiffness that is more like the fibres in the fibres' direction (0°)

and more like the matrix in the direction normal to that of the fibres (90°). For a laminate, which is a stack of variously angled laminae bonded together, we expect values of strength and stiffness between those one of the 0° and 90° of the lamina. As mentioned in §1.2.1, one of the most common ways of expressing the effectiveness of strength or stiffness of a material is as a ratio of either of these quantities to the density. Specific strength and specific stiffness or modulus (as the ratio between strength and density and stiffness and density are called respectively) are of particular interest in weight sensitive applications such as aircraft and spacecraft. Figure 1.1 shows these properties for different materials under various forms: buck structural metals (open squares), fibres (open circles), laminae with unidirectional fibres (circles with a vertical line) and laminae with an equal fraction of fibres in two perpendicular directions (circles with a horizontal and a vertical line).
Given that the most effective material should lie in the upper right-hand corner, fibres alone seem to exhibit the best properties. Anyway we know that fibres are never used without a matrix. From the same picture we can see that unidirectional laminae are stiffer and stronger then laminae with fibres in two perpendicular directions. From this evidence we could think to use unidirectional laminates in all the applications. This is not correct. For example when designing aircraft wings fibres must have multiple orientation in order to achieve the proper strength and stiffness necessary to accommodate loads from various directions. In other words, we can taylor the layup of a laminate in order optimize the strength and the stiffness in the direction that we desire.
In Figure 1.1 a wide variety of materials are also depicted. It is evident that graphite-epoxy composite can be used in a stiffness critical application, while glass-epoxy can be used in a strength critical application.
In conclusion it is important to point up the duality of the plot in Figure 1.1: stiffness and strength are equally important.

1.3.1.2 Cost Advantages

Carbon fibres have experienced, since their introduction, a continuous decrease of their cost thanks to the development of new and more efficient manufacturing processes. In the early 1970s carbon fibres cost about 700 $/kg. In the 1990s the cost decreased to 40 $/kg and in 2015 was about 21 $/kg [1] and [5]. These prices refer to commercial grade carbon fibres, aerospace grade carbon fibres cost more (about 85 $/kg in 2014 according to [5]).
Carbon fibres are, with epoxide resin, the raw materials necessary for manufacturing carbon-epoxy composites. The costs previously reported are thus only the costs of the raw material which is only one small element in the whole process of determining the true cost of an object. In fact, the life-cycle cost of an object is made up of initial cost (i.e. raw material, design, fabrication, assembly) plus others such as operating cost and maintenance cost. The Figure clarifies this concept. Therefore, using only the raw material cost or the initial cost to make a decision is misleading: operating and maintenance costs must be taken into account as well.

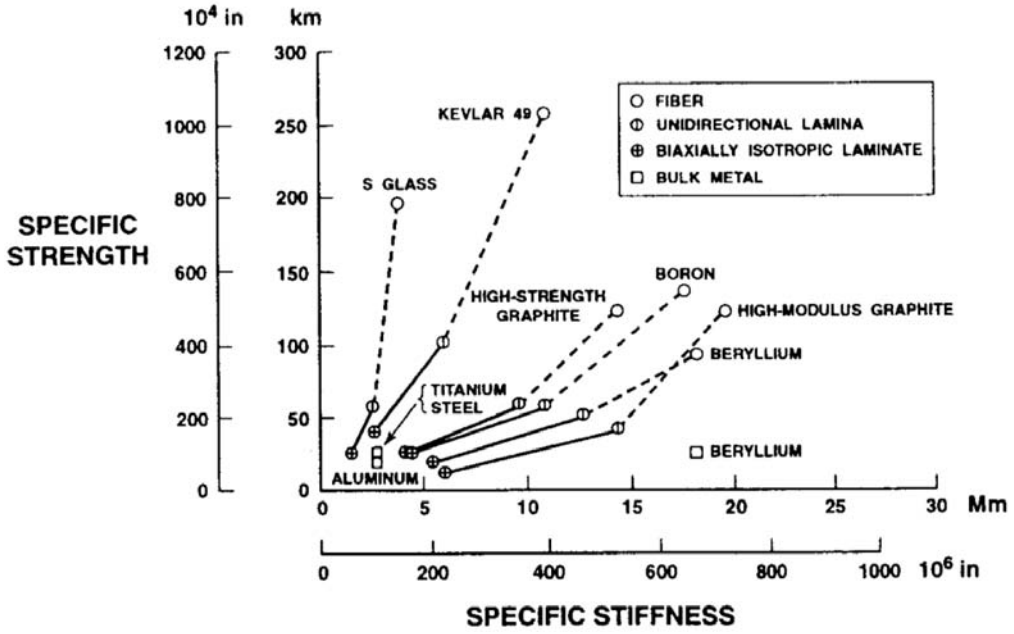

Figure 1.1: Specific strength vs specific stiffness for some materials.

The operating costs are generally lower for composite structures than for metallic ones. Thus we can afford to pay more for the initial cost of the composite structure in order to achieve those lower operating costs.
Of course the key criterion is the life-cycle cost that takes into account also another factor which wasn't mention before: the salvage value. When an object comes to the end of its life it must be disposed. If this object (e.g. an airplane) is made of aluminium, the metal can be recycled and so there is a certain salvage value; if instead it is made of a carbon-epoxy composite material nothing can be recycled because once that the resin has been cured it maintain the shape permanently and cannot be melted or softened. However, even the salvage value of aluminium aircraft is not enough higher than zero relative to the initial cost to make the salvage value a strong consideration in the overall economic analysis.
In conclusion we can say that a composite material might appear very efficient when expressed in terms of weight, but we must also think of the cost. We have already said that composite materials have an higher raw material cost but, in general, lower operating cost. But there is more. The manufacturing processes involved for the fabrication of composite structures are simpler as compared to those for metal structures. Furthermore, the Materials Utilization Factor (Materials Utilization Factor $= \frac{\text{raw material weight}}{\text{final part weight}}$) is lower for composite materials (about 1.2 or 1.3) and higher for metal ones. This is because metals are often carved down from a big chunk to the final shape while composite materials are normally built up until the desired geometry is reached. This means that usually less material is needed for building a structure with a composite material rather then with metals. Both these factors make the usage of composite materials cheaper (and increasingly cheaper) than the usage of metals.

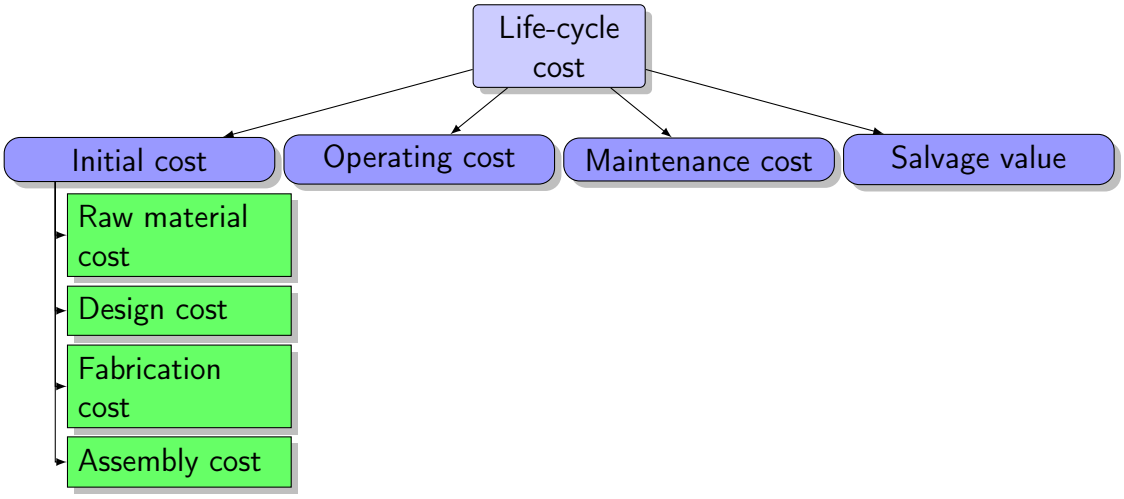

Figure 1.2: Contributions to the life-cycle cost of an object

1.3.1.3 Weight Advantages

Many are the advantages that arise from saving weight in a structure. Let us consider an aircraft or a truck. If we save a certain weight, we need less fuel for a given travel. Else, we can carry more fuel thus increasing the range of the airplane or truck, or the load that it can carry, or a combination of those two. But there is more. In fact, if we decrease the weight of a part of an airplane, we need a lower wing area, a lower engine thrust and a smaller tank. So the weight saving of the overall structure will be much grater than the weight saving of the part itself. For example, for a fighter, a 0.45 kg decrease in a part, can lead to a 1.13 kg total weight decrease. In aircraft industry, composite materials were first applied to secondary structures (those which, upon their failure, don't cause the failure of the whole structure). This lead to 10% structural weight saving. Nowadays also composite primary structures (those which, upon their failure, cause the failure of the whole structure) have been developed. This could lead up to a 30% structural weight saving.

1.3.1.4 Limitations

The advantages that arise from the usage of advanced composite materials have been deeply described in the above paragraph. Naturally there are also some disadvantages, some of which have already been mentioned. Without being exhaustive, here is a list of the most important ones [6]:

- high raw material and (sometimes) fabrication (especially lay-up) cost;
- adverse effects of both temperature and moisture;
- poor strength in the out-of-plane direction where the matrix carries the primary load;

- susceptibility to impact damage and delamination or ply separations;
- greater difficulty in repairing them compared to metallic structures.

Several studies have been carried on which aim to quantify and/or improve these disadvantages while keeping the benefits intact, and this work, with all its defects, can be categorised, to some extent, as one of them.

1.4 Applications

The most known application of composite material is in the aerospace field. However applications include also transportation, construction, marine goods, sporting goods and infrastructure [6]. In particular, the high-performance continuous-carbon-fibre composites, which are the object of this work, are mostly used in:

- aerospace;
- automotive;
- renewable energy generation.

Each of this sectors is now discussed in a dedicated subsection.

1.4.1 Aerospace

In military aircraft, low weight is the key to obtain a better performance and an higher payload. For this reason, the air force first used high-performances continuous-carbon-fibre composites and drove the development of these materials. Thanks to this, composites (on fighters) now approach 20 to 40% of the airframe weight and many technologies are available even for applications in civil aviation. Let us make some examples of both military and civil aircrafts.

1.4.1.1 Fighters. Boeing F18

Composite materials are used extensively in the Boeing F/A-18 (Figure 1.3) which is a carrier-based multirole fighter (the "F" stands for fighter and the "A" for attack aircraft). The oldest version is the McDonnell Douglas F/A-18C Hornet and took its first flight in 1978. The company that designed this aircraft merged with Boeing in 1997 so that now we can simply refer to it as Boeing F/A-18C Hornet. As we can see from Figure 1.3, carbon-epoxy composites are used both in primary structure (the vertical fin, the wings and the horizontal tail surfaces) and secondary structure but they only account for a 10% of the structural weight, which seems to be only a few. Nevertheless we have to remember what we reported in §1.3.1: the weight saving is only one among many other advantages that the application of composite materials leads to. For example, thanks to composite materials, the number of parts that the aircraft is made of can be significantly decreased (about - 30%), as well as the maintenance man-hours per flight hour (about - 50%). Both these aspects must be considered because they all combine

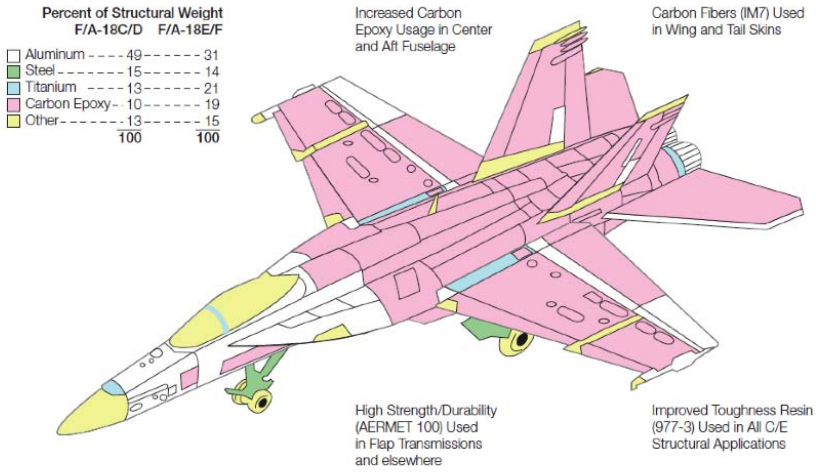

Figure 1.3: Composites application on Boeing F/A-18C/D and F/A-18E/F [7].

to define the life-cycle cost.
The next version is the Boeing F/A-18E/F Super Hornet which took its first flight in late 1995. This model use a greater percentage of carbon-epoxy composites (20%). There is also a more recent version of F/A-18 called Advanced Super Hornet that has been developed, but no data about the usage of composite materials could be found.

1.4.1.2 Civil aviation. Boeing 787 and Airbus A380

The early use of composite materials in the aircraft industry dates back to the late 1950s and started with the Boeing 707. From that moment, composite materials have been increasingly used, as the Figure 1.4[1] shows, with the two most important companies (Airbus and Boeing) each trying to surpass (or at least equalize) the other. This continuous rivalry brought recently to the development of two models which are very similar and substantially equivalent: the A350 from Airbus and the B787 from Boeing.
The Boeing 787 Dreamliner (Figure 1.5) massively uses composite materials for the primary structure. All fuselage sections and the main wing box are designed with carbon-epoxy laminates as well as the horizontals and vertical stabilizer boxes. Also wing leading edge slats and trailing edge flaps are made of carbon fibre laminate materials. Even secondary structures widely employe composite materials. For example rudder, elevators, winglets and nacelle cowlings are realized with sandwich structures while others such as the fairing on the wings, stabilizers, radome and wing-to-fuselage fairings are made of glass epoxy laminate materials or similar materials. Of course metals such as aluminium, titanium and steel are also used for example in the leading edges of nacelles and, in general,

[1]It is important to point out that in the y-axis there is the percentage by weight of composite materials which include carbon-epoxy, glass-epoxy, sandwich structures etc...

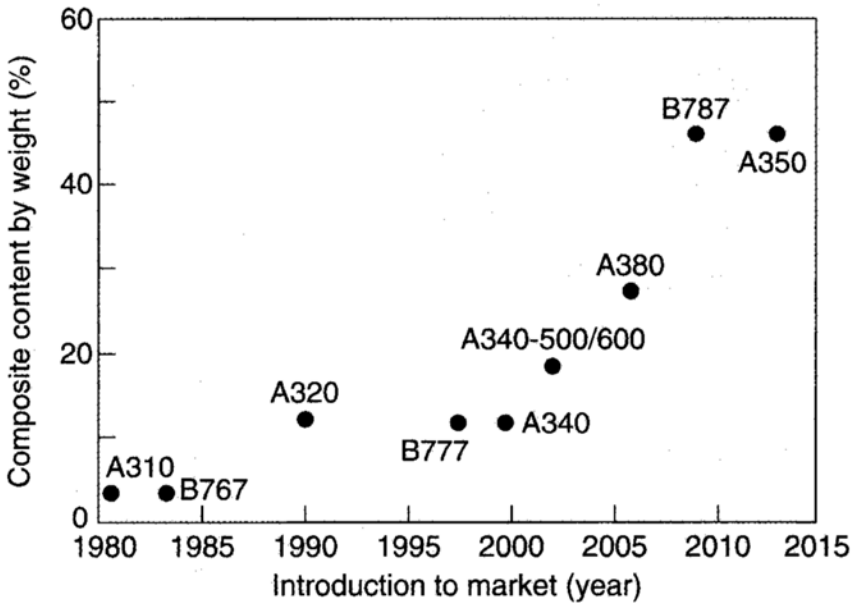

Figure 1.4: Usage of composite materials in civil aviation over years. A = Airbus, B = Boeing. The chart is taken from [8].

for those structures which have to carry heavy loads [9].

A350 is the Airbus response to the Boeing's 787 Dreamliner. Finding information about this plane is much more difficult in comparison to the Boeing's aircraft. Anyway, looking at the Figure 1.6, we can say that the parts made by composite materials are about the same. Airbus A350 uses an higher percentage of composite materials (53%) in comparison with Boeing 787 (50%). However we have to point out that the aircraft from Boeing was developed earlier than the one from Airbus.

1.4.2 Automotive and Renewable Energy Generation

It has been a very long time now that we talk about electric cars and some progress have been achieved in the last years. From the Paris conference has arisen the need to significantly reduce the emissions. To achieve this goal most of the governments decided to work simultaneously on two fields:

- reduce the energy consumption;
- increase the share of renewable energy in final energy consumption.

In the automotive sector the development of greener vehicles sees composite materials playing an important role in order to reduce the weight of the cars and thus, the emissions. In 2010 Tesla developed the Roadster, an electric vehicle which had an aluminium frame and a composite skin. This was one of the first cars to use composite materials, but it was really expansive (110k $). Then in 2013 BMW started the production of the i3 (Figure 1.7), an electric city car.

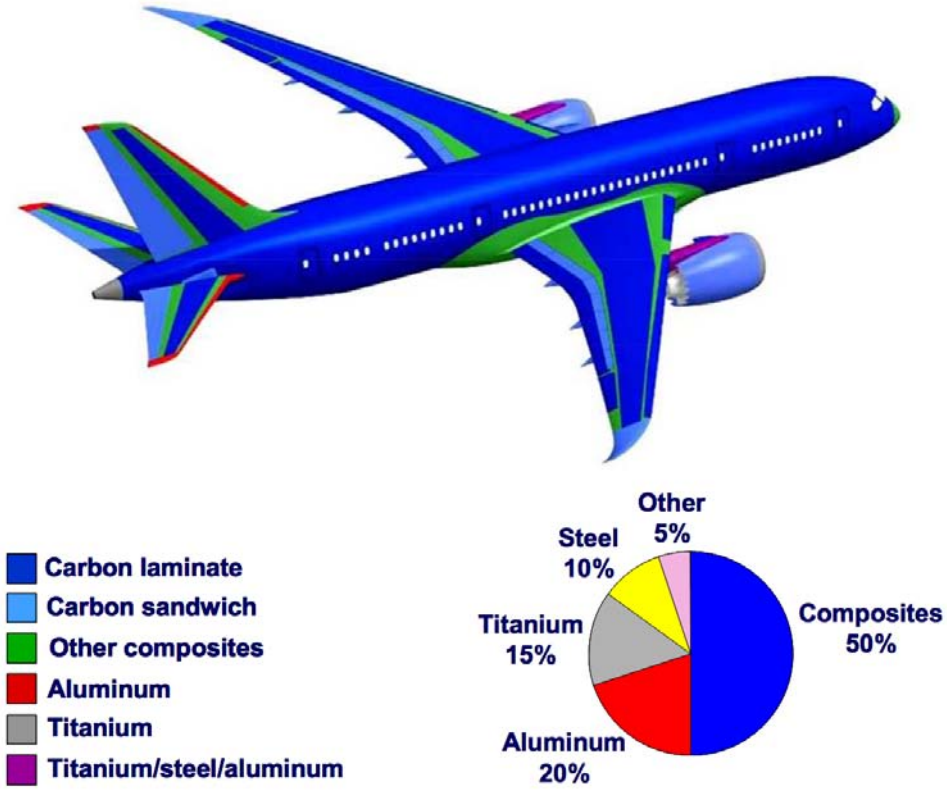

Figure 1.5: Usage of composite materials in Boeing 787 Dreamliner. Source [9].

This was the first mass-produced automobile using both a composite skin and a composite frame. Being a series-manufactured car allowed i3 to be less expensive than the Tesla Roadster, but actually not cheap (40k to 50k $).

Composite materials play a central role even in the renewable energy generation sector and in particular in the production of energy from the wind. In the last 25-30 years the use of wind turbines for electricity generation has grown from a grass-root "green" initiative to a financially sustainable primary energy resource. This is due to the fact that we passed from onshore "small" 150 kW turbines in the 1980s to "very big" 2 to 5 MW turbines which are installed both onshore and off-shore. Glass-fibre reinforced plastics were selected in the early wind turbine days because of good material availability and well-documented processing technology. However the power of the turbines increased over the years, thanks to the usage of larger, and thus heavier, blades. To lighten the structure, carbon-fiber reinforced plastic has been used since they have good stiffness, strength and fatigue and corrosion resistance. Nowadays, a hybrid CFRP-spar/GFRP-skin design is the most widely established solution since this presents the best compromise between improved performance and the higher cost of carbon fibre [10].

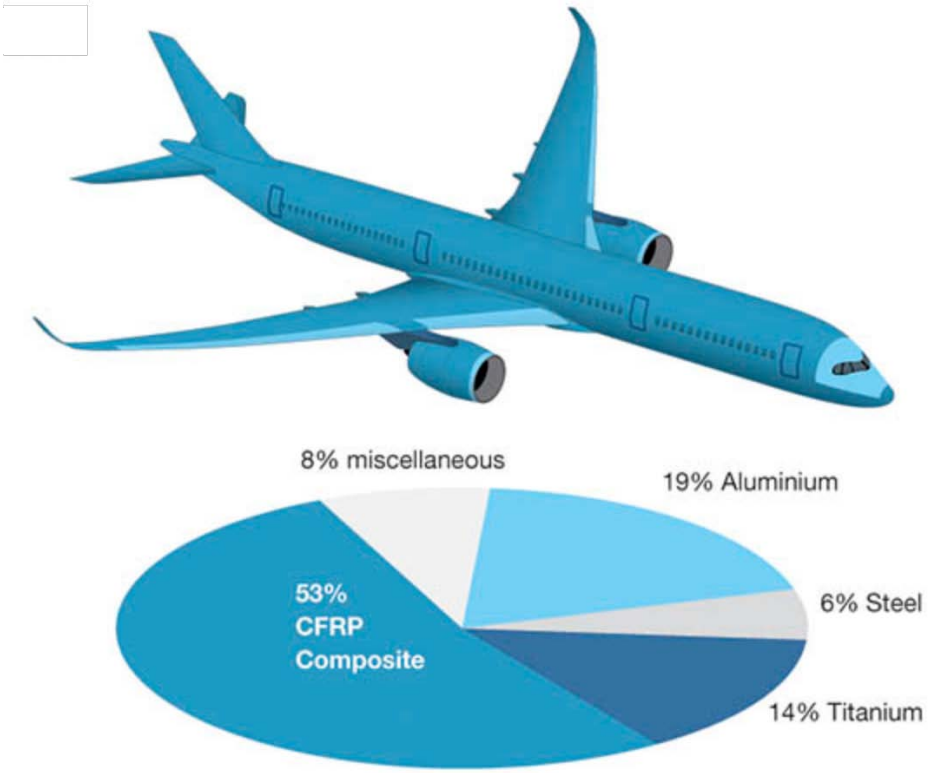

Figure 1.6: Usage of composite materials in Airbus A350-900 XWB. `http://www.hkengineer.org.hk/program/home/articlelist.php?cat=article&volid=180`

Figure 1.7: BMW i3 electric car. The frame and the skin are both made with composite materials. `http://articles.sae.org/11618/`

Chapter 2

Fracture in Composite Materials

This chapter gives a brief introduction to fracture mechanics. First the most common fracture modes are described. Then the beam theory used by Williams to calculate the total fracture toughness is outlined and the mode partitioning theories by Williams and Hutckinson & Suo are presented. Next the J-integral and the Ishikawa's decomposition are described. Subsequently the standard tests for the determination of the fracture toughness of symmetric samples are presented and the main equations are provided. Finally the idea behind this project and the main steps of the work are outlined.
Most of the information provided in this chapter are taken from [11], [12],[13] and [14].

2.1 Delamination and Fracture Modes

Fracture of a brittle material occurs when sufficient stress and work is applied at the atomic level to break the bonds that hold its atoms together. The material's theoretical strength, which can be calculated using a simple atomistic model, is in the order of $\frac{E}{10}$, with E being the Young's modulus. However, the experimentally determined strength of the same material is normally several orders of magnitude less than the theoretical one. This is due to the presence of (most of the time microscopic) defects which locally amplify the applied stress above the cohesive strength of the material. Fracture mechanics is concerned with the study of these cracks.
There are mainly three different modes in which a material can be loaded (Figure 2.1 from left to right):

- mode I;
- mode II;
- mode III.

It is also possible to load a material under any combination of these three modes. In this work, only pure mode I, pure mode II and mixed mode I/II simulations/tests will be carried out.

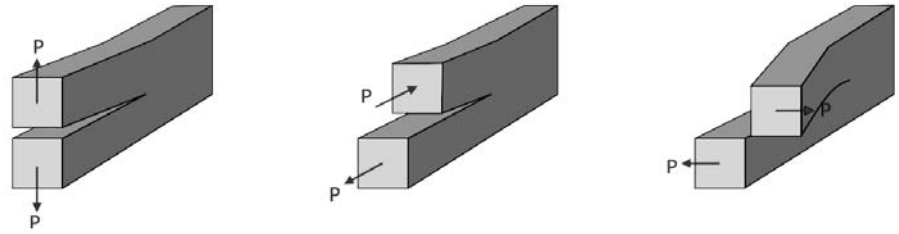

Figure 2.1: Loading (or fracture) modes. From left to right: mode I (opening), II (plane shear) and III (out of plane shear).

Composite materials are prone to delamination, this means that in the samples studied in this work, which are manufactured using pre-impregnated plies, the crack normally propagates in the resin rich region between the plies. This type of breaking of the composite is called "substrate failure".

2.2 Linear Elastic Fracture Mechanics and Delamination Calculations

Linear Elastic Fracture Mechanics (LEFM) assumes that a homogenous, isotropic, linear elastic body contains a sharp crack and then describes the energy change which occurs when such a body undergoes an increase in the crack area. Despite these assumptions, this theory can be applied also to composite materials. The presence of anisotropy simplify the analysis because the crack propagates between the plies, so in a plane that is known in advance instead to be determined. For one dimensional cases, deformations are governed by the beam theory and so the analysis is simplified further. This is often the case in composite laminates with unidirectional fibre reinforcements.
Williams [14] used the beam theory as a basis for calculating the energy release rate (ERR), G, of fibre reinforced polymers under mode I, II and mixed-mode loading conditions. The geometry that he considered is depicted in Figure 2.2. This is a thin sheet of thickness $2h$ and width B containing a delamination, or crack, at distance h_1 from the top surface and at a distance h_2 from the bottom surface. Bending moments M_1 and M_2 are applied to the upper and lower sections at the end of the delamination. If the crack grows of a quantity δa, G may be defined as

$$G = \frac{1}{B}\left(\frac{dU_e}{da} - \frac{dU_s}{da}\right) \tag{2.1}$$

where U_e is the external work performed and U_s the strain energy. After several steps Williams obtained

$$G = \frac{1}{16BEI}\left[\frac{M_1^2}{\xi^3} + \frac{M_2^2}{(1-\xi)^3} - (M_1 + M_2)^2\right] \tag{2.2}$$

where E is the beam modulus in the bending direction (for an isotropic material in plane strain condition $E = \frac{E^*}{1-\nu^2}$ with E^* being the Young's modulus and ν

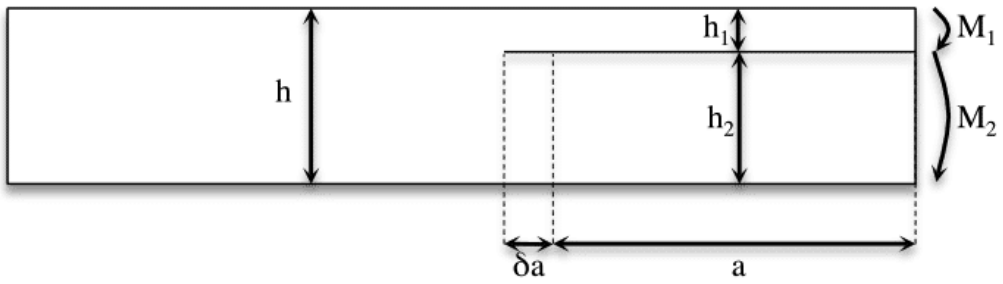

Figure 2.2: Delamination geometry used by Williams to derive the equation of the ERR.

the Poisson's ratio), I is the second moment of area of half the uncracked beam ($I = \frac{Bh^3}{12}$) and ξ is the ratio between the thickness of the top beam and the total thickness ($\xi = \frac{h_1}{2h}$).

2.3 Crack Growth and Stability

Crack growth occurs when the ERR reaches a critical value, G_c, that is sufficiently large enough to overcome the material's resistance to fracture, R. However, this crack growth may be stable or unstable depending on whether G or R vary with crack length. A plot of R versus crack length is known as a resistance curve or R-curve. A plot of G versus crack length is known as a driving force curve .
The Figure 2.3 (a) shows a flat R-curve; this is the case of a material for which the resistance is constant with the crack growth. Let's suppose that the sample contains a crack of length a_c. When the applied stress is σ_1 the crack is stable and no growth occurs. If the stress is then increased to σ_2 the crack growth becomes unstable because the driving force (G) increases with the crack growth while the material resistance (R) remains constant. The Figure 2.3 (b), instead, shows a rising R-curve. If the sample contains a crack of length a_1, the application of a load σ_1 will not cause any crack growth. If then the load is increased to σ_2 the crack will grow to a length of a_2 but no more. This is because the driving force (G) increases at a slower rate than the material resistance (R) and thus stable crack growth is achieved. If finally the stress is increased to σ_3 (or more), the rate of change of the driving force (G) is greater than the slope of the R-curve. Therefore the crack will grow in an unstable manner.
In general, the condition for stable crack growth is

$$\frac{dG}{da} \leq \frac{dR}{da} \tag{2.3}$$

and, if the material resistance is constant (which is the case of uni directional carbon fibre reinforced plastics used in this work),

$$\frac{dG}{da} \leq 0. \tag{2.4}$$

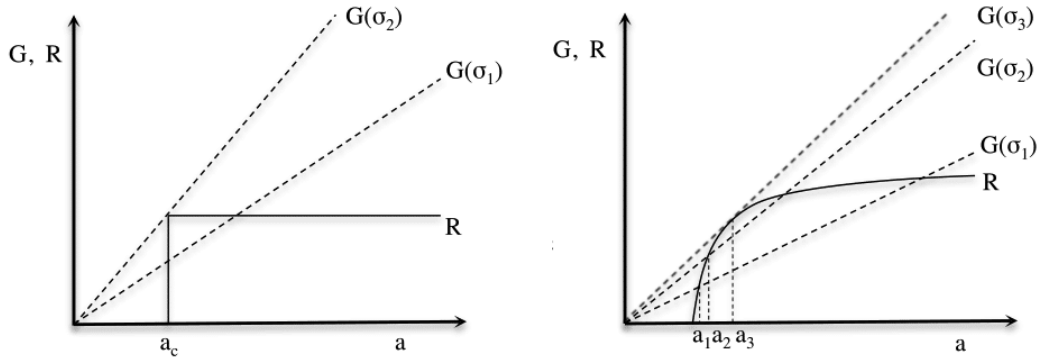

(a)(b)

Figure 2.3: Constant (a) and rising (b) R-curve.

2.4 Mix Mode Partitioning Theories

As it was reported in §2.1, a sample can be loaded in three different modes plus any combination of them (mixed mode). In §2.2 and 2.3 we talked in general about the concepts of ERR and material's resistance (or toughness). However, both the total ERR and the material's resistance depend on the loading conditions. For the vast majority of the materials the mode I loading condition is the most critical and the correspondent fracture toughness is taken as reference when designing structures. Unluckily, laminates may constitute an exception. Dillard [15], in fact, discovered that for some adhesively bonded joints, the toughness under a mixed mode loading condition can be much lower than under a pure mode I. It is therefore of primary importance to determine the toughness of a composite as a function of mode mixity, which is defined as the ratio between the mode II ERR and the total ERR ($\frac{G_{II}}{G}$, with $G = G_I + G_{II}$). In this way one can generate what is known as a mixed mode failure criterion, or failure locus, which can help to avoid the risk non-conservative design.
However, the measurement of the mixed mode failure locus is not straightforward because the mode mixity depend on both the geometry and the moments applied. Therefore, one must currently rely on the accuracy of analytical partitioning theories in order to determine the correct mode of loading (i.e. M_1 and M_2) for a given test configuration (i.e. the delamination geometry, in particular h_1 and h_2). In the following sections the partitioning theories from Williams [14] and from Hutckinson and Suo [16] will be outlined. Many other partitioning theories have been developed but the previous two are the only ones that will be used in this work. The reason is that each theory works well for one specific case but none of them succeed in predicting the mode mixity for all composite materials. In fact the damage at the crack tip plays an important role [12], and the real partitioning lies between the prediction from Hutckinson and Suo and that of Williams.

2.4.1 Williams: Global Solution

As it was reported in §2.2, Williams used the beam theory for both obtaining the total ERR (Equation 2.2) and the mode partition. While doing this he looked at the whole beam and he didn't consider any local stress or strain distribution. For this reason, this way of approaching the problem is known as the global approach and the mixed mode partition that derives is referred as the global solution. In the next part of this section only the main points of this theories will be outlined. For a more detailed (step by step) derivation of all the equations please refer to [14] or, better, to [11].
Considering the delamination geometry of Figure 2.2 Williams made two observations:

- in pure mode II loading the curvature of the two beams is the same;
- the opening mode (I) requires moments in opposite sense.

Thanks to this he was able to express the moments applied to the top and bottom beam (M_1 and M_2) as a combination of three terms:

- M_I, moment causing opening (or mode I);
- M_{II}, moment causing shearing (or mode II);
- $M_I M_{II}$, cross product between M_I and M_{II};

$$M_1^2 = M_{II}^2 - 2M_I M_{II} + M_I^2 \tag{2.5a}$$
$$M_2^2 = \psi^2 M_{II}^2 + 2\psi M_I M_{II} + M_I^2 \tag{2.5b}$$
$$M_1 M_2 = \psi M_{II}^2 + M_I M_{II}(1-\psi) - M_I^2 \tag{2.5c}$$

where $\psi = \left(\frac{1-\xi}{\xi}\right)^3$. By substituting these newly obtained relations into Equation 2.2 Williams obtained

$$G = \frac{1}{16BEI}\left[M_I^2 C_1 + M_{II}^2 + M_I M_{II} C_{12}\right] \tag{2.6}$$

where C_1, C_2 and C_{12} are functions of ξ, and so of the geometry only. Williams found out that, whatever the geometry is, C_{12} is always equal to zero. This is of much great importance because it implies that the ERR doesn't depend on the cross product $M_I M_{II}$ and can thus be partitioned into mode I and mode II

$$G_I = \frac{M_I^2(1+\psi)}{16BEI(1-\xi)^3} \tag{2.7a}$$
$$G_{II} = \frac{3M_{II}^2(1-\xi)(1+\psi)}{16BEI\xi^2}. \tag{2.7b}$$

When applying Equations 2.7 (a) and (b) also the following relations might be useful

$$M_I = \frac{M_2 - \psi M_1}{1+\psi} \tag{2.8a}$$

$$M_{II} = \frac{M_2 + M_1}{1+\psi}. \tag{2.8b}$$

2.4.2 Hutckinson and Suo: Local Solution

Differently from Williams, Hutckinson and Suo performed the partition of the ERR by considering the presence of singular stress distribution at the crack tip (K dominant region). Since they considered local conditions at the crack tip the mixed mode partition that they proposed is referred as the local solution.
Starting from the decomposed intensity factors K_I and K_{II} and using the relation that links them to the ERR

$$G = \frac{K_I^2 + K_{II}^2}{E} \tag{2.9}$$

they obtained the partitioned ERR

$$G_I = \frac{1}{E}\left(\frac{Pcos(\omega)}{\sqrt{2h_1U}} + \frac{Msin(\omega+\phi)}{\sqrt{2h_1^3V}}\right)^2 \tag{2.10a}$$

$$G_{II} = \frac{1}{E}\left(\frac{Psin(\omega)}{\sqrt{2h_1U}} - \frac{Mcos(\omega+\phi)}{\sqrt{2h_1^3V}}\right)^2 \tag{2.10b}$$

where

- the delamination geometry is the same as for Williams (Figure 2.2);
- P and M are linear combinations of the load applied

$$P = \frac{-D_2(M_1+M_2)}{h_1} \tag{2.11a}$$

$$M = M_1 - D_3(M_1+M_2) \tag{2.11b}$$

$$D_2 = \frac{\frac{6}{\gamma}}{(\frac{1}{\gamma}+1)^3} \tag{2.11c}$$

$$D_3 = \frac{1}{(\frac{1}{\gamma}+1)^3}; \tag{2.11d}$$

- γ is the beams ratio ($\gamma = \frac{h_1}{h_2}$);
- U, V and ϕ are geometric factors

$$U = \frac{1}{1+4\gamma+6\gamma^2+3\gamma^3} \tag{2.12a}$$

$$V = \frac{1}{12(1+\gamma^3)} \tag{2.12b}$$

$$\phi = arcsin\big(6\gamma^2(1+\gamma)\sqrt{UV}\big); \tag{2.12c}$$

- ω is given by the (approximate) relation

$$\omega = 52.1 - 3\gamma \tag{2.13}$$

which is valid for $0 \leq \gamma \leq 1$. If $\gamma \geq 1$, it is necessary to use $\frac{1}{\gamma}$ instead of γ in Equations 2.11 (c) and (d), 2.12 (a), (b) and (c) and 2.13. The moments M_1 and M_2 in Equations 2.11 (a) and (b) must also be swapped.

Finally it is important to point out that the Equation 2.13 gives a result which is in degrees and not in radians.

2.5 J-Integral

In all the previous sections the LEFM theory has been used to obtain both the total and the mode partitioned ERR. As it was specified in §2.2, this theory can be applied only to homogenous, isotropic, linear elastic bodies. This is of course a major limitation. However, it is possible to overcome this problem thanks to the so called J-Integral, method that was proposed, for bodies containing a crack, by Rice [17] in 1968. Because the J-integral is applicable for infinite as well as finite, homogeneous as well as inhomogeneous, linear as well as non-linear materials, it is a very powerful method for determining the crack extension force.
The J-Integral, in its most general form (3D), states that the force on an elastic singularity in the x_i direction is [18]

$$J_i = \int_S (w n_i - T_j u_{j,i}) dS \tag{2.14}$$

where S is a surface containing the crack tip and the significance of the others terms will be explained in the remainder of this paragraph.
In this work only 2D geometries (and loadings) are considered and thus a simpler 2D expression of the J-Integral can be used [19]. With reference to the Figure 2.4, the J-Integral is usually written for the x direction (J_x) for a crack along the x direction as

$$J_i = \int_\Gamma w dy - T_i \frac{\partial u_i}{\partial x} ds \tag{2.15}$$

where $i = x$, $j = y$, Γ is a contour line going from the bottom surface to the top surface of the crack (or vice versa), $w = \int_0^{\epsilon_{ij}} \sigma_{ij} d\epsilon_{ij}$ is the strain energy density (with σ_{ij} and ϵ_{ij} being the the stress and strain tensors respectively), $T_i = \sigma_{ij} n_j$ is the the traction vector (with n_j being the outward unit vector normal to Γ), u_i the displacement vector and ds a length increment along the contour Γ.
The J-Integral has the following properties:

1. $J = G$: J_i is the driving force for the singularity along x_i direction (i.e. J (J_x) is the driving force for the crack to grow in the x direction). This means that the evaluation of Equation 2.15 gives the total ERR G.

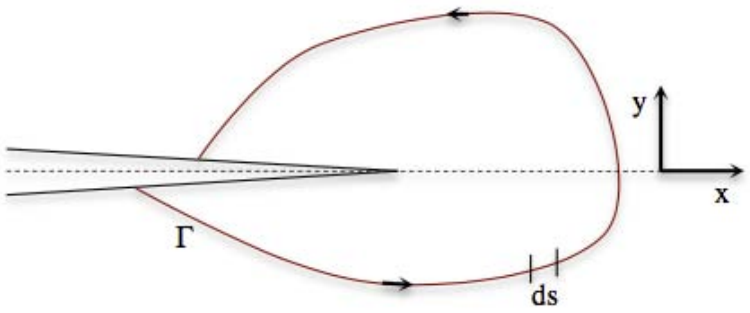

Figure 2.4: Arbitrary contour around the tip of a crack.

2. Path Independence: J_i is invariant with respect to the shape of surface S (or contour Γ for the 2D case) as long as it contains the same singularity[1].

2.6 Mode Decomposed J-Integral

The J-Integral, as it is written in Equation 2.15 allows the calculation of the total ERR but it doesn't provide enough information to decompose it into mode I and mode II. Ishikawa [20] in 1979 proposed a decomposition of the J-Integral that was based on the decomposition of the displacement, strain and stress fields into symmetric (causing mode I) and asymmetric (causing mode II) components. Let's consider first the displacement field. For the point P in Figure 2.5, the displacement vectors causing mode I (u_i^I) and mode II (u_i^{II}) are given by

$$u_i^I = \begin{bmatrix} u_1^I \\ u_2^I \end{bmatrix} = \frac{1}{2} \begin{bmatrix} u_1 + u_1^{'} \\ u_2 - u_2^{'} \end{bmatrix} \tag{2.16a}$$

$$u_i^{II} = \begin{bmatrix} u_1^{II} \\ u_2^{II} \end{bmatrix} = \frac{1}{2} \begin{bmatrix} u_1 - u_1^{'} \\ u_2 + u_2^{'} \end{bmatrix} \tag{2.16b}$$

$$u_i = u_i^I + u_i^{II} \tag{2.16c}$$

where u_i and $u_i^{'}$ are respectively the displacement vectors of point P and P', which is symmetrical to P about the crack plane (i.e. x axis). For this reason the contour Γ must be symmetric about the crack plane. With similar meaning symbology the mode decomposed strain and stress fields are

$$\epsilon_{ij}^I = \begin{bmatrix} \epsilon_{11}^I & \epsilon_{12}^I \\ \epsilon_{21}^I & \epsilon_{22}^I \end{bmatrix} = \frac{1}{2} \begin{bmatrix} \epsilon_{11} + \epsilon_{11}^{'} & \epsilon_{12} - \epsilon_{12}^{'} \\ \epsilon_{21} - \epsilon_{21}^{'} & \epsilon_{22} + \epsilon_{22}^{'} \end{bmatrix} \tag{2.17a}$$

$$\epsilon_{ij}^{II} = \begin{bmatrix} \epsilon_{11}^{II} & \epsilon_{12}^{II} \\ \epsilon_{21}^{II} & \epsilon_{22}^{II} \end{bmatrix} = \frac{1}{2} \begin{bmatrix} \epsilon_{11} - \epsilon_{11}^{'} & \epsilon_{12} + \epsilon_{12}^{'} \\ \epsilon_{21} + \epsilon_{21}^{'} & \epsilon_{22} - \epsilon_{22}^{'} \end{bmatrix} \tag{2.17b}$$

$$\epsilon_{ij} = \epsilon_{ij}^I + \epsilon_{ij}^{II} \tag{2.17c}$$

[1]The assumptions for having path independency are actually four: partial differentiability of the strain energy density with respect to the strain, equilibrium of the stress field, compatibility of the strain field (which means that it can be derived from the displacement field) and no traction on the surface of the crack. Further details can be found in [17] or in [20].

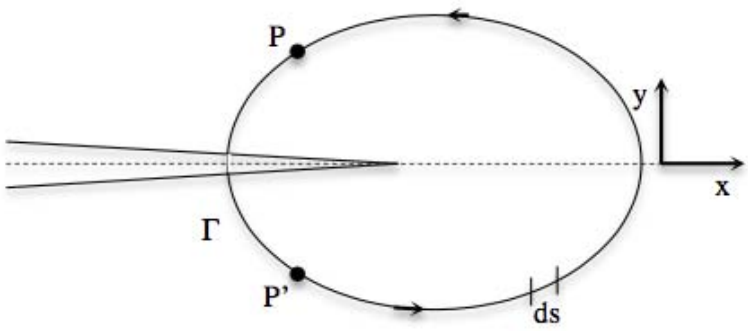

Figure 2.5: Contour symmetrical about the crack plane (2D case, the symmetry is about the x axis).

$$\sigma_{ij}^{I} = \begin{bmatrix} \sigma_{11}^{I} & \sigma_{12}^{I} \\ \sigma_{21}^{I} & \sigma_{22}^{I} \end{bmatrix} = \frac{1}{2} \begin{bmatrix} \sigma_{11} + \sigma_{11}^{'} & \sigma_{12} - \sigma_{12}^{'} \\ \sigma_{21} - \sigma_{21}^{'} & \sigma_{22} + \sigma_{22}^{'} \end{bmatrix} \tag{2.18a}$$

$$\sigma_{ij}^{II} = \begin{bmatrix} \sigma_{11}^{II} & \sigma_{12}^{II} \\ \sigma_{21}^{II} & \sigma_{22}^{II} \end{bmatrix} = \frac{1}{2} \begin{bmatrix} \sigma_{11} - \sigma_{11}^{'} & \sigma_{12} + \sigma_{12}^{'} \\ \sigma_{21} + \sigma_{21}^{'} & \sigma_{22} - \sigma_{22}^{'} \end{bmatrix} \tag{2.18b}$$

$$\sigma_{ij} = \sigma_{ij}^{I} + \sigma_{ij}^{II} \tag{2.18c}$$

where, of course, $\epsilon_{12}^{I} = \epsilon_{21}^{I}$, $\epsilon_{12}^{II} = \epsilon_{21}^{II}$, $\sigma_{12}^{I} = \sigma_{21}^{I}$ and $\sigma_{12}^{II} = \sigma_{21}^{II}$. Substituting all these relations in Equations 2.15 the J-Integral becomes

$$J = \int_{\Gamma} \left[\int_{0}^{\epsilon_{ij}} (\sigma_{ij}^{I} + \sigma_{ij}^{II}) d(\epsilon_{ij}^{I} + \epsilon_{ij}^{II}) dy - (\sigma_{ij}^{I} + \sigma_{ij}^{II}) n_j \frac{\partial u_i^{I} + u_i^{II}}{\partial x} ds \right]. \tag{2.19}$$

The expansion of Equation 2.19 gives

$$J = J_I + J_{I/II} + J_{II/I} + J_{II} \tag{2.20}$$

in which are present also terms involving the product between J_I and J_{II}. However Ishikawa showed that these "mixed" terms reduce to zero and therefore J_I and J_{II} are equal to the mode I and mode II ERR G_I and G_{II} according to the equations

$$J_I = \int_{\Gamma} \left[\int_{0}^{\epsilon_{ij}} \sigma_{ij}^{I} d\epsilon_{ij}^{I} dy - \sigma_{ij}^{I} n_j \frac{\partial u_i^{I}}{\partial x} ds \right] \tag{2.21a}$$

$$J_{II} = \int_{\Gamma} \left[\int_{0}^{\epsilon_{ij}} \sigma_{ij}^{II} d\epsilon_{ij}^{II} dy - \sigma_{ij}^{II} n_j \frac{\partial u_i^{II}}{\partial x} ds \right]. \tag{2.21b}$$

2.7 Standard Tests

The standard tests are performed on symmetric samples. This means that the specimens are centrally cracked (i.e. $h_1 = h_2$) so that $\xi = \frac{1}{2}$ and $\phi = 1$.

More, these standard tests are normally carried out by applying loads (P) or displacements (δ) instead of moments since the machines for the application of loads/displacements are less sophisticated than those for the moments. The equations provided in this section are taken from [11] and from the standard test procedures which are different for each test.

2.7.1 Double Cantilever Beam (DCB) Test

The double cantilever beam (DCB) test is depicted in Figure 2.6 and it is used to determine the pure mode I fracture toughness G_{IC} according to equation

$$G_{IC} = \frac{P^2 a^2}{BEI} \tag{2.22}$$

where a is the total crack length. The moment applied to each beam is $M = Pa$. The Equation 2.22 derives from the so called Simple Beam Theory (SBT) which:

1. underestimates the compliance (i.e. displacement divided by load) since the beam is not perfectly built in;
2. overestimates the applied moments which are lower than Pa;
3. doesn't take into account that the loads/displacements are applied via blocks which locally stiffen the beams where they are glued.

The corrected beam theory (CBT) overcomes all these problems:

$$G_{IC} = \frac{3P\delta F}{2B(a + |\Delta_I|)N} \tag{2.23}$$

where Δ_I, F and N are the correction factors respectively for 1, 2 and 3 (Figure 2.7). The expression for estimating them can be found in the standard [21] together with the specimen's dimensions and further details on test procedure which will be also described later in this work.

2.7.2 End Loaded Split (ELS) Test

The end loaded split (ELS) test is used to determine the pure mode II fracture toughness. The specimen is clamped at one end so that it can move horizontally but not vertically (Figure 2.8). According to the SBT, the fracture toughness under pure mode II loading, G_{IIC}, is given by equation

$$G_{IIC} = \frac{3P^2 a^2}{16BEI}. \tag{2.24}$$

Of course Equation 2.24 has the same problems as 2.22, problems that are overcome by applying the CBT

$$G_{IIC} = \frac{9P^2 (a_e)^2 F}{4B^2 h^3 EN} \tag{2.25}$$

where a_e, F and N are the correction factors and the expression for estimating them can be found in the standard [22].

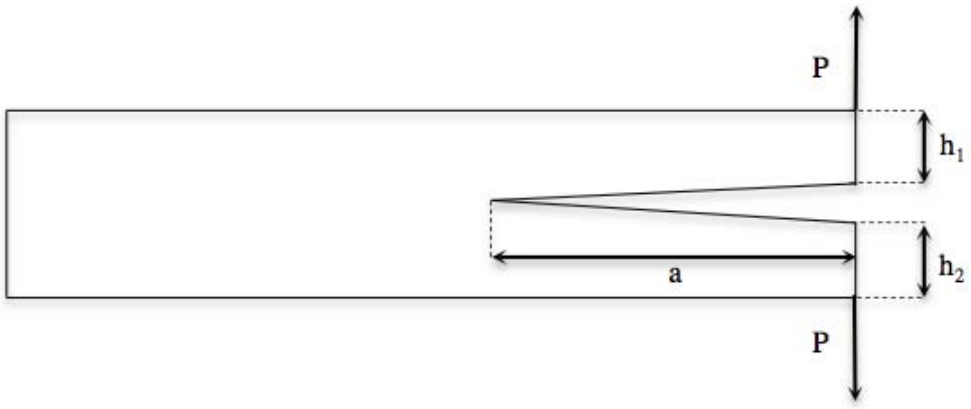

Figure 2.6: Double cantilever beam (DCB) test.

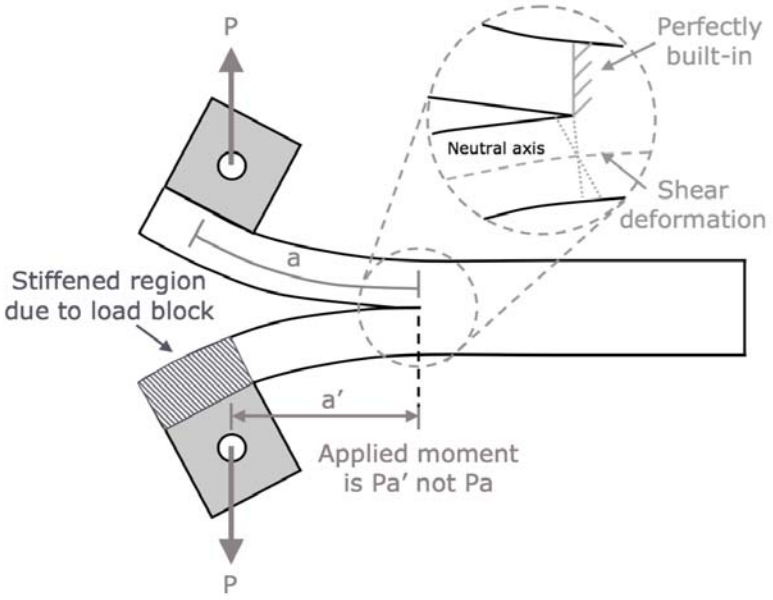

Figure 2.7: Double cantilever beam (DCB), illustration of the correction factors (from [11])

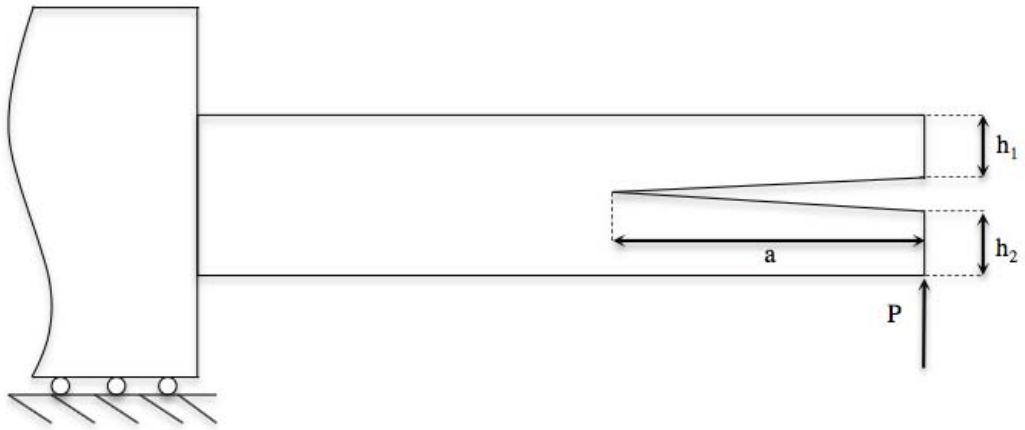

Figure 2.8: End Loaded Split (ELS) test.

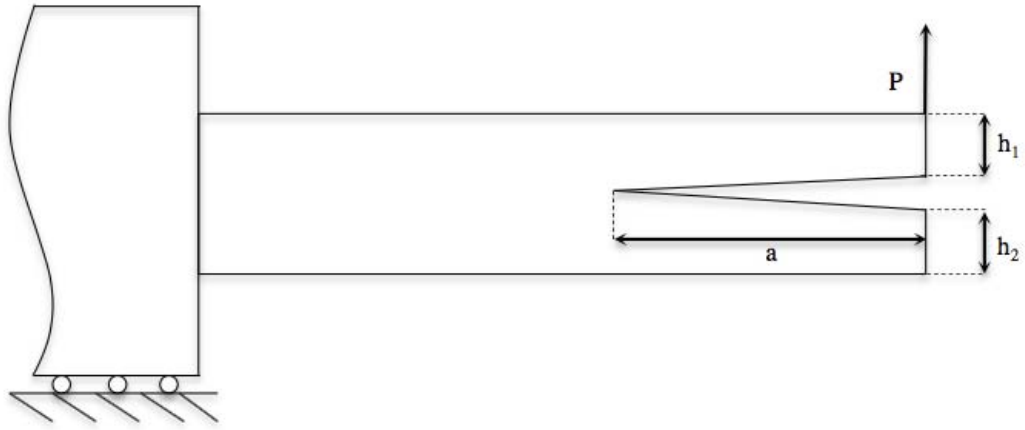

Figure 2.9: Fixed Ratio Mixed Mode (FRMM) test.

2.7.3 Fixed Ratio Mixed Mode (FRMM) Test

The Fixed Ratio Mixed Mode (FRMM) test (Figure 2.9) is used to determine the mixed mode fracture toughness $G_{I/IIC}$ ($G_{I/II} = G_I + G_{II}$). For this test (which is symmetric) the mode mixity $\frac{G_{II}}{G}$ is known and is $\frac{3}{7}$ (0.4287). The equations provided by the CBT are

$$G_I = \frac{3P^2(a+\Delta_I)^2F}{B^2Eh^3N} \tag{2.26a}$$

$$G_{II} = \frac{9P^2(a+\Delta_{II})^2F}{4B^2Eh^3} \tag{2.26b}$$

where Δ_I, Δ_{II} ($\Delta_{II} = 0.42\Delta_I$, F and N are the correction factors and the expression for estimating them can be found in [23].

2.8 Project Overview

§2.7 shows that reliable tests are available for the determination of mode I, mode II and mixed mode fracture toughness on symmetric specimens. In general a mixed mode test can be performed on a sample in three ways:

1. by applying different moments ratios $\frac{M_1}{M_2}$ to symmetric specimens;
2. by applying only a moment M_1 to the top (or bottom) beam of a asymmetric specimen;
3. by combining 1 and 2.

1 and 3 are not considered in this work. 2, instead, is basically a variant of the previously described FRMM test performed on asymmetric specimens. For this reason this test is called Asymmetric Fixed Ratio Mixed Mode (AFRMM). This kind of test is of interest to this work since a reliable analytical partition of the energy is not available. In fact all the theories (Williams, Hutckinson and Suo and many others) are in agreement for the partition on symmetric samples ($\frac{G_{II}}{G} = \frac{3}{7}$) but they give considerably different results in the asymmetric cases. Up to now the Semi Analytical Cohesive Analysis (SACA) [12] developed by Mark Conroy is the only procedure that is available to accurately estimate the mode partition in asymmetric samples.
The aim of this project is to try to obtain experimentally the mode partition using a Digital Image Correlation (DIC) approach. The DIC gives as output the displacement and strain fields. Knowing the material's properties and assuming an elastic behaviour, one can easily get the stress field. Feeding all these informations into the expressions of the mode decomposed J-Integral it is possible to obtain J_I and J_{II} and, therefore the mode partition $\frac{J_{II}}{J}$, which is equal to $\frac{G_{II}}{G}$ in the elastic case (§2.6).
At least in its initial idea the project was articulated in several steps:

1. develop a MATLAB script for the calculation of the total ERR (J-Integral) and another for the partitioned ERR (mode decomposed J-Integral);
2. develop ABAQUS models for DCB, ELS, FRMM and AFRMM geoemetries;
3. test the scripts using the fields data from ABAQUS;
4. manufacture DCB, ELS and FRMM samples;
5. test the samples above using the DIC in order to check if there is agreement between the ERRs obtained from the DIC and thos calculated using the equations in §2.7;
6. manufacture AFRMM samples with different beams ratios;
7. test them with the DIC and check if the mode partition in agreement with what is predicted by SACA procedure.

All this seems very easy to do but many have been the difficulties found along the way especially in the experimental part because the DIC equipment was relatively new (mid 2016) and at University College Dublin (UCD) there was no one able to use it properly. For this reason only part of the planned work has been done and the task to go on with it is left to the one who (probably) is reading this report.

Chapter 3

Modelling and Numerical Partitioning

In this chapter all the computational part of this work is presented. First, all the equations used in both the MATLAB scripts for the total and for the mode decomposed ERR are derived. Then the most important features of the ABAQUS models that have been developed are outlined and the results for the DCB, ELS, FRMM and AFRMM cases are presented. All these first models are simple loadings of the previously mentioned geometries, therefore no crack growth is observed and a K-dominant region exist at the crack tip. Finally, in the last part of this chapter, the MATLAB scripts are tested in the most general (real) case by introducing damage at the crack front. This is achieved by modelling cohesive elements in ABAQUS.

3.1 Equations Derivation for the MATLAB Scripts

The MATLAB scripts that have been developed implement the Equations 2.15 and 2.21 (a) and (b) using as input the fields' data from the ABAQUS models which will be described in the next sections. The integration contour Γ is chosen to be rectangular and, in any case (i.e. for both the calculation of the total and the mode partitioned G), symmetric about the crack plane. The integration direction is counterclockwise (Figure 3.1).
The Equation 2.15 is expressed using a tensorial notation[1]; therefore, for the implementation in the MATLAB script, is necessary to expand it. Let's start from the first term, the strain energy density. This terms accounts for the energy which is stored in each point of the integration path. Upon expansion it becomes

$$\begin{aligned} w = \int_0^{\epsilon_{ij}} \sigma_{ij} d\epsilon_{ij} = \frac{1}{2}\big(&\sigma_{11}\epsilon_{11} + \sigma_{12}\epsilon_{12} + \sigma_{13}\epsilon_{13} + \\ &\sigma_{21}\epsilon_{21} + \sigma_{22}\epsilon_{22} + \sigma_{23}\epsilon_{23} + \\ &\sigma_{31}\epsilon_{31} + \sigma_{32}\epsilon_{32} + \sigma_{33}\epsilon_{33}\big) \end{aligned} \tag{3.1}$$

[1]For the tensorial notation I referred to [24], in particular section 2.4.

which reduces to

$$w = \int_0^{\epsilon_{ij}} \sigma_{ij} d\epsilon_{ij} = \frac{1}{2}\big(\sigma_{11}\epsilon_{11} + 2\sigma_{12}\epsilon_{12} + \sigma_{22}\epsilon_{22}\big) \tag{3.2}$$

since $\sigma_{ij} = \sigma_{ji}$ and $\epsilon_{ij} = \epsilon_{ji}$. Moreover, this is a 2D case and we assume plain strain conditions in the plane 1, 2 (x, y) so all the strain components containing a 3 as subscript reduce to zero.
Let's consider now the second term, which accounts for the work done by the external forces. The first part of this term is the traction vector $T_i = \sigma_{ij} n_j$, which, upon expansion becomes

$$T_i = \begin{bmatrix} t_1 \\ t_2 \\ t_3 \end{bmatrix} = \begin{bmatrix} \sigma_{11}n_1 + \sigma_{12}n_2 + \sigma_{13}n_3 \\ \sigma_{21}n_1 + \sigma_{22}n_2 + \sigma_{23}n_3 \\ \sigma_{31}n_1 + \sigma_{32}n_2 + \sigma_{33}n_3 \end{bmatrix}. \tag{3.3}$$

Since we are considering a 2D geometry, all the terms multiplied by n_3 reduce to zero. This is because n, which is the outward unit vector normal to the path Γ, lays on the 12 plane and therefore $n_3 = 0$. Consequently

$$T_i = \begin{bmatrix} t_1 \\ t_2 \\ t_3 \end{bmatrix} = \begin{bmatrix} \sigma_{11}n_1 + \sigma_{12}n_2 \\ \sigma_{21}n_1 + \sigma_{22}n_2 \\ \sigma_{31}n_1 + \sigma_{32}n_2 \end{bmatrix}. \tag{3.4}$$

The product between the traction vector ad the derivative of the displacement gives

$$\begin{aligned} t_i &= t_1 \frac{\partial u_1}{\partial x} + t_2 \frac{\partial u_2}{\partial x} + t_3 \frac{\partial u_3}{\partial x} \\ &= (\sigma_{11}n_1 + \sigma_{12}n_2)\frac{\partial u_1}{\partial x} + (\sigma_{21}n_1 + \sigma_{22}n_2)\frac{\partial u_2}{\partial x} \end{aligned} \tag{3.5}$$

because the displacement in the direction 3 equals to zero ($u_3 = 0$), and thus also its derivative with respect to the x (i.e. 1) coordinate is zero ($\frac{\partial u_3}{\partial x} = 0$). By substituting Equations 3.2 and into the expression of the J-Integral (Equation 2.15) we obtain

$$\begin{aligned} J = \int_\Gamma \Bigg\{ &\frac{1}{2}\big(\sigma_{11}\epsilon_{11} + 2\sigma_{12}\epsilon_{12} + \sigma_{22}\epsilon_{22}\big) dy \\ &- \left[(\sigma_{11}n_1 + \sigma_{12}n_2)\frac{\partial u_1}{\partial x} + (\sigma_{21}n_1 + \sigma_{22}n_2)\frac{\partial u_2}{\partial x} \right] ds \Bigg\}. \end{aligned} \tag{3.6}$$

Now, for carrying out the integration, it is useful to divide the rectangular contour Γ in five parts Γ_1, Γ_2, Γ_3, Γ_4 and Γ_5. The "total" J-Integral will then be the sum of the J-Integrals calculated along each of those partial paths

$$J = J_{\Gamma 1} + J_{\Gamma 2} + J_{\Gamma 3} + J_{\Gamma 4} + J_{\Gamma 5}. \tag{3.7}$$

Now, referring to Figure 3.1, we have:

1. for Γ_1 and Γ_5 $ds = -dy$ and $n = (-1, 0)$;
2. for Γ_2 $ds = dx$, $dy = 0$ and $n = (0, -1)$;
3. for Γ_3 $ds = dy$ and $n = (1, 0)$;
4. for Γ_4 $ds = -dx$, $dy = 0$ and $n = (0, 1)$.

We use now this information to obtain the expressions for $J_{\Gamma 1}$, $J_{\Gamma 2}$, $J_{\Gamma 3}$, $J_{\Gamma 4}$ and $J_{\Gamma 5}$

$$J_{\Gamma 1} = \int_{\Gamma 1} \left\{ \frac{1}{2}\big(\sigma_{11}\epsilon_{11} + 2\sigma_{12}\epsilon_{12} + \sigma_{22}\epsilon_{22}\big)dy + \left[-\sigma_{11}\frac{\partial u_1}{\partial x} - \sigma_{21}\frac{\partial u_2}{\partial x}\right]dy \right\} \tag{3.8a}$$

$$J_{\Gamma 2} = \int_{\Gamma 2} \left\{ 0 - \left[-\sigma_{12}\frac{\partial u_1}{\partial x} - \sigma_{22}\frac{\partial u_2}{\partial x}\right]dx \right\} \tag{3.8b}$$

$$J_{\Gamma 3} = \int_{\Gamma 3} \left\{ \frac{1}{2}\big(\sigma_{11}\epsilon_{11} + 2\sigma_{12}\epsilon_{12} + \sigma_{22}\epsilon_{22}\big)dy - \left[\sigma_{11}\frac{\partial u_1}{\partial x} + \sigma_{21}\frac{\partial u_2}{\partial x}\right]dy \right\} \tag{3.8c}$$

$$J_{\Gamma 4} = \int_{\Gamma 4} \left\{ 0 + \left[\sigma_{12}\frac{\partial u_1}{\partial x} + \sigma_{22}\frac{\partial u_2}{\partial x}\right]dx \right\} \tag{3.8d}$$

$$J_{\Gamma 5} = \int_{\Gamma 5} \left\{ \frac{1}{2}\big(\sigma_{11}\epsilon_{11} + 2\sigma_{12}\epsilon_{12} + \sigma_{22}\epsilon_{22}\big)dy + \left[-\sigma_{11}\frac{\partial u_1}{\partial x} - \sigma_{21}\frac{\partial u_2}{\partial x}\right]dy \right\}. \tag{3.8e}$$

These equations, together with Equation 3.7, are implemented in the MATLAB script for the total G.
If we replace the various σ_{ij}, ϵ_{ij} and u_i in Equations 3.8 (a), (b), (c), (d) and (e) with σ^I_{ij}, ϵ^I_{ij} and u^I_i, respectively from Equations 2.16 (a), 2.17 (a) and 2.19 (a), we find the value of the mode decomposed J-Integral (mode I) for each part of the path (i.e. $J_{I,\Gamma 1}$, $J_{I,\Gamma 2}$, $J_{I,\Gamma 3}$, $J_{I,\Gamma 4}$ and $J_{I,\Gamma 5}$) and, therefore, of the J_I along the whole path since $J_I = J_{I,\Gamma 1} + J_{I,\Gamma 2} + J_{I,\Gamma 3} + J_{I,\Gamma 4} + J_{I,\Gamma 5}$.

$$J_{I,\Gamma 1} = \int_{\Gamma 1} \left\{ \frac{1}{2}\big(\sigma^I_{11}\epsilon^I_{11} + 2\sigma^I_{12}\epsilon^I_{12} + \sigma^I_{22}\epsilon^I_{22}\big)dy + \left[-\sigma^I_{11}\frac{\partial u^I_1}{\partial x} - \sigma^I_{21}\frac{\partial u^I_2}{\partial x}\right]dy \right\} \tag{3.9a}$$

$$J_I = J_{I,\Gamma 1} + J_{I,\Gamma 2} + J_{I,\Gamma 3} + J_{I,\Gamma 4} + J_{I,\Gamma 5} \tag{3.9b}$$

The same of course is for J_{II}. It is sufficient in this case to replace σ_{ij}, ϵ_{ij} and u_i in Equations 3.8 (a), (b), (c), (d) and (e) with σ^{II}_{ij}, ϵ^{II}_{ij} and u^{II}_i, respectively from Equations 2.16 (b), 2.17 (b) and 2.19 (b).

$$J_{II,\Gamma 1} = \int_{\Gamma 1} \left\{ \frac{1}{2}\big(\sigma^{II}_{11}\epsilon^{II}_{11} + 2\sigma^{II}_{12}\epsilon^{II}_{12} + \sigma^{II}_{22}\epsilon^{II}_{22}\big)dy + \left[-\sigma^{II}_{11}\frac{\partial u^{II}_1}{\partial x} - \sigma^{II}_{21}\frac{\partial u^{II}_2}{\partial x}\right]dy \right\} \tag{3.10a}$$

$$J_{II} = J_{II,\Gamma 1} + J_{II,\Gamma 2} + J_{II,\Gamma 3} + J_{II,\Gamma 4} + J_{II,\Gamma 5} \tag{3.10b}$$

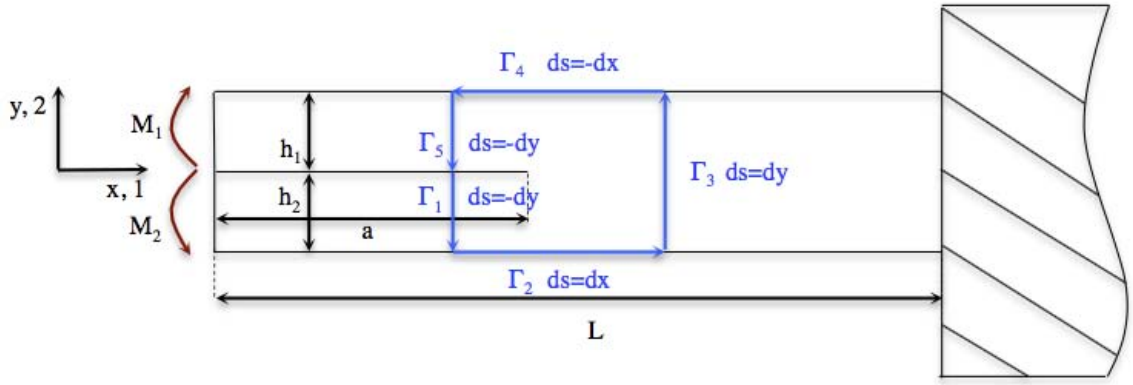

Figure 3.1: Schematisation of the geometry used in the ABAQUS models.

These equations are implemented in a second MATLAB script and allow the calculation of the mode decomposed ERR

$$\frac{J}{J_{II}}. \tag{3.11}$$

3.2 Case Setup: ABAQUS Model

In this section the main features of the ABAQUS model are outlined.
The geometry that has been implemented is the same that is depicted in Figure 3.1. This is a 2D beam that is fully built in (fixed) at the uncracked end while pure moments are applied to the top and bottom beam of the cracked end. The width B of the beam is 1 m while the length L, the heights of the upper and lower beams h_1 and h_2, as well as the moments applied M_1 and M_2 are different from case to case:

- DCB, $L = 150mm$, $h_1 = h_2 = 5mm$ ($\gamma = \frac{h_1}{h_2} = 1$) and $M_1 = -M_2 = -500Nm$ ($k = \frac{M_2}{M_1} = -1$);
- ELS, $L = 170mm$, $h_1 = h_2 = 5mm$ ($\gamma = 1$) and $M_1 = M_2 = -500Nm$ ($k = 1$);
- FRMM, $L = 170mm$, $h_1 = h_2 = 5mm$ ($\gamma = 1$), $M_1 = -500Nm$ and $M_2 = 0$ ($k = 0$);
- AFRMM, $L = 170mm$, $M_1 = -500Nm$ and $M_2 = 0$ ($k = 0$). h_1 is varied between 1, 2, 3, 4, 6, 7, 8 and 9 mm while $h_2 = 10 - h_1$. γ is, therefore, 1/9, 2/8, 3/7, 4/6, 6/4, 7/3, 8/2 and 9/1)

The material that has been chosen is isotropic and linear elastic with a Young's modulus of 210 GPa and a Poisson's ratio of 0.3. These properties, which are typical of steel, has been chosen because the purpose is to see if the MATLAB

scripts are doing their job (i.e. giving the mode mixity) and not to obtain values for composite materials. More, the choice of an isotropic material instead of an orthotropic one is not a limitation. In fact Mark Conroy [12] reported that "the isotropic solution offers an excellent approximation for mixed mode partitions in elastic orthotropic composite laminates".
For meshing the part a structured orthogonal mesh with quadratic elements in plain strain has been used. More, reduced integration have been selected. For each symmetric case (DCB, ELS and FRMM) five different subset size have been used (2, 5, 10, 25 and 50 elements across half beam thickness) in order to capture the convergence profile. For the asymmetric cases only the mesh size which have 25 elements across half beam thickness has been used. This allows to have enough accuracy and, at the same time, it doesn't require an high computational cost.
The ABAQUS are reported, for each case, in Appendix A.

3.3 DCB

For the DCB case the analytically computed total ERR is $G_{ANA} = 103.999997 J/m^2$. This can be computed via equation

$$G_{ANA} = \frac{M_1^2(1+\gamma)^3}{16BEI}\left[\frac{1}{\gamma^3} + k^2 - \frac{(1+k)^2}{(1+\gamma)^3}\right] \tag{3.12}$$

which is a more convenient way to write the Equation 2.2.
In Figure 3.2 is reported the convergence profile for the total J. In the x axis there is the number of elements across half beam thickness. It is important to notice that, since the beam thickness is constant, the higher is the number of the elements, the lower is the size of each of them. In the y axis there is the %error which is defined as

$$\%\text{error} = \frac{G_{ANA} - J}{G_{ANA}} 100\% \tag{3.13}$$

As we can see, the error decrease as the number of elements increases and thus convergence is observed.
Regarding the mode partition, $J_I \simeq J$ and $J_{II} \simeq 0$ up to the tenth decimal digit for all the mesh sizes. This is correct since, as it was reported in §2.7.1, the DCB test is used to determine the pure mode I fracture toughness (i.e. $G_I = G$ and $G_{II} = 0$, as this is the case).

3.4 ELS

For the ELS case the analytically computed total ERR (Equation 3.12) is $G_{ANA} = 77.999998 J/m^2$. In Figure 3.3 is reported the convergence profile for the total J. As we can see, the error decrease as the number of elements increases and thus convergence is observed.
Regarding the mode partition, $J_I \simeq 0$ and $J_{II} \simeq J$ up to the eighteenth decimal

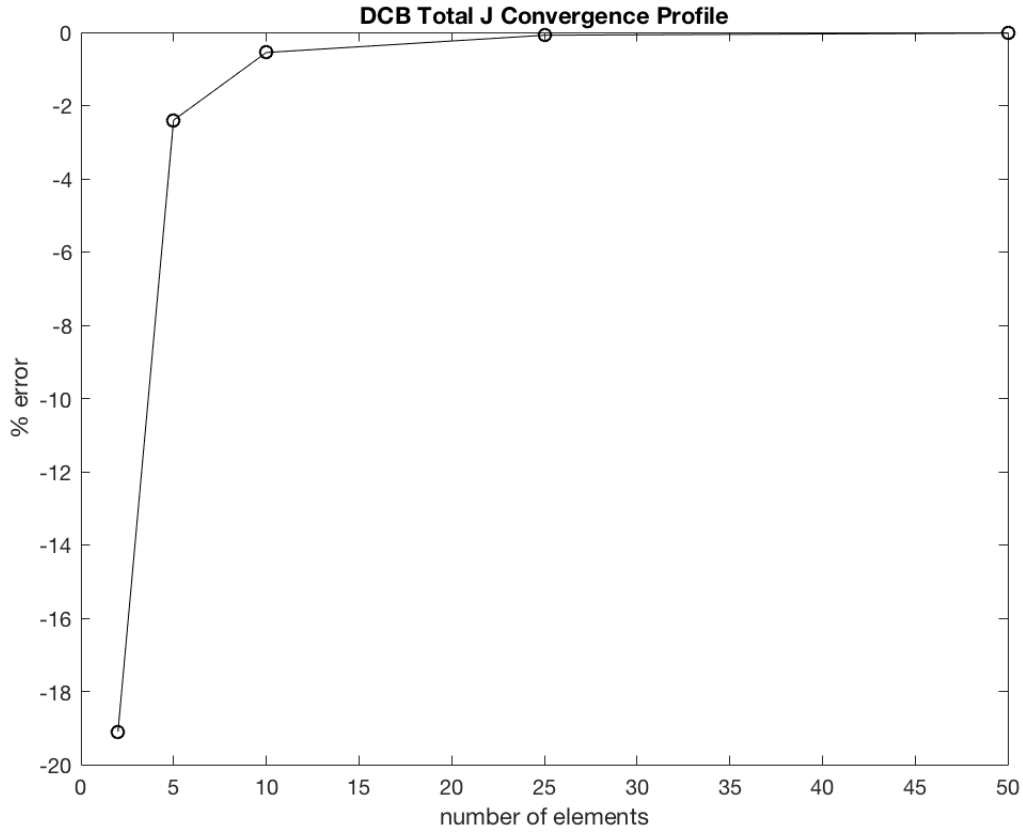

Figure 3.2: Convergence profile for the numerically computed total G (which is J) in the DCB case.

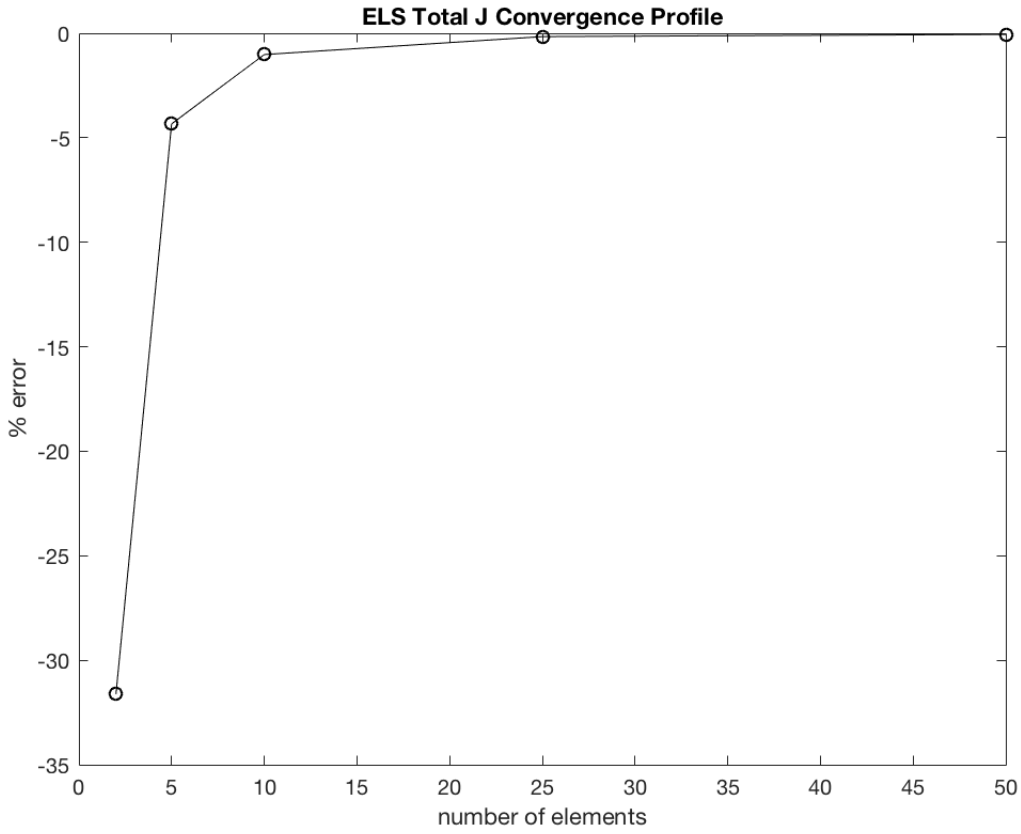

Figure 3.3: Convergence profile for the numerically computed total G (which is J) in the ELS case.

digit for all the mesh sizes except the coarsest (2 elements). This is correct since, as it was reported in §2.7.2, the ELS test is used to determine the pure mode II fracture toughness (i.e. $G_I = 0$ and $G_{II} = G$, as this is the case).

3.5 FRMM

For the FRMM case the analytically computed total ERR (Equation 3.12) is $G_{ANA} = 45.499999 J/m^2$. In Figure 3.4 (solid line) is reported the convergence profile for the total J. As we can see, the error decrease as the number of elements increases and thus convergence is observed.
In Figure 3.4 (dashed line) is also depicted the convergence profile for the mode partitioning $\frac{J_{II}}{J}$. As the as the number of elements increases, the partition approaches $\frac{3}{7}$, which is correct for the FRMM case (§2.7.3).

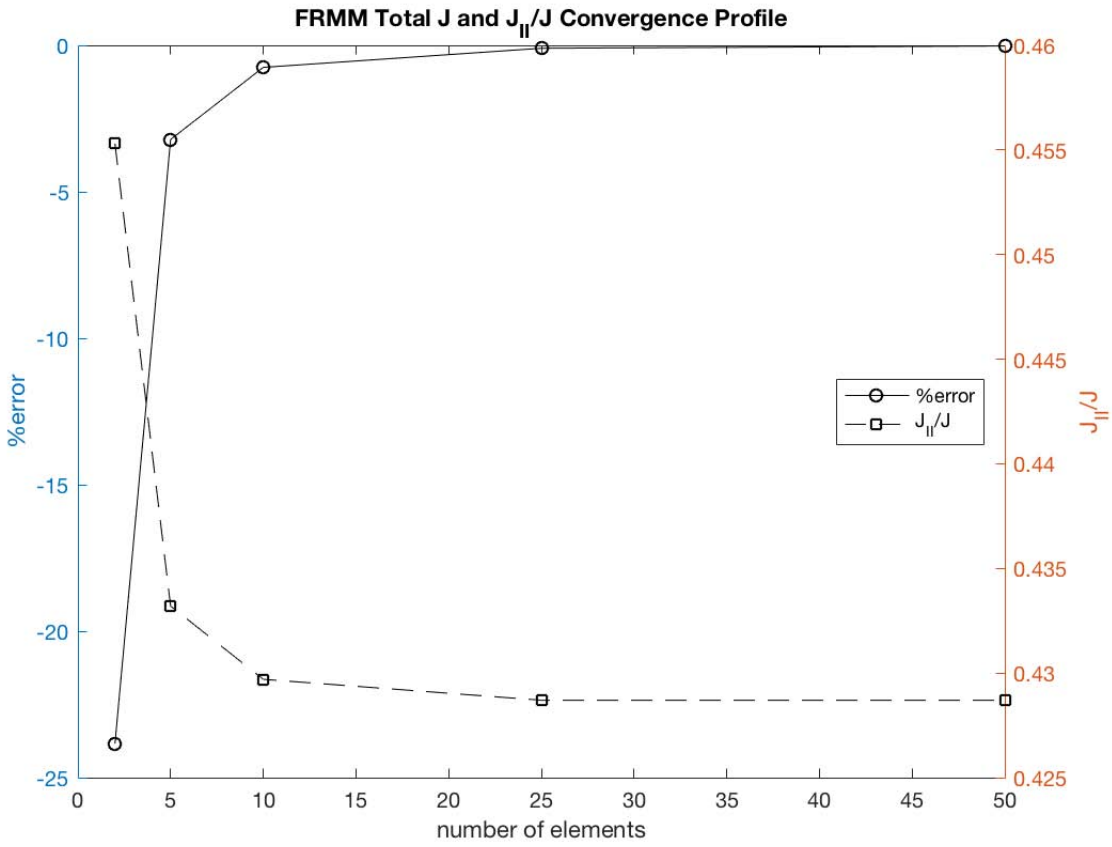

Figure 3.4: Convergence profile for the numerically computed total G (which is J) (left y axis) and for the mode partition $\frac{J_{II}}{J}$ (right y axis) in the FRMM case.

γ	G_{ANA} $[J/m^2]$	J $[J/m^2]$	$\%error$
1/9	6493.5000	6700.622264	−3.1897
2/8	806.0000	812.7268	−0.8346
3/7	234.2407	235.2165	−0.4166
4/6	95.0625	95.3030	−0.2530
5/5	45.5000	45.5452	−0.0993
6/4	23.5926	23.5304	0.2636
7/3	12.4504	12.3990	0.4128
8/2	6.1953	6.1528	0.6860
9/1	2.4163	2.3785	1.5644

Table 3.1: Total G (G_{ANA}), total J and %error for the various AFRMM geometries.

3.6 AFRMM

As stated §3.2, the eight AFRMM cases were run using only the second thinnest mesh size (i.e. 25 elements) which provides enough accuracy. The Table 3.1 compares the numerically computed total J with the analytically calculated total G (G_{ANA}, Equation 3.12). As we can see, the error is small enough but much higher than in the symmetric cases. This is due to the fact that, since the contour needs to be symmetrical, the integration has to be performed having one of the horizontal path that is internal to the beam. This doesn't happen in the symmetrical cases where both the horizontal parts of the paths can be chosen to coincide with the outer surfaces of the beam. The error in the cases 1/9 and 9/1 is instead more related to the mesh size that brings to have only five elements across the thinnest beam. A finer mesh size would have probably helped to reduce the error but, since the aim of these models is only to see if the scripts are working well, it is useless to further reduce the element size.
Regarding the mode partition (Figure 3.5), we can see that the numerical results are very close to those predicted by Hutchkinson and Suo. This not surprising since this is a purely elastic case and a K-dominant region, which matches all the assumptions made by Hutckinson and Suo, exist at the crack tip. It is interesting to notice that the differences that exist between the numerical solutions and the analytical ones is due both to numerical errors and to approximation in the derivation of the analytical solution. In fact, in the symmetric case (5/5, $\gamma = 1$) the numerical solution and the analytical prediction are the closest because the last one is exact and, therefore, the only error present is the numerical.

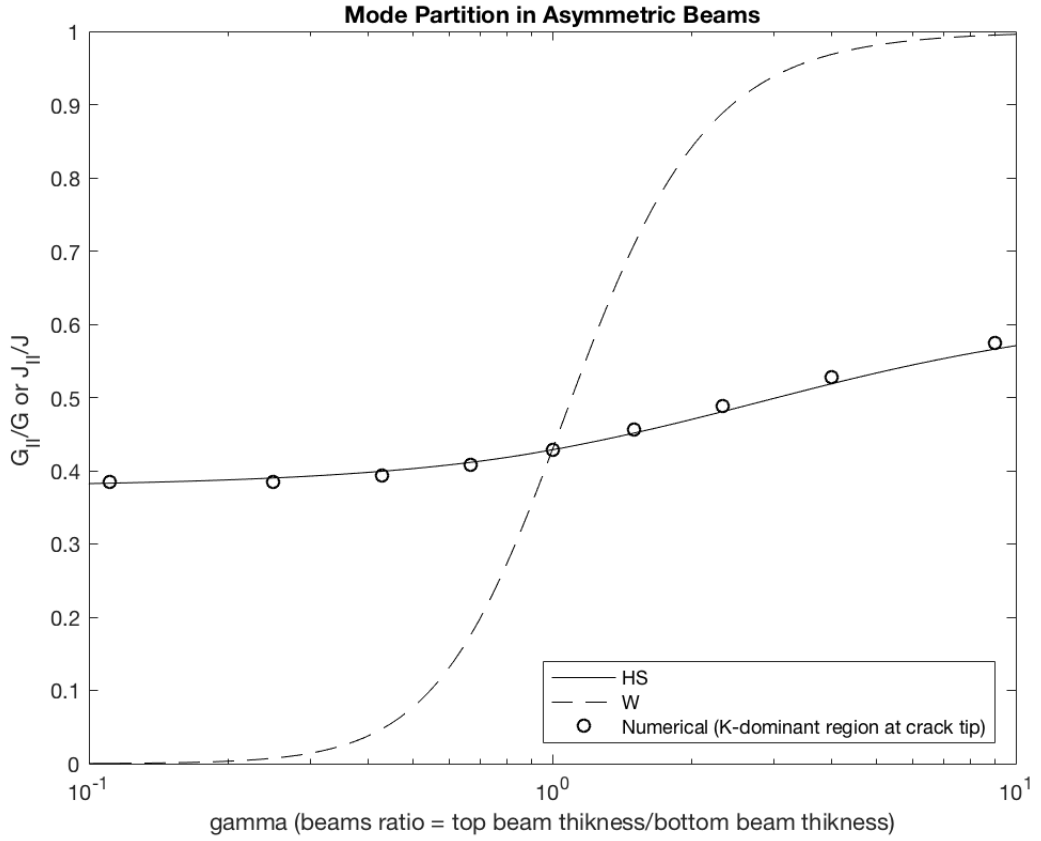

Figure 3.5: Mixed mode partition. Comparison between the analytical predictions ($\frac{G_{II}}{G}$) from Williams (dashed line) and Hutckinson and Suo (solid line) and the numerically computed ($\frac{J_{II}}{J}$, circles)

3.7 Cohesive Zones Models (CZM)

[2] Up to now, the scripts that have been developed proved to work well when a singular stress and strains exist at the crack tip. However, in reality, the stress and strains which develop at the crack tip are limited. The cohesive zones allow to simulate this by introducing predefined stress-displacement relation which is known as cohesive law. The application of a cohesive zone produce an extended crack tip region where the surfaces are kind of bounded together. To separate them some work must be done, according to the stress-displacement relation, and this work can be equated to the fracture toughness of the material [12].
The cohesive zones are a powerful tool because they can represent many different fracture processes/mechanisms by a simple traction-displacement curve. Depending on the case, the traction-displacement law can represent voids formation and coalescence, shear bending, micro-cracking, fibre bridging and many others. These are all types of damage that can occur in the zone above the crack tip. It can be therefore concluded that the cohesive zones are used to model damage.
In order to implement in ABAQUS the cohesive zones, it is necessary to create a layer of cohesive elements between the two parts that will separate as the crack grows, and then to assign a cohesive response to this layer of special elements.

3.7.1 Coupled Linear-Softening Cohesive Zone Model

The Coupled Linear-Softening Cohesive Zone Model is already implemented in ABAQUS and it is used in this work to model linear elasticity with damage. The formulation of this CZM is shown in Figure 3.6.
In order to understand better how the CZM works, it is better to consider first only what happens in the direction normal to the crack plane (opening mode, I) to one single cohesive element experiencing a pure traction stress. In Figure 3.7 is depicted the corresponding traction-separation law which is characterised by:

- the peak strength t_{NC};
- the penalty stiffness K_N;
- the fracture energy G_{IC}.

All these values have to be given as input in ABAQUS. At the beginning we are in the first (rising) part of the curve. The traction load is increasing but is lower than t_{NC}. Since the slope of the curve K_N is usually very high ($K_N >> E$) the element stretches only a few ($\delta \approx 0$). Then, when the load reaches maximum, the damage starts (point ($\delta_{N,init}$,t_{NC}) in the graph). From this point forward the damage evolves following a linear softening law

$$t_N = (1 - d)\bar{t}_N \tag{3.14}$$

[2] For the theory of the CZM I referred to [12], [25], [26] and to some personal notes.

where d is a damage variable which is monotonically increased from zero (undamaged) to one (fully damaged) and $\bar{t}_N$ is the traction predicted by the penalty stiffness

$$d = \frac{\delta_{N,fail}(\delta - \delta_{N,init})}{\delta(\delta_{N,fail} - \delta_{N,init})} \tag{3.15a}$$

$$\bar{t}_N = K_N \delta \tag{3.15b}$$

Basically, during the damage evolution, what is happening is that the element is stretching more and more and simultaneously the load on it is decreasing. When the displacement/separation reaches $\delta_{N,fail}$ the element "breaks" and the two surfaces, that were initially bonded by it, are now separate. Either the value of $\delta_{N,fail}$ or the fracture energy G_{IC} can be specified. In the first case we talk of displacement control, while in the second case we talk about energy control. The latter is used in this work. Knowing that the fracture energy is the area below the traction-separation curve it is possible to calculate the failure displacement and, therefore, know when the cohesive element can be considered to be broken. All of this concerns the normal behaviour of a cohesive element undergoing a pure traction. In the general, however, the element experiences both traction and shear stress at the same time (mixed mode). This is the case of the CZM represented in Figure 3.6. The behaviour of the element up to the point of initiation is governed no more by one, but by two penalty stiffnesses: K_N for the normal direction (K_{yy} in Figure 3.6) and K_S for the shearing direction (K_{xx} in Figure 3.6).

$$t_N = K_N \delta_N \tag{3.16a}$$

$$t_S = K_S \delta_S \tag{3.16b}$$

Furthermore, since we don't have a pure traction stress, we cannot say that the damage of a certain element starts when t reaches t_{NC}. For this reason a damage initiation criterion has to be employed. In this work we used a quadratic damage initiation criterion, which accurately predicts delamination onset in composite laminates [27].

$$\left(\frac{\langle t_N \rangle}{t_{NC}}\right)^2 + \left(\frac{t_S}{t_{SC}}\right)^2 = 1 \tag{3.17}$$

where T_N and t_S are the normal and the shear stress in the cohesive element and t_{NC} and t_{SC} are the stress values for damage initiation in pure opening (I) and pure shearing (II) mode. The angle brackets indicate that compressive normal stress doesn't contribute to the criterion which means that if $T_N \geq 0$ then $\langle t_N \rangle = t_N$, else $\langle t_N \rangle = 0$. Regarding the damage evolution the Equations 3.14

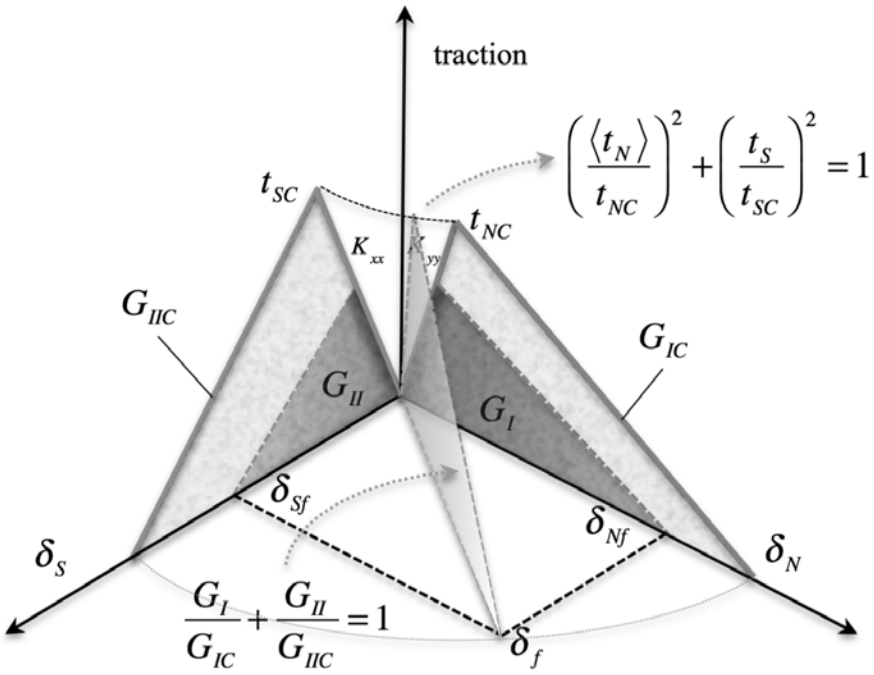

Figure 3.6: Coupled Linear-Softening Cohesive Zone Model (from [12])

and 3.15 (a) and (b) become

$$t_N = (1-d)\bar{t}_N \text{if} \bar{t}_N > 0 \text{else} t_N = \bar{t}_N \tag{3.18a}$$

$$t_S = (1-d)\bar{t}_S \tag{3.18b}$$

$$d = \frac{\delta_{fail}^{eff}(\delta^{eff} - \delta_{init}^{eff})}{\delta(\delta_{fail}^{eff} - \delta_{init}^{eff})} \tag{3.18c}$$

$$\bar{t}_N = K_N \delta^{eff} \tag{3.18d}$$

$$\bar{t}_S = K_S \delta^{eff} \tag{3.18e}$$

$$\delta^{eff} = \sqrt{\delta_N^2 + \delta_S^2}. \tag{3.18f}$$

where δ^{eff} is the overall effective displacement, δ_{fail}^{eff} is the effective displacement at failure and δ_{init}^{eff} is the effective displacement at damage initiation. Similarly to the penalty stiffnesses and to the damage initiation criterion, also a mixed mode failure criterion is necessary. The following (linear) failure criterion has been used in this work

$$\left(\frac{G_I}{G_{IC}}\right) + \left(\frac{G_{II}}{G_{IIC}}\right) = 1 \tag{3.19}$$

where G_I and G_{II} are the energies dissipated in mode I and mode II up to that point and G_{IC} and G_{IIC} are the pure mode fracture toughnesses.

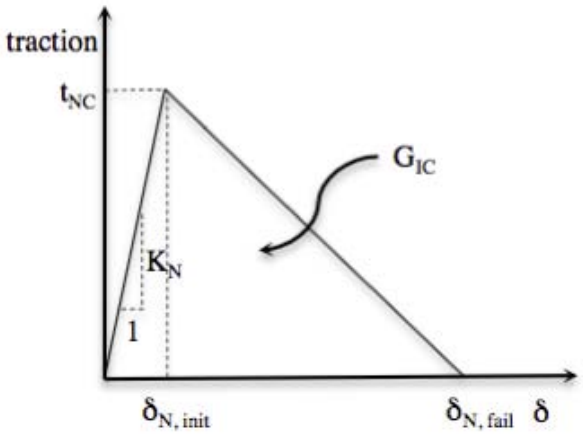

Figure 3.7: Coupled Linear-Softening Cohesive Zone Model, focus on the normal (opening) behaviour.

3.7.2 Case Setup: ABAQUS Model

The AFRMM geometry is the only one modelled using the cohesive elements. For the symmetric cases in fact the mode partition is known exactly and it doesn't change if some damage is introduced. On the other hand, for the asymmetric cases, the mode partiton is not know exactly. In §3.6 we have seen that, if a K-dominant region exist at the crack tip, the numerical solutions approach the predictions from Hutchinson and Suo. Mark Conroy [12] reported that, when damage is introduced at the crack tip (that is what happens in real cases), the numerical solutions tend to move towards the values predicted by Williams. The aim of this part of the work is to test the script for the mode partition in order to see if it is able to pick up this movement towards Williams.
In order to obtain the data of the fields to feed in the MATLAB script, the 2D ABAQUS model ($B = 1m$) that is depicted in Figure 3.8 has been developed. Two steel beams ($E = 210GPa$, $\nu = 0.3$) of length $L = 170mm$ are bonded together using a layer of zero thickness cohesive elements of length $L_2 = 90mm$. Therefore a initial crack of length $L_1 = 80mm$ exist between the two beams. The heights of the top (h_1) and bottom (h_2) beams vary as in the singular AFRMM case (§3.6). The properties assigned to the cohesive element layer are:

- element type, COH2D4 (necessarily linear, the quadratic option cannot even be selected);
- penalty stiffnesses, $K_N = K_S = 10^{15}Pa$;
- damage initiation (opening and shear strengths), $t_{NC} = t_{SC} = 60MPa$;
- failure criterion (mode I and II fracture toughnesses), $G_{IC} = G_{IIC} = 200J/m^2$.

As we can see the fracture toughness is low for a steel. We can think about this setup as two steel bars that are sticked together using a low quality glue. For the beams a structured orthogonal mesh with quadratic elements in plain strain

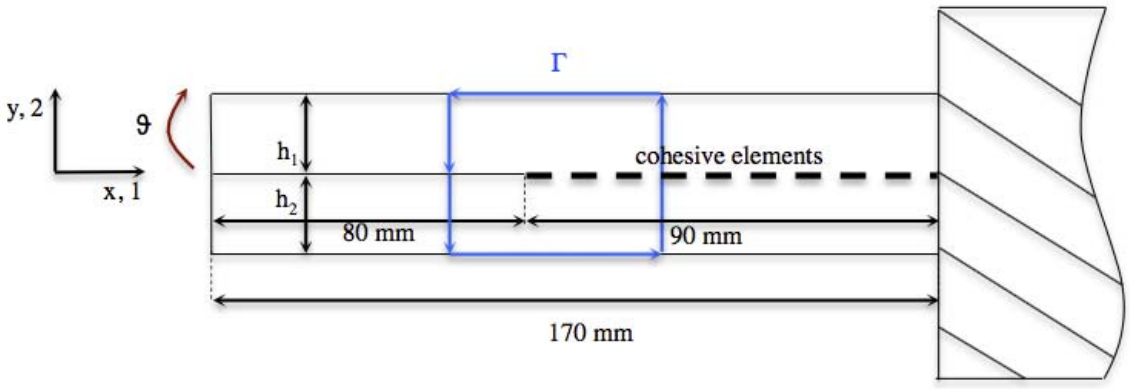

Figure 3.8: Schematisation of the geometry used in the AFRMM ABAQUS model with the cohesive elements.

(CPE8R) has been used. Moreover, reduced integration have been selected. The size of the mesh is the one that allows to have 25 elements across half beam thickness and is the same for the cohesive layer. A rotation of $\vartheta = \frac{\vartheta_C}{2}$ is applied to the top beam. ϑ_C is the angle that causes crack propagation and is given by

$$\vartheta_C = \frac{M_C}{E}\left(\frac{L_1 + x}{I_1} + \frac{(L_2 - x)(1 + k)}{I_1 + I_2}\right) \tag{3.20}$$

where x is the measure of the crack length (initially at zero), L_1 and L_2 are the initial cracked and uncracked lengths, I_1 and I_2 are the second momert of area of the top and the bottom beams ($I_1 = \frac{Bh_1^3}{12}$, $I_2 = \frac{Bh_2^3}{12}$) and M_C is the moment required to apply a ERR equal to the fracture toughness and can be worked out from

$$M_C = \sqrt{\frac{B^2 EG}{6}\left(\frac{1}{h_1^3} - \frac{1}{(h_1 + h_2)^3}\right)^{-1}} \tag{3.21}$$

reminding that G has been set to be $200 J/m^2$.

3.8 AFRMM With Cohesive Elements

The Table 3.2 shows the values of the applied rotations for each AFRMM geometry. In Figure 3.9 are reported the numerically calculated energy partitions ($\frac{J_{II}}{J}$) together with the analytical predictions of Williams and Hutchkinson and Suo. As we expected, the numerical partitions are no more close to Hutckinson and Suo but they have shifted towards Williams. This means that the scripts are able to get the mode partition even when a damaged region exist at the crack tip, which is the most general (real) case. However it is important to point out two things. First, since the fracture hasn't initiated ($\vartheta = \frac{\vartheta_C}{2} < \vartheta_C$), the damage at the crack tip is not fully developed. If the crack had started, the numerical

γ	ϑ_C $[rad]$
1/9	0.183
2/8	0.066
3/7	0.039
4/6	0.030
5/5	0.027
6/4	0.026
7/3	0.025
8/2	0.024
9/1	0.028

Table 3.2: ϑ_C for the various AFRMM geometries (γ).

partitions would have been more shifted towards Williams. However, making the crack to propagate requires a much much higher computational cost which is not necessary for this part of the work whose aim is only to observe the shifting of the mode partitions. Second, if an higher value of the toughness had been chosen and/or a lower value of the opening and shear strength had been set, the movement of the numerically calculated mode partitions would have been even more important.

3.9 Chapter Conclusions

In this chapter we saw that the scripts which have been developed are able to pick up the correct total ERR. In the symmetric cases also the mode partition is calculated with an excellent accuracy. In the asymmetric (singular) cases the mode partition suffers a higher error which is anyway acceptable. Regarding the mode partition the scripts are able to pick up the correct mode partition in all the symmetric cases (negligible error, less than 1%) and also in the singular asymmetric ones (partitions close to Hutckinson and Suo). Finally the introduction of some damage at the crack tip brings the mode partitions to shift towards Williams, which is exactly what was expected.
It can be therefore concluded that the scripts are ready to be employed using experimental data from DIC.

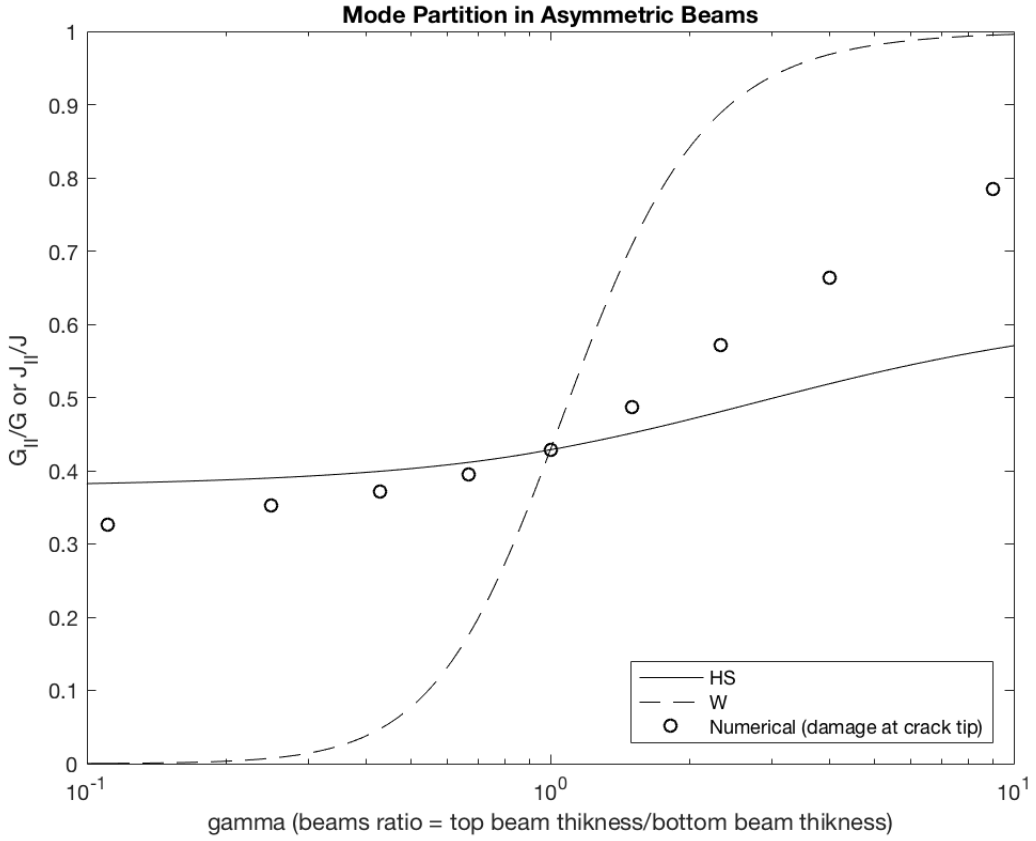

Figure 3.9: Mixed mode partition. Comparison between the analytical predictions ($\frac{G_{II}}{G}$) from Williams (solid line) and Hutckinson and Suo (dashed line) and the numerically computed ($\frac{J_{II}}{J}$, circles)

Chapter 4

Materials and Methods

In the first part of this chapter the materials used and the procedure followed for manufacturing the samples are exposed. Then, in the second part, the testing method is reported and the machines that were employed are described with particular attention to the Digital Image Correlation (DIC) machine.

4.1 Specimens Manufacturing

4.1.1 Material

The material that has been used for the experimental part of this work is a unidirectional (carbon/epoxy) composite [28]. The material is provided in the form of a roll of preimpregnated (prepreg) tape which is stored in a freezer at -18°C. In the freezer it has a shelf life of 12 months. After being taken out from the freezer the layup has to be done within 10 days and the curing process at last after 30 days.
The matrix HexPly®8552 is a very tough resin which is used primary in aircraft structures.

4.1.2 Layup Procedure

The prepreg is removed from the freezer and 66 sheets are cut using scissors. The size of the sheets depend on the size of the samples and on how many samples one wants to obtain from the panel. The day after the sheets are laid on top of each other by hand with the fibres aligned in the same direction. After having laid up the 10^{th}, 20^{th}, 30^{th}, 36^{th}, 46^{th}, 56^{th} and 66^{th} sheet the layup is debulked for 45 minutes in order to remove any air pocket. Between the 33 rd and the 34^{th} layer a thin (12 μm) PTFE sheet is placed in order to produce a precrack of 60 mm and 80 mm when the DCB and ELS or FRMM samples are cut[1]. The debulking procedure is illustrated in Figure 4.1. The layup is placed on an

[1]Only symmetric samples have been manufactured and tested. Unluckily there was no time left for producing and testing any asymmetric sample. This was due to all the (many) unexpected problems found in using the DIC equipment.

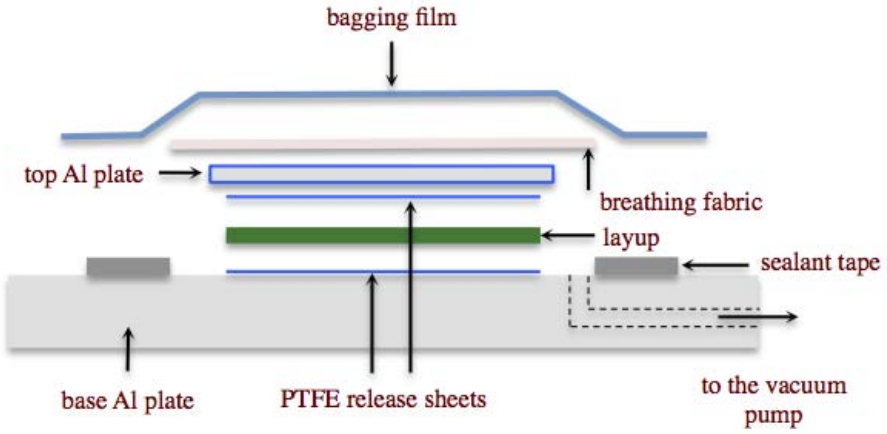

Figure 4.1: Illustration of the layup for the debulking.

Aluminium base plate and protected by a thick PTFE release film on both sides. A second Aluminium plate, covered by a PTFE sheet, is placed on the top of the layup. This allows to uniformly distribute the pressure on the whole layup. After, a breathing fabric, which allows the vacuum to reach the entire layup, is placed on the Aluminium plate. The layup is then covered with a bagging film and sealed around all edges using a sealant tape. The base plate is then attached to a vacuum pump. After making sure there are no leaks between the sealant tape and the bagging film, the vacuum pump is left on for debulking for 45 minutes.

4.1.3 Curing Process

After the last debulking (66^{th} layer) the layup is ready for the curing process. The two PTFE sheets that were preventing the direct contact of the layup with the mould are replaced and between them and the layup two sheets of release ply are placed. The release ply helps to provide a consistent surface finish on the top and bottom of the cured composite. Then edge dam tape is placed around the layup to prevent the resin from leaking (this is only for scruple since the material is prepreg and resin leaks shouldn't occur). Subsequently, the same Aluminium plate covered by a PTFE sheet that was used during the debulking, is put on the top of the layup. This helps to distribute the downward pressure in the pressclave. It is important to notice that none of the previously mentioned items should cover the vacuum holes that are present in the base plate. After this, the breathing fabric is placed so that it covers the layup and also the vacuum holes. Similarly to the debulking, a bagging film is closing off the layup, this time with high temperature sealant tape all around it. Again the vacuum is checked for leaks. Other high temperature sealant tape is placed along the edges of the base plate in order to seal it with the top lid. At this point the top lid is placed on the top of the base plate and the complete unit is inserted into the pressclave. The hydraulic press is then lowered and a force of 500 kg is applied. This force pushes the top lid against the bottom plate and allows to create a sealed chamber in

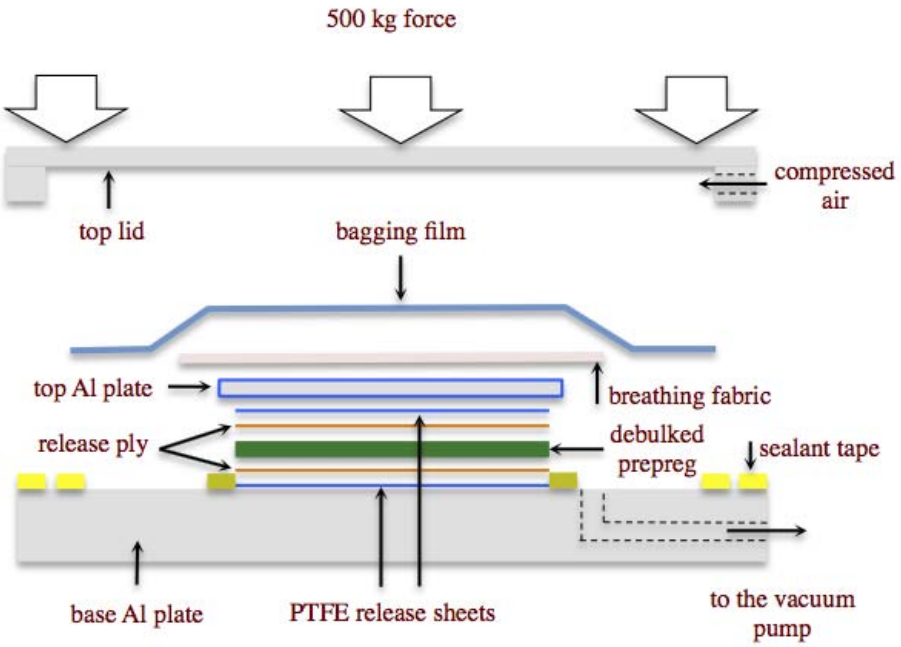

Figure 4.2: Illustration of the layup for the curing process.

between. After this, pressurised air is introduced in the sealed chamber though a pipe. This is necessary for consolidating the laminate during the curing process. The vacuum pump is then switched on to create the vacuum under the bagging film. A schematisation of the layup for the curing process is provided in Figure 4.2.

As last thing, the curing cycle is programmed and the heaters are switched on. The curing cycle that has been used is reported in Figure 4.3. When the curing cycle is ended and the temperature is below 80°C, first the vacuum pump, then the compressed air and finally the pressclave are switched off. The system is then left to cool overnight to enable handling mould and the material. As can be seen, the curing cycle takes 250 minutes. After this time the heaters automatically switch off and the cooling phase starts. Since the mould is not equipped with any special cooling system, the cooling takes place "naturally". From one side this is good because the cooling rate is low (between 0.1 and 1 °C/minute, [11]) and thus no thermal stress are introduced in the cured panel. From the other side this means that at least 4 hours are required, after the end of the curing process, for the temperature to go below 80°C.

The day after the pressclave is risen and the unit is removed. The top lid is lifted off the base plate by removing the outer sealant tape. Then the other tapes and sheets are removed to extract the cured composite panel.

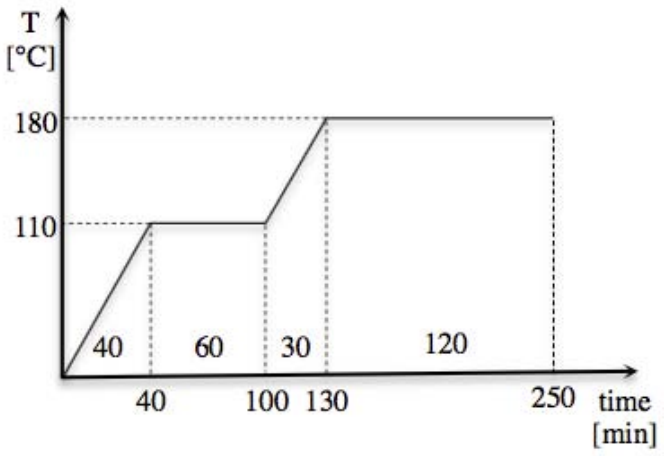

Figure 4.3: Graph showing the curing cycle that has been used to manufacture the composites.

4.2 Specimens Preparation

The specimens are cut from the cured panel using a diamond blade. The width of the disc has to be taken into account when planning the number of specimens. All the samples have a thickness around 10 mm and a width of 25 mm. The length depend either the samples are DCB or ELS/FRMM. The DCB samples have a length of 150 mm with a precrack (measured from the edge of the sample) of 60 mm. The ELS and the FRMM sample instead have a length of 170 mm and a precrack of 80 mm. After the cutting, the specimens are cleaned and load blocks are glued to them. For the DCB samples two load blocks are necessary, one is attached to the top and one to the bottom since the load must be applied symmetrically (opening). For the ELS and the FRMM samples, instead, one block is sufficient. In the ELS the load is applied to the bottom beam (and pushes upwards), therefore the load block must be attached to the bottom beam. In the FRMM the load is applied to the top beam (and pull upwards), therefore the load block must be attached to the top beam.
Normally the surface of the samples is painted completely with a white paint and vertical lines are drown at know distances from the original crack tip position in order to follow the crack growth during the tests. In this case the samples are tested using the DIC and, as will be explained later, a very thin paint pattern is needed for the software to pick up the displacements and the strains. To make the surface as flat as possible the observed zone of the samples is polished using first a coarse (P200) and then a thin (P600) sandpaper.

4.3 Test Methods

The tests were performed using a screw-driven Tinius-Olsen testing machine with a 10 kN load cell. The same programmed test method is used for all the tests, which is a displacement-controlled method with a steady upward motion of the

load cell attached to the load block, at 2 mm/min. The Figure 4.4 shows the rig for the DCB (a), ELS (b) and FRMM (c) tests. The test is divided into two parts: the test from the insert (opening) and the test from the precrack. At the beginning the samples contain a thin PTFE sheet that acts as crack starter. Its thickness, however, (12 μm) is not small enough and the crack cannot be considered a physical one. Thus, in order to obtain a "real" crack, the samples must be "opened"; which means to let the PTFE sheet to start the crack and allow it to propagate for 5 mm. After this the samples are referred as "opened" and the second part of the test (from the precrack) can take place. This is the real part of the test during which 60 mm for DCB, and 30 mm for ELS and FRMM samples of crack propagation must be observed, as prescribed by the norms [21], [22] and [23]. In the case of this work the length of crack propagation that can be monitored is limited by the use of the DIC. The observed length is therefore reduce, case by case, according to the area that can be captured by the cameras (which depends on may factors that will be discussed later in this work).

4.4 DIC - Digital Image Correlation

4.4.1 Principle of DIC

DIC is an acronym for Digital Image Correlation and is a non-invasive technique to measure deformations of a sample by just studying images taken from it [29]. If the sample has no visible features that follow the deformation it is necessary to paint it with speckles. The resulting surface pattern must follow the sample deformation and shouldn't alter it. High resolution digital cameras are used to take a series of images over time. A computer then analyses these images and calculates the displacement field taking place in the sample. From the displacement field then the strain field (and many other fields) can be derived.
When one camera is used to record the images only a 2D deformation field can be obtained. The machine works in this way:

- The camera images of the pattern which has been painted on the sample surface;
- The software takes this image and discretises it into smaller sub-cells called facets (Figure 4.5);
- More images are taken over time during which the sample surface displaces and deforms (and the pattern with it);
- The pattern within each facet after the displacement/deformation is compared with the pattern within each facet before the deformation. Where the pattern has the best match, this represents the pattern displacement within the facet (Figure 4.6).

The usage of two or more cameras allows the measurement of 3D deformation fields. Even tough the working principle is the same as the one described for the

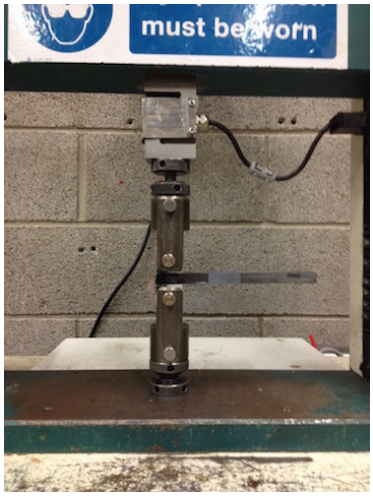

(*a*)

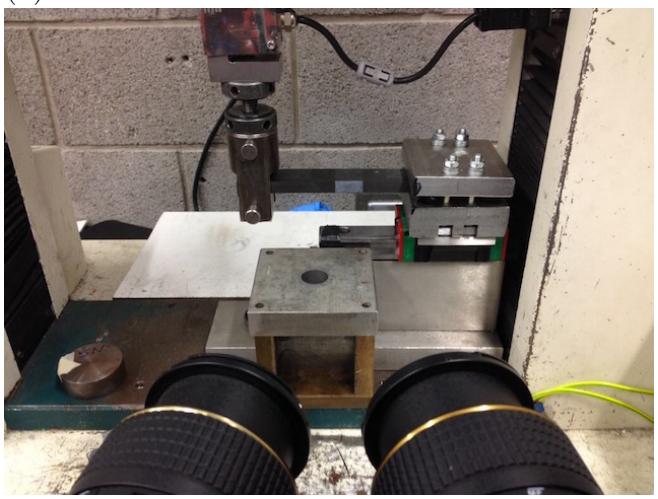

(*b*)

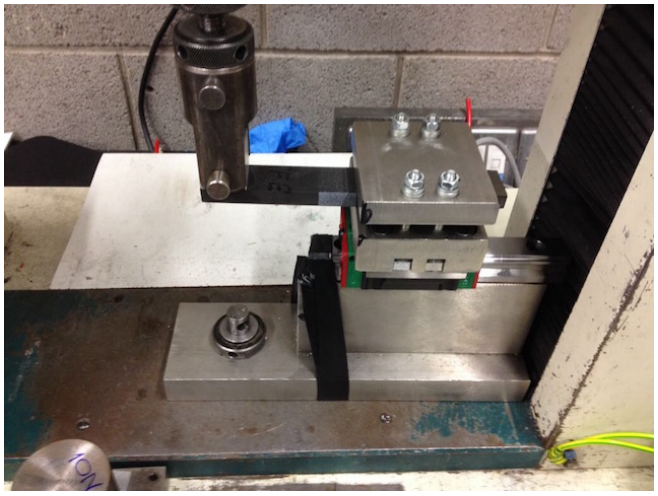

(*c*)

Figure 4.4: Rig for the DCB (*a*), ELS (*b*) and FRMM (*c*) tests.

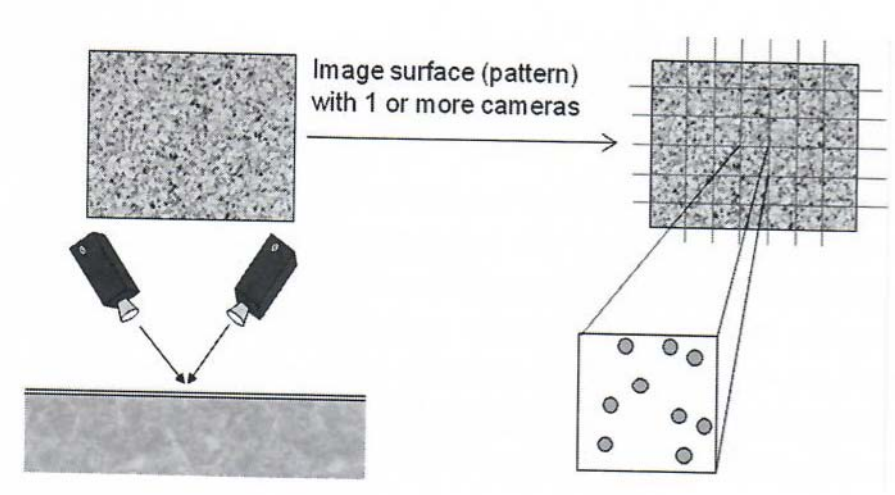

Figure 4.5: Discretisation of the image into smaller sub-cells (from [29])

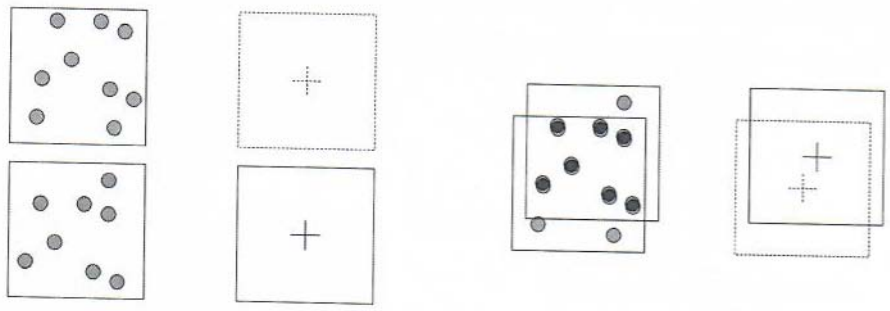

Figure 4.6: Pattern displacement within the facet (from [29])

2D case, there is an extra issue: the same pattern on the sample surface is seen differently by the two cameras. However it is exactly this feature that allows to calculate the height of the surface and thus the z displacements over time.

4.4.2 Hardware Components of the DIC

The DIC equipment that has been used is the StrainMaster Portable from LaVision. The hardware components can be seen in Figure 4.7 and consist of

- two high resolution cameras model Imager M-lite 5M (5 million pixels, frame rates up to 57 Hz);
- two white/blue LED illumination units;
- a central control unit;
- a computer with the software StrainMaster DIC installed on it.

The two cameras, the two lights and the control unit are installed on a rail which is fixed on a tripod. The cameras and the lights can be easily moved on the rail and the tripod can be risen or lowered thanks to a crank. The cameras and the

Figure 4.7: Hardware components of DIC (from [29])

lights are connected to the controller whose aim is to coordinate them with each other. The cameras and the controller are also connected to the computer.

4.4.3 Specimens Preparation for DIC

The samples preparation follows the same steps described in §4.2 with some additional others that are explained in this paragraph.
After the cutting with the diamond blade, the samples have a surface which is very irregular. When performing a "standard" test (i.e. without the DIC) this is not a problem: the surface can be painted with the white paint and the lines for following the crack propagation can be drown. When using the DIC the fact that the surface is not flat might represent a problem: some zones of the surface can reflect more light towards the cameras than others which instead scatter more. The result is that, on the same picture, there are areas which are brighter and areas which are darker and this is not good. The reason is that, since the sample is moving during the test, a point, which is at the beginning in a bright area, could not be recognised as the same point if, during the test, it travels to a darker one. The problem is even worse when, as in this work, two cameras are used: the brightest zones in the picture from camera 1 don't necessarily correspond to the brightest zones in the picture from camera 2 since the two cameras are not aligned. For this reason it is necessary to accurately polish the surface of the sample that we want to observe. For this purpose a polisher has been used, holding the samples with the hand. First a P200 and then a P600 sandblasting paper have been employed until the surface was perfectly flat. After this the surface was washed with water, dried and cleaned with isopropanol. Once the samples are completely dry, the portion of the surface that we wanted to observe was circumscribed using paper tape and the distance between the beginning of the sample and the beginning and the end of the area is recorded (Figure 4.8). The paper tape is necessary to shield the surface of the sample that we are no interested in from being painted. The sample is then painted using a Rust-Oleum Hard Hat white paint. The first samples were painted outside. The sample was placed on the grass and the paint was sprayed vertically on it. The quality of the

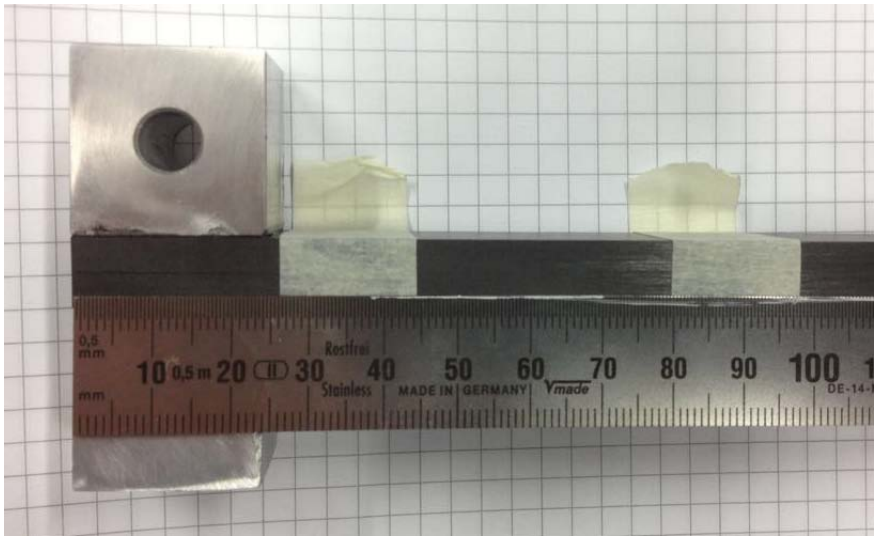

Figure 4.8: A DCB sample with the area of interest circumscribed with tape. The ruler is used to record the distance between the beginning of the sample and the beginning and the end of the area that is going to be painted.

painting was quite good but the distribution of the white dots was not uniform, basically because of the wind. At the end of the experimental campaign the last samples were painted inside holding them with one hand and spraying the paint horizontally from about one meter. The quality of the pattern resulted to be much better not only in terms of distribution because of the absence of wind, but also in terms of uniformity of dots' size because the biggest drops were falling on the ground before reaching the sample.
It is important to notice that the results is strongly influenced by the quality of the painted pattern. Furthermore, the ability of understanding if the pattern is good or not develops with experience. Therefore, at the beginning is better to paint the samples only a few and see how they look like on the DIC. If they are not good enough it is sufficient to paint them a bit more.

4.4.4 Test Method with DIC

When testing a sample using the DIC the procedure that is explained in this paragraph has been followed. Not only is mandatory to do all the steps that are reported but it is also important to do them in the right order (i.e. how they are presented).

- The sample, prepared as explained in §4.4.3, was placed on the traction machine using the rigs according to the test that we wanted to perform.
- The DIC equipment (the tripod with the cameras, the lights and the controller) was placed in front of the sample. The distance between the sample and the cameras has been varied during the experimental campaign.
- The DIC was started following these steps: plug the DIC, switch on the

plug, switch on the controller, switch on the computer, run the StrainMaster software.

- Once on the StrainMaster, the personal workspace (folder) was selected and a new project was created.
- The cameras were set to 10 bit and then focused on the area of interest of the sample. The lights were also adjusted to achieve a good contrast.
- The machine was then calibrated using one of the calibration plates provided by LaVision.
- The capture rate of the images and the recording time were specified together with the name of the recording.
- The reference images were then taken.
- The traction machine and the DIC recording were started at the same time.
- The traction machine and the DIC recording were stopped at the same time.
- After the recording the images were processed giving as input: the interval of the images to be processed, the increment, the area that should be analysed, the subset size in terms of pixels, the calculation method, the accuracy and the name of the processing.
- The images and the data were then visualised and eventually exported.

Of all the steps mentioned above it is important to pay particular attention to the calibration. Once the cameras are focused on the surface of the sample the best contrast possible should be achieved. This has been performed either by playing with the position of the lights, the aperture of the cameras and the exposure time. At this point, one of the calibration plates from LaVision was placed in front of the area of interest of sample so that there was contact between them but trying not to move the sample (otherwise the focus might be lost). When choosing the calibration plate it is important to consider that each calibration plate is able to calibrate a space that is about three times the area of the calibration plate itself. The calibration plate was then removed trying not to move the sample and the calibration was performed by taking three images averaged at a frequency of 4 Hz. After the calibration the machine gives a number which is the residual fit error of the calibration. This number should be lower than 0.5 but the calibration is still good even if it is lower than 1. Since the coordinate system is defined during the calibration it is important to place the calibration plate in the right way. The centre of the calibration plate defines the origin of the coordinate system while the triangle and the square define respectively the positive direction of the x and of the y axis. During the experimental campaign the calibration plate was placed having the serial number in the bottom right corner. In this way the x axis was horizontal and was pointing towards right while the y axis was vertical

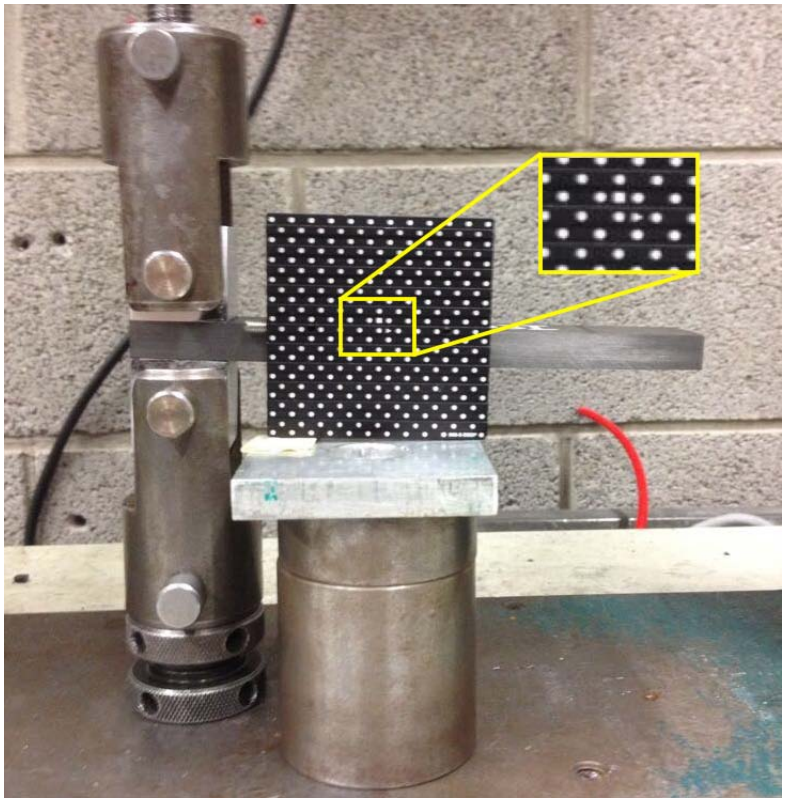

Figure 4.9: Calibration performed on a DCB sample. Note the position of the calibration plate: the triangle and the square correspond to the positive x and y axes respectively (detail).

and was pointing upwards (Figure 4.9, detail). Moreover, in order to have the x axis parallel to the crack, the calibration plate was carefully rotated by placing a piece of tape below the left part of its bottom edge. This turned out to be necessary since the software StrainMaster doesn't allow to move the coordinate system before processing the data. However there is another software, DaVis, which allows to change the coordinate system after the calibration and before the processing of the images. Unluckily, this software became available only at the very end of the experience and there was not enough time left to understand how to use it. The previously described procedure is also reported, with many more details in [31]. However, some features were learnt while performing, with the machine, the first tests that are not reported in this work. These tests were carried out on thinner samples and also many times on the same sample after having re-glued it, this in order to save material which is very expensive. These tests took between two to three months. They didn't bring any result useful for the aim of the work but they allowed us to understand how to use the DIC machine that was new for everybody at UCD. The experience acquired during those first months turned out to be of much use for the real part of the experimental campaign of this project, which is described in the following chapter.

Chapter 5

Testing with the DIC

In this chapter are reported the results of the experiments that have been performed together with details about the experimental setups. The first tests that have been performed are DCB and they gave very wired results (i.e.not consistent with what we expected and with what we saw from the ABAQUS models). The accuracy of the DIC was then assessed and it turned out to be not good enough to pick up the strains that we were interested in. The experimental setup was then modified in order to try to bring the accuracy of the machine as high as possible. Finally DCB, ELS and FRMM tests were performed. These test gave much better results than the first DCB however, some new and unexpected problems were found that didn't allow to use the already developed scripts to get the fracture energy and the mode partition.

5.1 Initial DCB tests

The first tests, that were carried out on samples like those described in §4.2, were four DCB. In particular, each of the four DCB specimens was tested from the insert (opening) and from the precrack. However, as stated in §4.3, since the DIC was used to monitor the crack propagation, the field of view was not wide enough to allow the observation of all the crack propagation at once. For this reason, the so called "test from the precrack" was split into two. Basically with the DIC the opening of the sample and two successive crack propagations were monitored. The samples were therefore painted and polished three times, one for each test. With reference to Figure 5.1, the areas that were observed (and thus painted) and their distances from the beginning of the sample are:

- for the test form the insert: $L_1 = 45mm$, $L_2 = 80mm$, $a_0 = 60mm$;
- for the first test from the precrack: $L_1 = 50mm$, $L_2 = 105mm$, $a_0 = 65mm$;
- for the second test from the precrack: $L_1 = 70mm$, $L_2 = 130mm$, $a_0 = 85mm$.

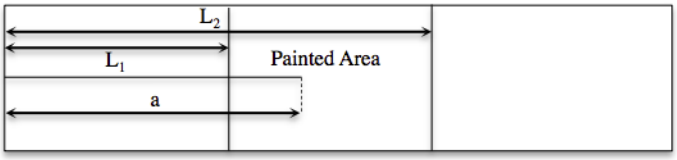

Figure 5.1: Area of the DCB samples that was painted for the observation with the DIC. L_1, L_2 and a are different depending on the fact that the test is from the insert or from the first or second precrack.

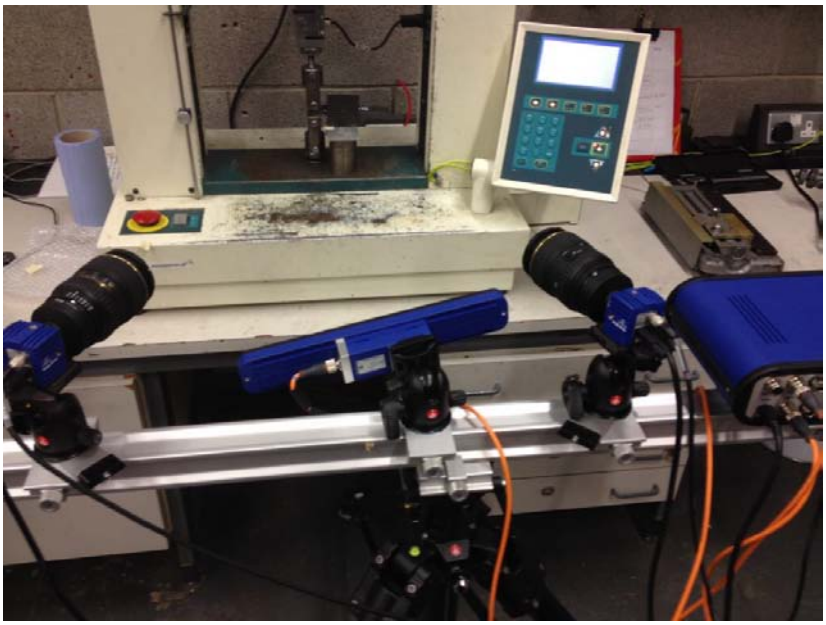

Figure 5.2: Experimental setup used in the first tests.

5.1.1 Experimental Setup

For these first tests, the DIC machine was placed in front of the traction machine so that the distance between the rail and the sample was about 750 mm. The height (i.e. the distance between the rail and the floor) was 950 mm. Regarding the illumination, only one light unit was used. This was placed exactly in front of the sample and fixed horizontally on the rail (Figure 5.2). The aperture of the cameras was set to be 8 or 11 and the exposure time between 40 and 50 ms. The calibration plate that was used is the 058-5-SSDP from LaVision whose size is 58x58 mm.

5.1.2 Results and Comments

The results that are presented in this paragraph regard the stable crack propagation that takes place in the sample number 1 during the first test from the precrack. The displacement field is visualised in Figures 5.3 (u_x) and 5.4 (u_y) while the engineering strain field in Figures 5.5 (ϵ_{xx}), 5.6 (ϵ_{yy}) and 5.7 (ϵ_{xy}). For

the processing the correlation mode was set to be "relative to the first", the calculation mode "accurate" and the subset size 25 pixels. This size is a compromise between two aspects: having at least 3 white dots into each subset and having a sufficiently large number of elements across the thickness of the sample. However, other calculations were performed using smaller and bigger subset sizes but the results were not substantially different.
As we can see in Figures 5.3 and 5.4, both displacements look very smooth and are consistent with what is happening during the test. The load block that is attached to the bottom beam of the sample is fixed and is not moving during the test while the top load block is moved upwards. For this reason we expect to have a y displacement higher for the top beam and lower for the bottom one, but in any case positive. This is exactly what is shown in the Figure 5.4. Moreover, since the two beams are progressively pulled apart (the crack is propagating) and the sample is not constrained in the x direction on its right edge, we expect to have a movement of the sample towards left and, therefore, a negative x displacement. Figure 5.3 is showing this. While the displacement field makes sense considering the experimental configuration, the strain field makes no sense at all. From the ABAQUS model (§3.2) and from [12] we would have expected to see a linear distribution for the axial strain (ϵ_{xx}) across each of the two beams, with the neutral axis being in the middle. Instead, what we can see in Figure 5.5 is basically a random distribution which is absolutely incorrect. Looking now to Figure 5.6 we can see something that as first impression could be amazing: the crack edges are surrounded by colours which means that very big strains are taking place there. This of course doesn't correspond to reality. The fact that the crack edges are painted with colours is only due to the inability of the software to detect the crack propagation. Basically the software is not understanding that there is no more continuity in the material and is therefore stretching a lot the subsets in correspondence of the crack. Therefore, there, very high values of ϵ_{yy} are calculated. Finally, regarding the in plane shear strain this should be zero if pure moments were applied to the beams. However in this case displacements, and thus forces, are applied. According to [14] a parabolic distribution of the ϵ_{xy} should be present in each beam. Looking at Figure 5.7 we cannot detect any distribution: the shear strain seems to be almost uniform except for some "noise" in correspondence of the crack which is due to the same reason explained before. From the previous lines it is clear that the results were completely unsatisfactory and couldn't be used to determine the total G with the new approach (J-Integral). The reasons behind these very bad results might be many:

1. the sample is moving a lot during the test. The displacements linked to the motion are therefore much much higher than those related to the deformation. This can lead to a loss of information about the deformation and thus the strains which then turn out to be only "noise";

2. the testing method that we used requires to apply displacements to the sample instead of pure moments as instead Mark Conroy did using a much more sophisticated machine and bigger samples [12]. Moreover, the resulting applied forces are symmetrical but the displacements are asymmetrical since

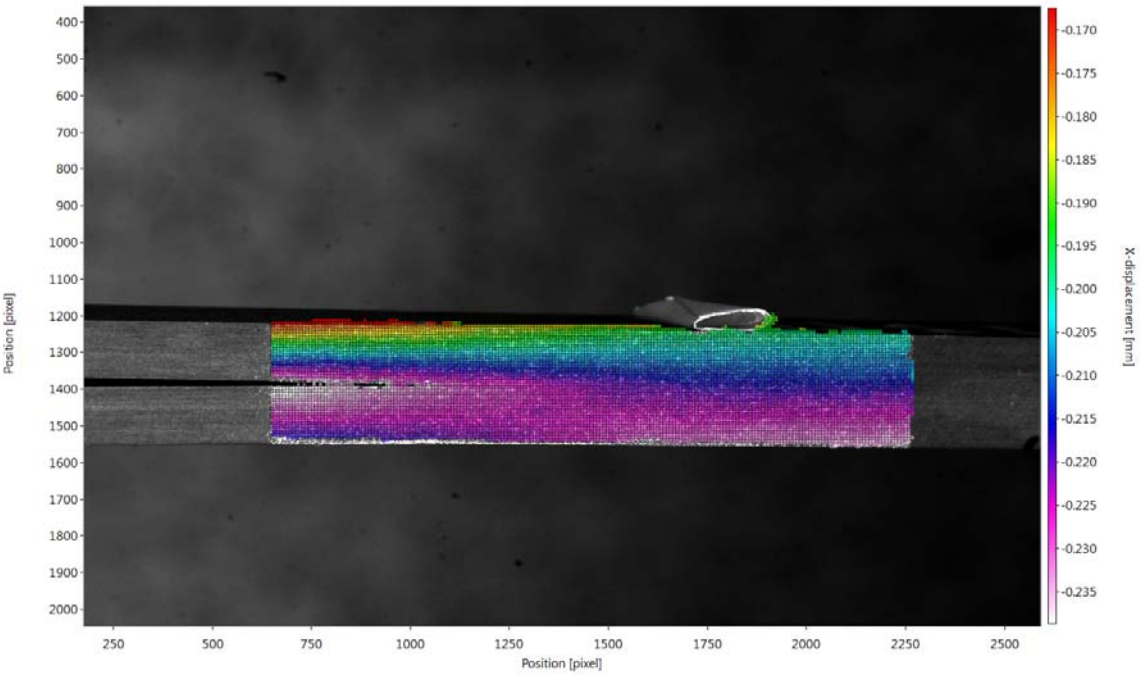

Figure 5.3: DCB, displacement in the x (horizontal) direction u_x.

the bottom load block is fixed while the top load block is pulled upwards with a 2 mm/min speed;

3. the machine might not calculate the strains in the right way;

4. the machine, with this experimental configuration, is not accurate enough to pick up very small strains as those that we expect are ($\epsilon_{xx,MAX}$ around 0.10% (0.001), as reported in [12]). Therefore what we can see from the images is basically only "noise".

It is necessary to understand which of the previous points is or are the real reasons for which we are not obtaining what we expected. Being aware that changing the experimental configuration is not possible, it becomes clear that nothing can be done regarding 1 and 2. In the next paragraphs indeed an investigation about how the strains are calculated by the DIC machine (3) is carried out and the accuracy of the machine with this experimental setup (4) is assessed.

5.1.3 Fracture Toughness and R-Curves

By using the images taken from the DIC it is possible to monitor the crack growth over time. Since the DIC and the traction machine are started at the same time it is possible to associate the increment in crack length to the force and, therefore, to calculate the fracture toughness.

- For each test the images taken from the DIC are analysed and the x position, in terms of pixels, of the crack tip is recorded;

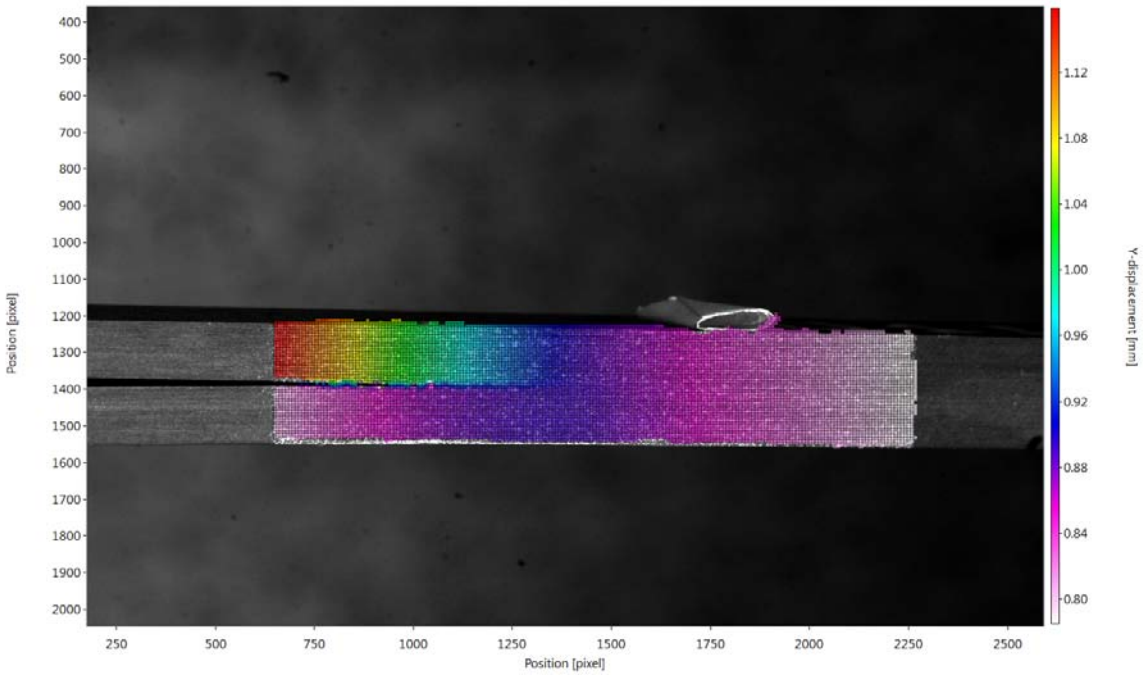

Figure 5.4: DCB, displacement in the y (vertical) direction u_y.

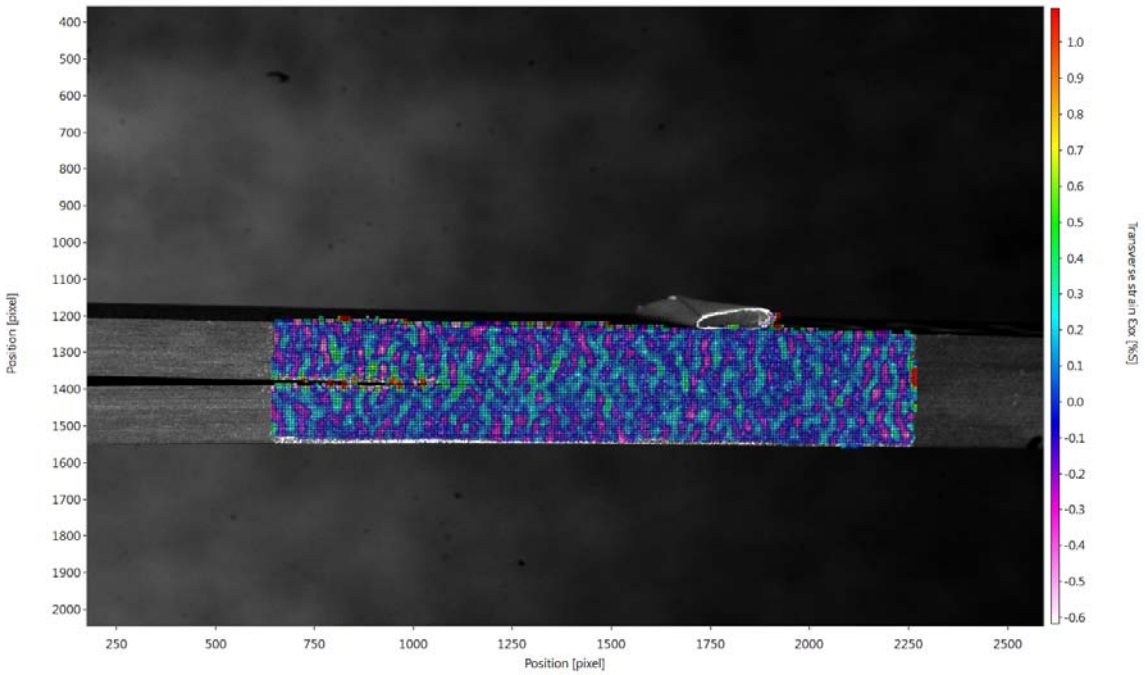

Figure 5.5: DCB, axial strain ϵ_{xx}.

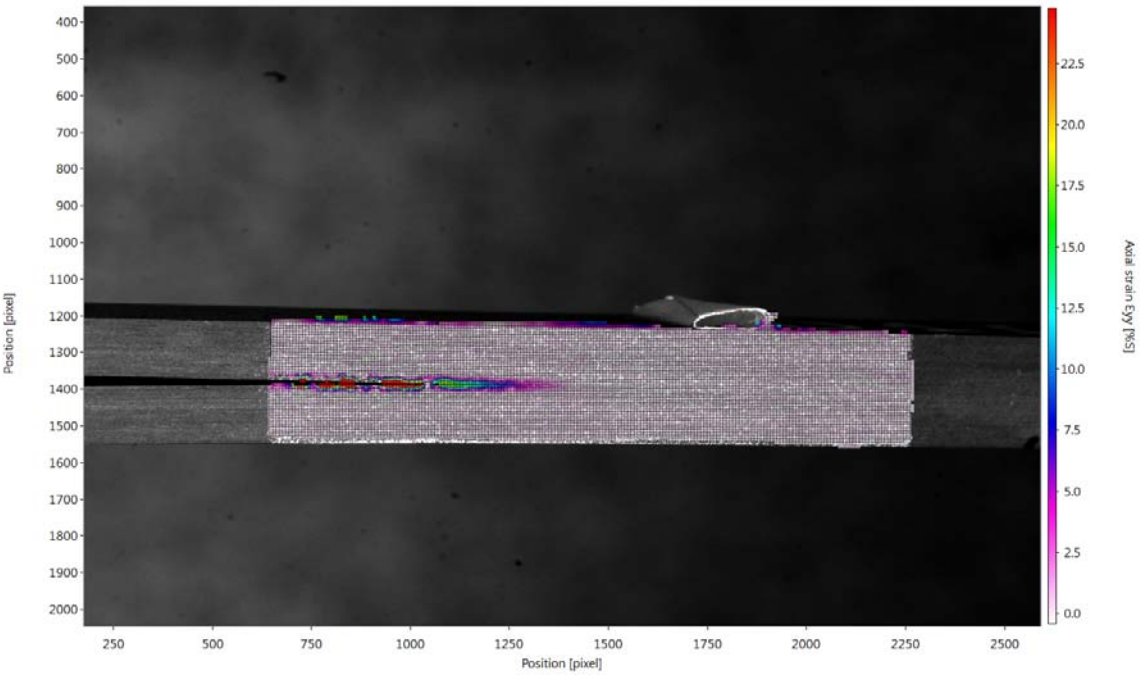

Figure 5.6: DCB, vertical strain ϵ_{yy}.

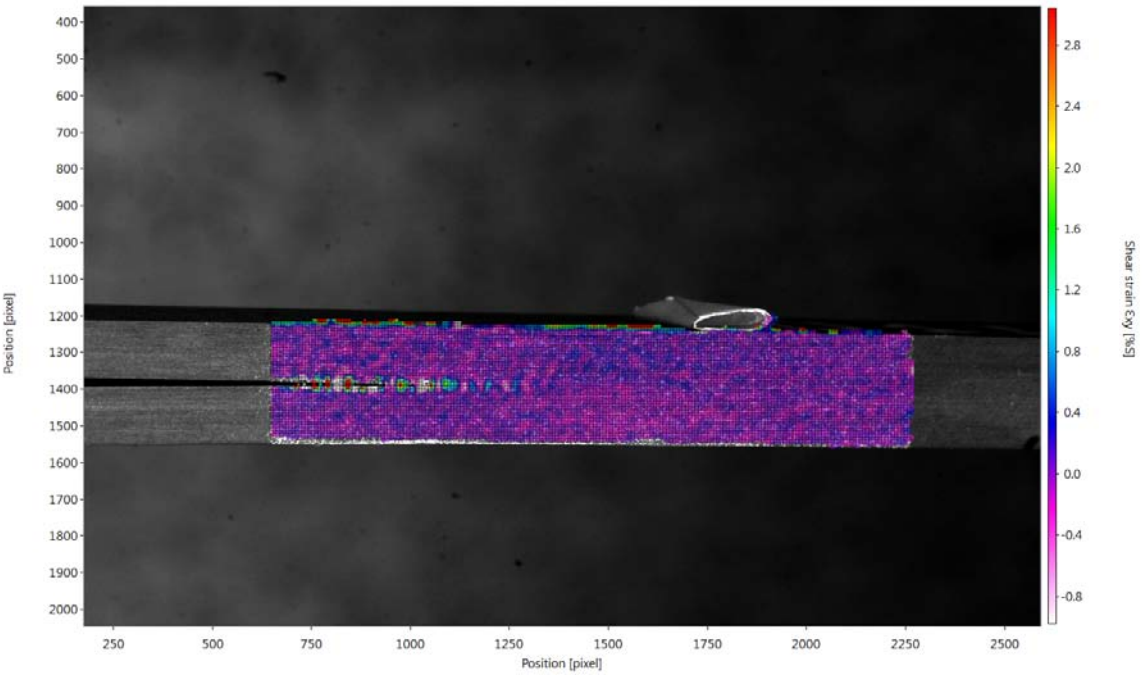

Figure 5.7: DCB, shear strain ϵ_{xy}.

Specimen	G_{IC} $[J/m^2]$	*ST.DEV* $[J/m^2]$
1	240	19
2	239	5
3	259	5
4	214	6

Table 5.1: Fracture toughness (G_{IC}) and corresponding standard deviations (*ST.DEV*) for the DCB samples.

- The increment in crack length in mm over time is then worked out thanks to an EXCEL data-sheet;
- The increment in crack length vs time is then converted into increment of crack length vs crosshead displacement thanks to an MACRO (the speed of the test is known and is 2 mm/min);
- These data, together with the data load vs crosshead displacement from the load cell, are then feed into another EXCEL macro that calculates the G_{IC} and the R-curves thanks basically to the equations reported in §2.7.1. However, this macro, that was created by the Imperial College London, is password protected and so the exact nature or the interpolation of the force and the displacement for each crack length is not known.

In Table 5.1 are reported, for each of the four DCB samples, the values of the fracture toughness calculated using the CBT together with the corresponding standard deviations. In Figure 5.8 are depicted the R-curves. Both the values of the G_{IC} and the R-curves are very close to those obtained by Mark Conroy (on average 218 J/m^2, [12]) and Marijana Larma (on average 237 J/m^2, [30]) that used the same material.

5.2 Investigating the Strain Calculation

As it was stated in §4.4.1 the results of the DIC calculation is a displacement field from which a deformation gradient F is computed [31]. This deformation gradient describes both the shape change of a deformed object and the rigid body rotation. The rotation doesn't alter the object and therefore doesn't induce any strain. By applying the polar decomposition[1] the deformation gradient tensor F is decomposed into a rotation tensor R and a (right) stretch tensor U that describes the shape change (Figure 5.9)

$$F = RU. \tag{5.1}$$

[1]For the polar decomposition refer to [24], section 4.2

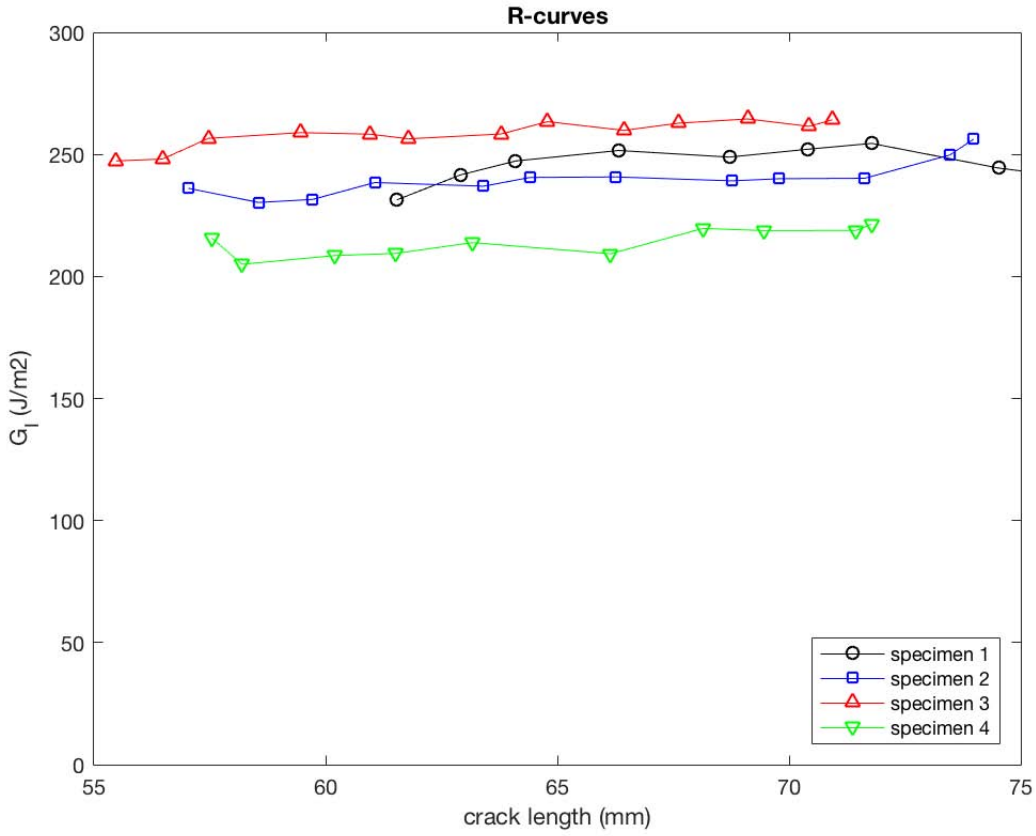

Figure 5.8: *R*-curves of the four DCB specimens.

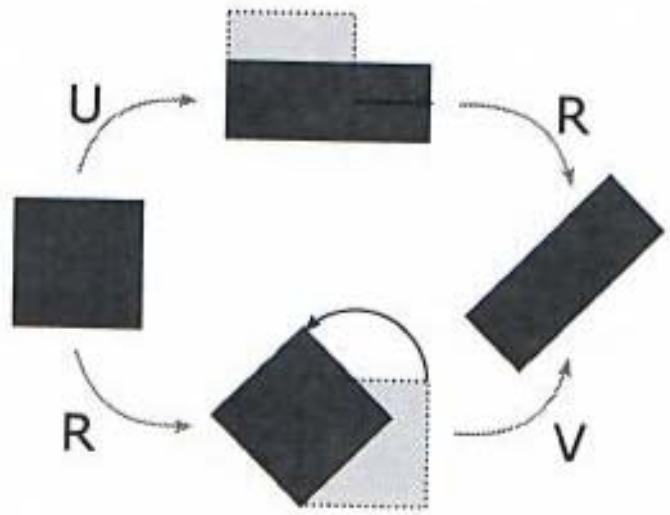

Figure 5.9: Polar decomposition of the deformation gradient tensor (from [31])

The components of the engineering strain tensor are then calculated using small strain approximation which means that only the first order terms are considered

$$\epsilon_{xx} = \frac{\partial u_x}{\partial x} \approx U_{11} - 1 \tag{5.2a}$$

$$\epsilon_{yy} = \frac{\partial u_y}{\partial y} \approx U_{22} - 1 \tag{5.2b}$$

$$\epsilon_{xy} = \frac{1}{2}\left(\frac{\partial u_x}{\partial x} + \frac{\partial u_y}{\partial y}\right) \approx U_{12}. \tag{5.2c}$$

This way of calculating the strain is, as we expected, correct and even the approximation of small strains is consistent since during the test the composite behaviour is elastic. It can be concluded that the way in which the strains are calculated is not the reason why the results are not good.

5.3 Assessing the Accuracy of the DIC

In order to assess the accuracy of the DIC under this experimental configuration a three point bending test was performed. During this kind of test the specimen is moving only a few and in any case, far less than during a normal DCB test. Moreover, the loads are much higher and therefore also the strains that develop in the material are higher.
Four rectangular samples were cut starting from DCB samples so that they have a width of 25 mm, a length of 90 mm and a thickness of 5 mm. The surface of the sample that was going to be observed with the DIC was polished and painted. Regarding the test method, the samples were placed on two supports that were 80 mm far from each other. The load was applied in the middle of the sample thanks to a pin that was moving downwards with a speed of 2 mm/min and

Figure 5.10: Experimental configuration for the three point bending test.

recorded using a 50 kN load cell (Figure 5.10). The DIC was then placed in front of the sample maintaining the same experimental configuration that had been used for testing DCB (i.e. distances, lights etc. . .). Also the calculations were carried out using the same parameters as the DCB.
Regarding the results, again the displacements u_x and u_y look very smooth and consistent. The main concern is, even in this case, the axial strain ϵ_{xx} for which we expect a Navier distribution across the thickness. In Figure 5.11 is depicted the axial strain ϵ_{xx} for a load of 3000 N. This is the minimum load for which we can start to see a linear distribution for the strain. However, as it can bee seen, the distribution is not so clear: the maximum and minimum strains at the edges of the sample are not exactly equal and opposite and the neutral axis is a very curved line. This fact, together with the observation that the Navier distribution gets better as the load is increased, brought us to conclude that the DIC under this experimental configuration was not accurate enough to pick up the strains when they are small like in a DCB test (where the maximum load is lower than 200 N).

5.4 Increasing the Accuracy of the DIC

Many are the factors that may affect the accuracy or the DIC

- painting;
- distance between the cameras and the sample;
- contrast achieved in the images;

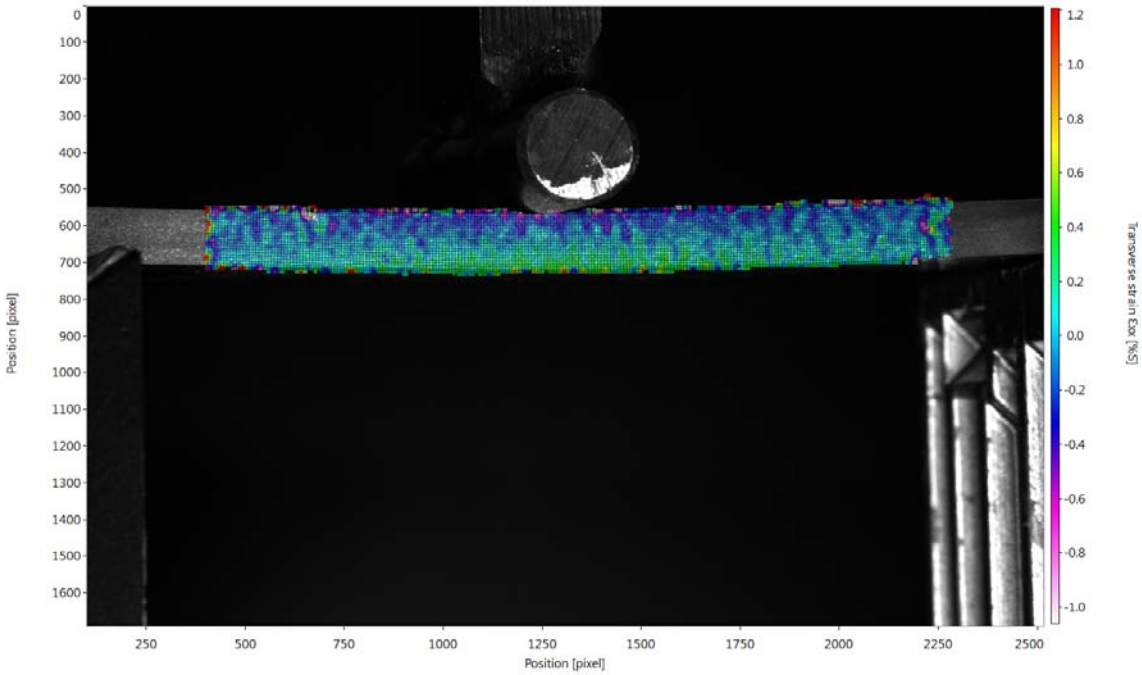

Figure 5.11: Three point bending, axial strain ϵ_{xx}.

- calibration plate used.

In order to increase the accuracy it is necessary to paint the samples in the best way possible. This means that the white dots should be very small and uniformly distributed. In order to achieve this, we moved from painting the sample outside and spraying the paint vertically on them to painting the samples inside (no wind) and spraying the paint horizontally (§4.4.3). Regarding the contrast, after many months of practicing and a training session with a technician from LaVision that took place in the middle of May, we were able to reach very high values (up to 900 counts using the 10 bit cameras). The distance rail-sample of 750 mm was chosen because it was the minimum to be able to capture the whole area of the 58x58 mm calibration plate that was the smallest available. In order to be able to stay closer to the sample during the test a smaller calibration plate (20x20 mm) was purchased from LaVision. Unluckily, because of an error, the company sent a 25x25 mm calibration plate and, only later, the required 20x20 mm. However, the 25x25 mm calibration plate (025-3.3) allowed to reduce the distance between the sample and the rail up to 300 mm. Other four three point bending samples were tested under this conditions and the results (i.e. the axial strain at about 3000 N) is depicted in Figure 5.12. As first thing it is important to notice that, since the cameras are closer to the sample, the area that can be observed is smaller than in Figure 5.11. More, we can observe that the maximum and minimum axial strains (i.e. $\epsilon_{xx,MAX}$ and $\epsilon_{xx,MIN}$) are about the same but, in this second case, the distribution is smoother.
It can be therefore concluded that the reduction of the observation distance together with the usage of a smaller calibration plate brought some improvements.

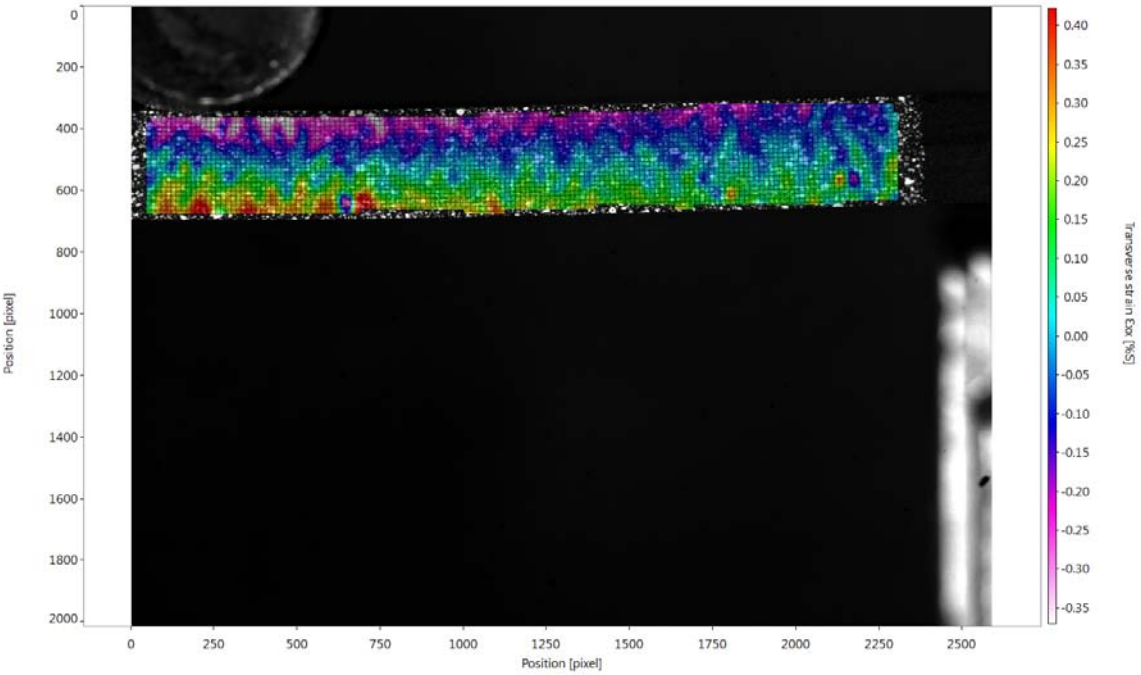

Figure 5.12: Three point bending, axial strain ϵ_{xx}.

This experimental setup (with some small changes) was then used to perform another DCB test and also one FRMM and one ELS whose results are described in the following paragraphs.

5.5 Last DCB tests

The last DCB test was performed using the 20x20 mm calibration plate (020-5 SSDP) that arrived in the last weeks of the experiments. The usage of this smaller calibration plate allowed to further reduce the distance between the rail and the DIC up to 250 mm. To achieve about the maximum possible contrast with the 10 bit cameras (1000 counts) the lights were placed as shown in Figure 5.13 and the following parameters were used: aperture 11 and exposure time between 60 and 70 ms. Since the cameras and the the sample were very close to each other, the area that could be observed was only 20 mm in length. With reference to Figure 5.1, the areas that were observed (and thus painted) and their distances from the beginning of the sample are:

- for the test form the insert: $L_1 = 45mm$, $L_2 = 65mm$, $a_0 = 60mm$;
- for the first test from the precrack: $L_1 = 55mm$, $L_2 = 75mm$, $a_0 = 65mm$;
- for the second test from the precrack: $L_1 = 80mm$, $L_2 = 100mm$, $a_0 = 75mm$.

Regarding the parameters for the calculation, the same stated in §5.1.2 were used. Only the subset size was changed from being 25 pixels to 65 pixels. (Many

calculations have been performed using different subset sizes and the 65 pixels proved to be the best, given this sample-cameras distance). The results (i.e. the strain field) for the test from the first precrack during stable crack propagation are shown in Figures 5.14 (ϵ_{xx}), 5.15 (ϵ_{yy}) and 5.17 (ϵ_{xy}). As we can see, the axial strain exhibit a clear linear distribution across the beams thickness. More, the neutral axis is almost in the middle of each of the beams although it is not a perfect straight line. Regarding the transverse strain, using this experimental configuration the DIC is able to capture the traction strain that develops above the crack tip (red zone) and also the the compression zone after the traction zone (Figure 5.16). Looking then at Figure 5.17 we can see that the shear strain is almost zero in correspondence of the crack plane, as it was expected. Since we are applying loads and not pure moments, we would have expected to see parabolic distributions of the shear strain across each of the two beams, while looking at Figure 5.17 we cannot see this. The reason, however, is simply because these strains are much smaller than those that develop above the crack tip. If we reduce the scale of the colours (Figure 5.18) we can appreciate even these parabolic distributions.
On one hand these results are very satisfactory: a huge improvement has been achieved since the beginning of the experimental campaign. Moreover, it is important to remember that the accuracy of the DIC has been brought up to its limit since we are detecting maximum axial strains that in the order of 0.07 %, value that is only three/four times higher than the error stated in [29] for this subset size.
On the other hand, these results are not good enough to be fed into the MATLAB script for the calculation of the total G and the mode partition for several reason.

- First is a technical aspect that could be easily overcome. The software StrainMaster allows to export only the displacement field and not the strain field. To export the strain field it is necessary to use the software DaVis which turned out to be available only in the last weeks of the test. Since this software is much more complicated than StrainMaster, there was not enough time to understand how to use it.

- The distributions of the strains seem, from the pictures, to be good. However, if one looks at the local values of the axial strain (i.e. he calculates them from the displacements since the StrainMaster doesn't allow to export them) of a selected transverse section, he can see that they are not so smooth. For example the Navier distribution, which is supposed to be linear, is not perfectly linear ($R^2 = 0.95$ in the best case). Moreover, the neutral axis is not exactly in the middle of the section and the maximum and minimum values are not exactly equal and opposite. It is necessary to average several sections that are close to each other to obtain a good linear distribution ($R^2 = 0.98$) that has the zero strain exactly in the middle. This problem is of course related to the fact that the strains that are captured are only (in the best case) four times higher than the error of the machine.

- The calculation masks (areas) were positioned so that to avoid both the

Figure 5.13: Experimental setup used in the last tests.

edges of the sample and the crack faces. The reason is simple: if the areas were placed so that to include the previously mentioned surfaces, there would be a lot of noise and the calculated displacement field would be completely wrong (at least at the boundaries). However, the displacements and strains data close to the crack surfaces, which are in this way not available, are necessary for the calculation of the J-Integral. In order to be able to have these missing information a fitting of the available data should be performed followed by extrapolation. This is a very hard task and requires a lot of time on its own.

5.6 FRMM Test

The FRMM test was performed in the same way as the last DCB and also the same calculation parameters were used. The only difference concerned the painted areas. With reference to Figure 5.1, the areas that were observed (and thus painted) and their distances from the beginning of the sample are:

- for the test form the insert: $L_1 = 65mm$, $L_2 = 85mm$, $a_0 = 80mm$;
- for the first test from the precrack: $L_1 = 75mm$, $L_2 = 95mm$, $a_0 = 85mm$;
- for the second test from the precrack: $L_1 = 100mm$, $L_2 = 120mm$, $a_0 = 95mm$.

It is important to point out that, since the test from the insert might result in unstable crack initiation, the sample was clamped 5 mm after the crack tip. The results (i.e. the axial and transverse strains) for the test from the first precrack

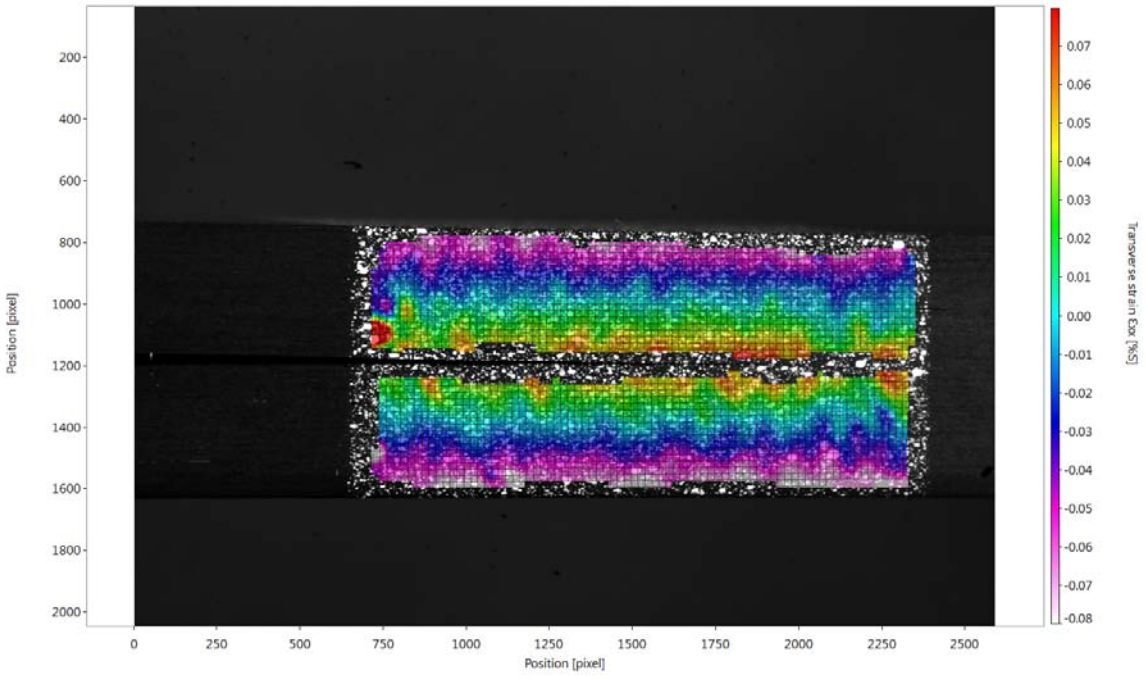

Figure 5.14: DCB, axial strain ϵ_{xx}.

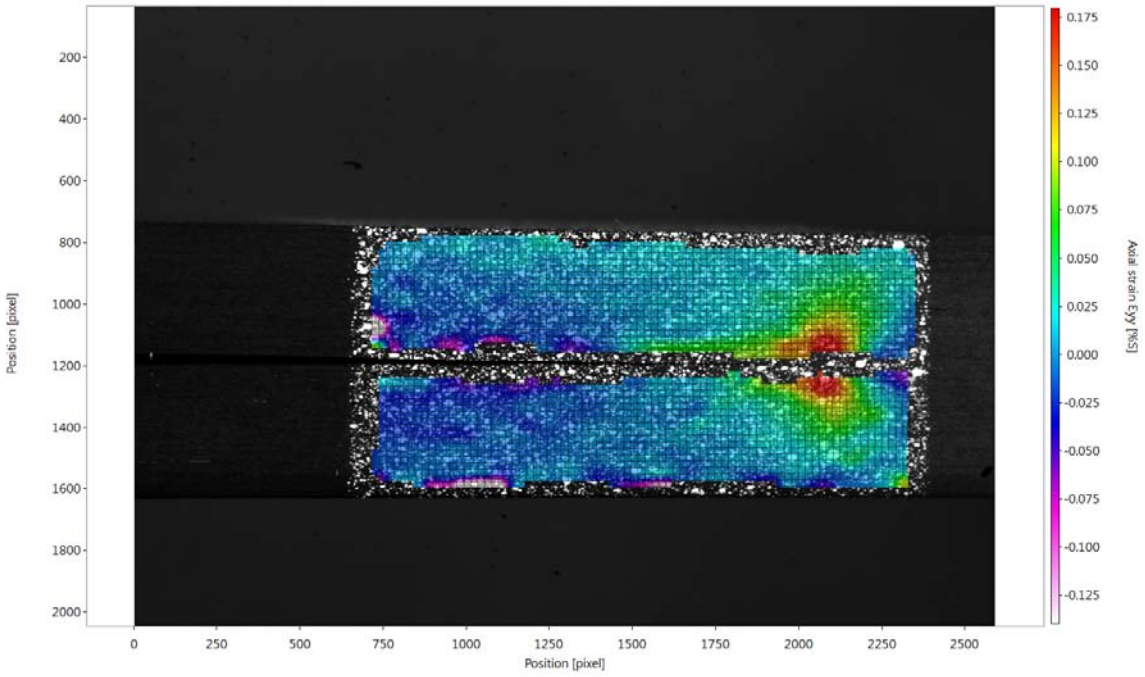

Figure 5.15: DCB, vertical strain ϵ_{yy}.

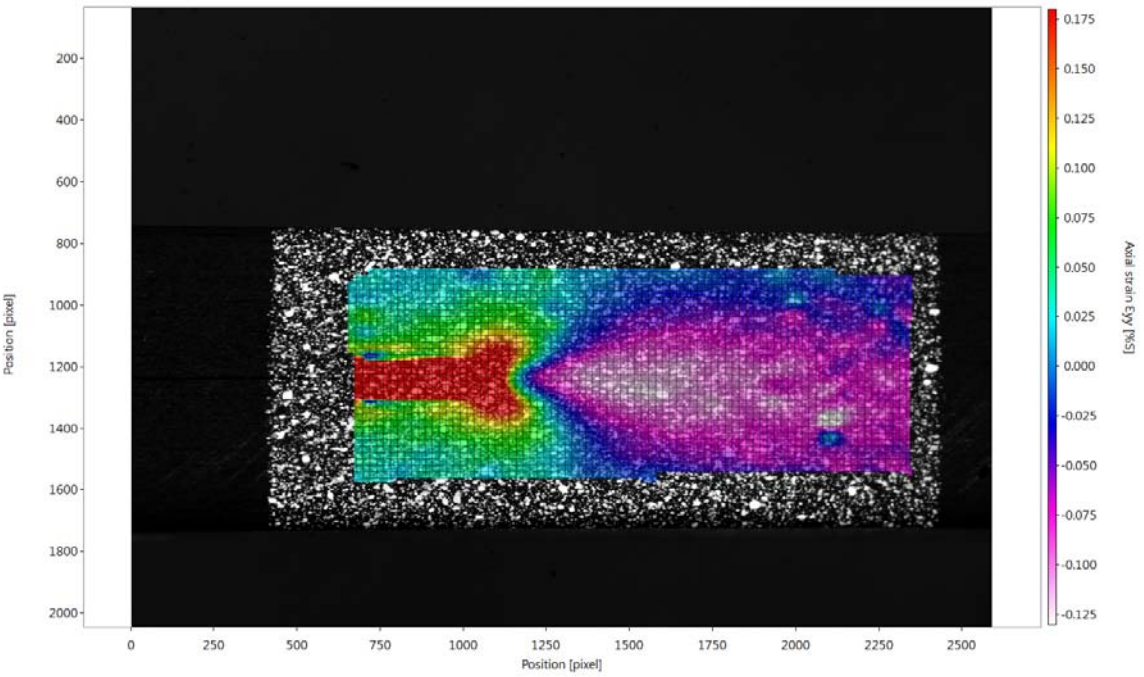

Figure 5.16: DCB, vertical strain ϵ_{yy}, detail.

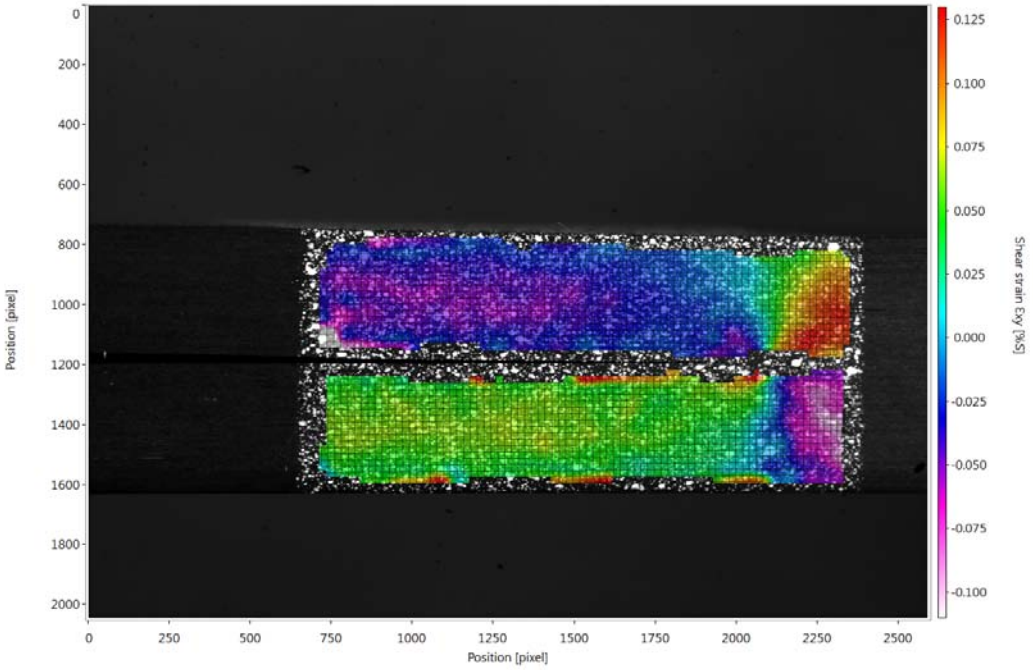

Figure 5.17: DCB, shear strain ϵ_{xy}.

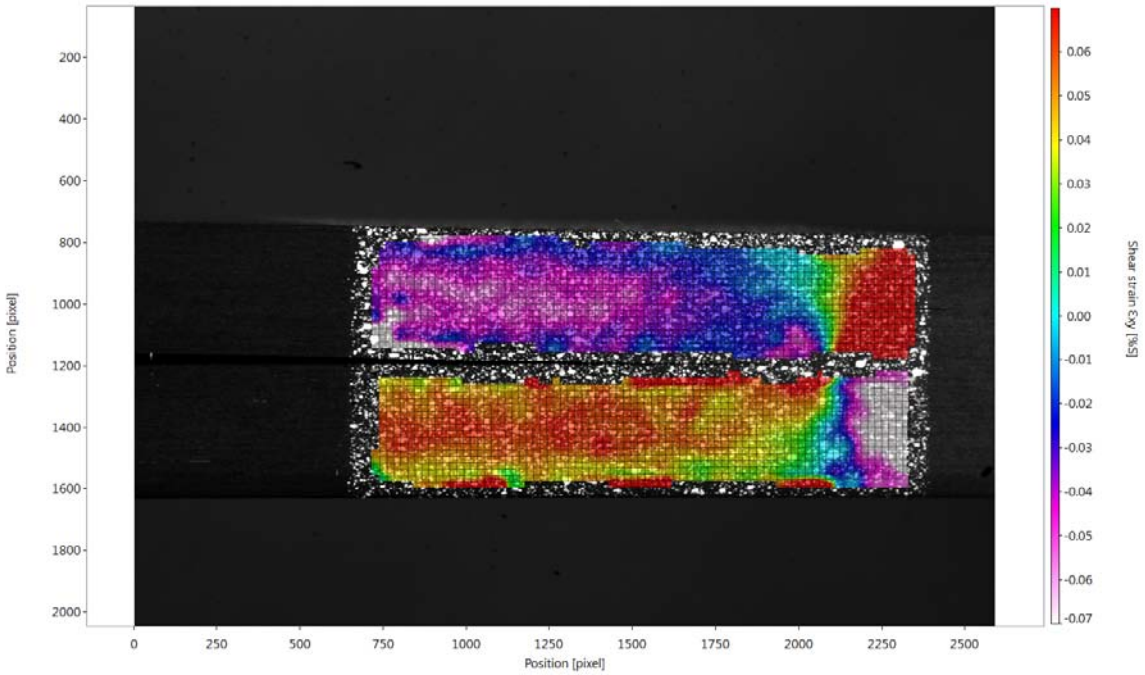

Figure 5.18: DCB, shear strain ϵ_{xy}.

during stable crack propagation are shown in Figures 5.19 (ϵ_{xx}) and 5.20 (ϵ_{yy}). It is interesting to notice that the lower beam experience an axial strain that approaches zero as we go far from the crack tip. This is correct since in this kind of test the lower beam is not loaded. Regarding the transverse strain we can observe that the distribution in correspondence of the crack tip is not symmetric. In particular we can see that the traction strains are more concentrated in the lower beam while the compression ones in the top beam. Basically what is happening is that the strains, and thus the stresses, are transferred from the top beam (that is loaded) to the bottom beam (which is unloaded). The same problems explained in §5.5 affect also the FRMM.

5.7 ELS Test

The ELS test was performed in the same way as the last DCB and FRMM and also the same calculation parameters were used. With reference to Figure 5.1, the areas that were painted are:

- for the test form the insert: $L_1 = 65mm$, $L_2 = 85mm$, $a_0 = 80mm$;
- for the first test from the precrack: $L_1 = 75mm$, $L_2 = 95mm$, $a_0 = 85mm$.

Also in this case, for the test from the insert, the ample was clamped 5 mm after the crack tip. However, in this case, also the propagation of the real/physical crack was unstable, and the crack initiation brought to the breaking of the whole sample during the test from the precrack. The results (i.e. the axial and shear

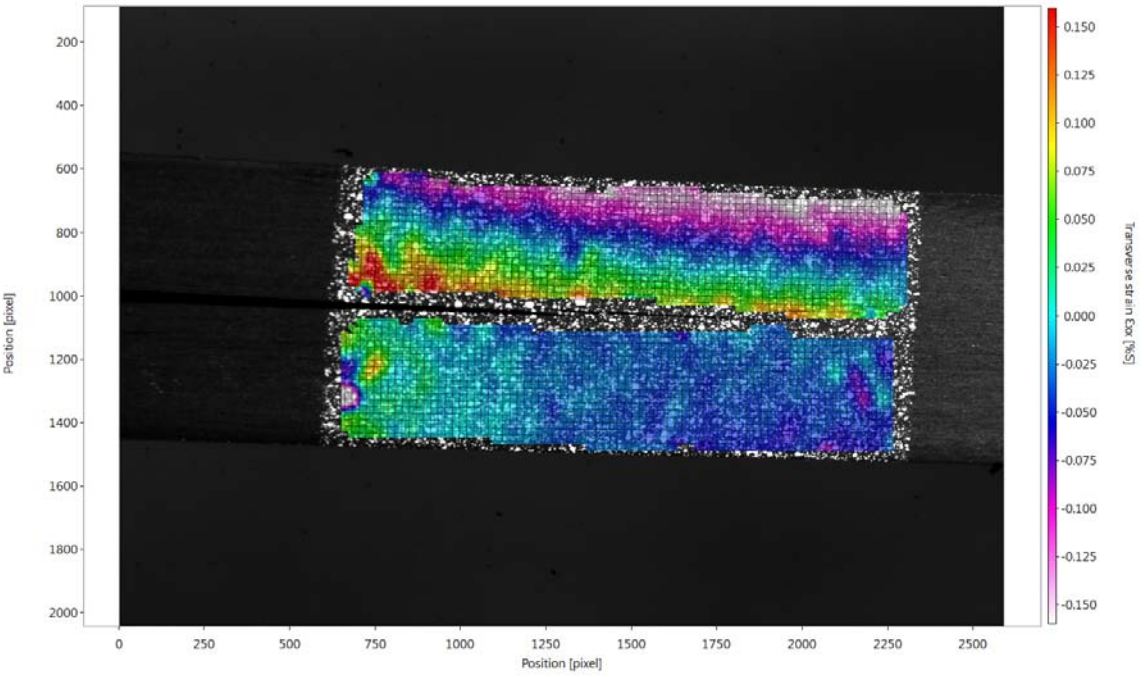

Figure 5.19: FRMM, axial strain ϵ_{xx}.

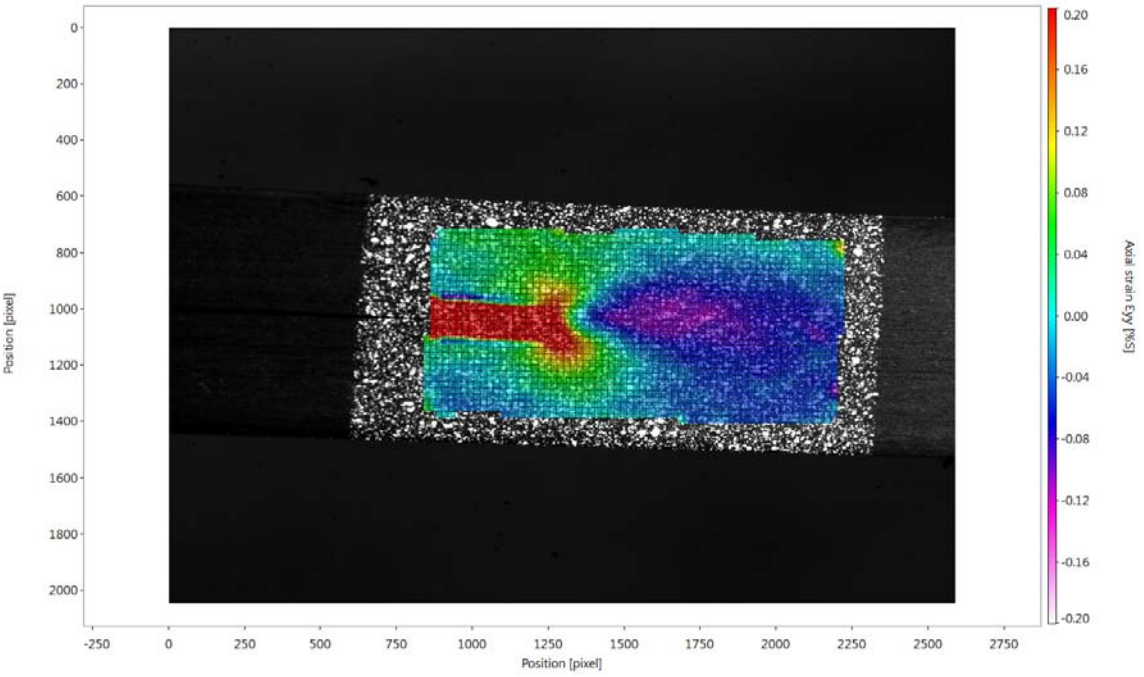

Figure 5.20: FRMM, vertical strain ϵ_{yy}, detail.

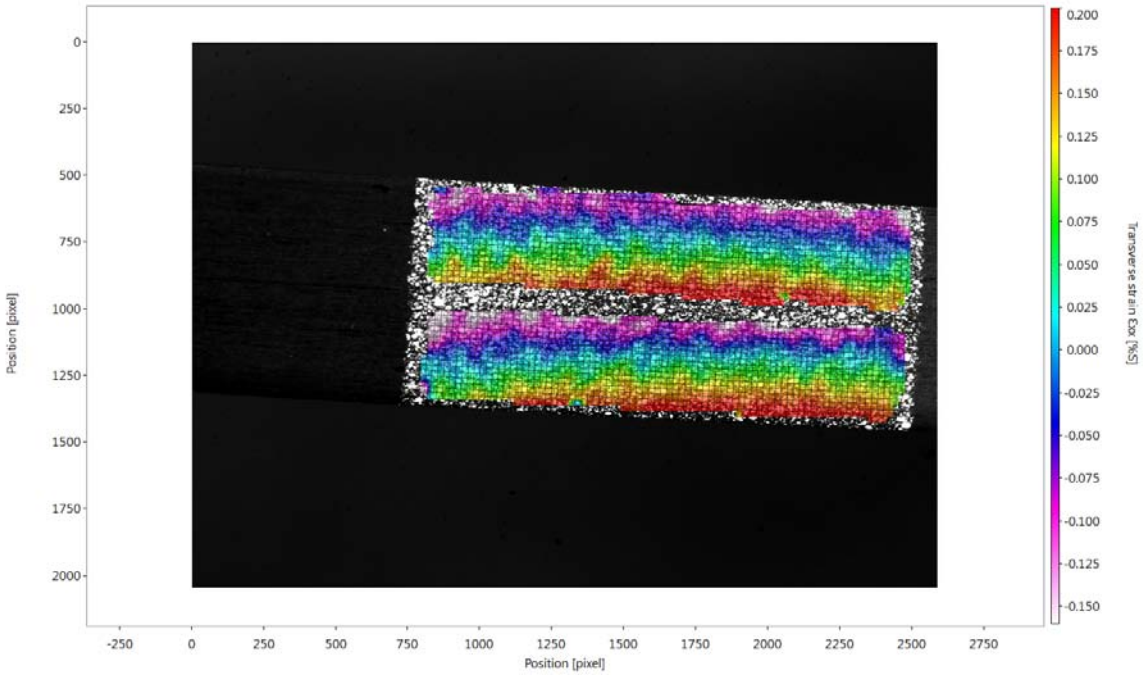

Figure 5.21: ELS, axial strain ϵ_{xx}.

strains) for the test from the precrack immediately before the crack initiation are shown in Figures 5.21 (ϵ_{xx}) and 5.22 (ϵ_{xy}). Looking at the axial strain we can notice that the values are very high, especially in comparison with those of DCB. This is not surprising since also the loads (moments that are necessary to initiate the crack) are much higher during the ELS test. Regarding then the shear strains, we can see that the maximum values are in the zone that is above the crack tip. This of course makes sense since the ELS test is a pure mode II and the sample fails because of the shear stress that develops above the crack. The same problems explained in §5.5 affect also the ELS.

5.8 Chapter Conclusions

The conclusions of this chapter are reported in detail in the next next one, together with those from the other chapters.

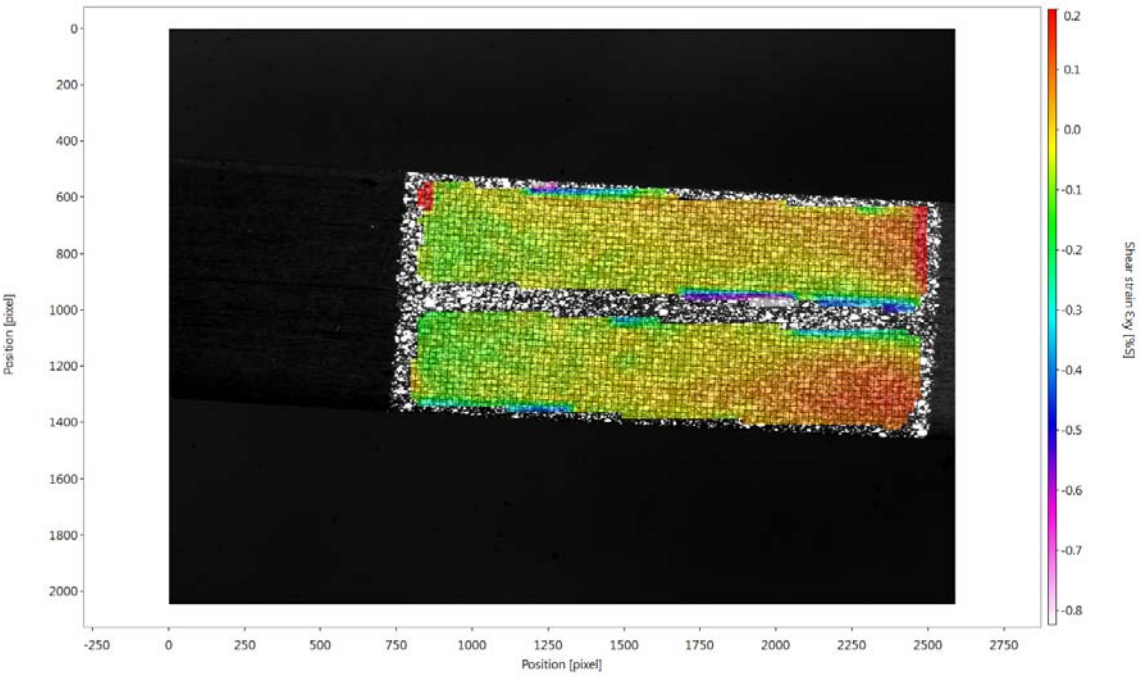

Figure 5.22: ELS, shear strain ϵ_{xy}.

Chapter 6

Conclusions and Future Work

The first Chapter of this report gives an overview on composite materials. In particular the advantages, the disadvantages and the applications of CFRP were described.
The second Chapter outlines the theory that is at the basis of mixed-mode fracture mechanics. The first theory that was explained is the one from Williams for the determination of the total ERR. Then both the mode partitioning theories from Williams (global) and Hutckinson and Suo (local) were briefly described. After this, the J-Integral approach for the calculation of both the total and the mode decomposed ERR (Ishikawa) were reported. Finally the principles at the basis of standardized fracture tests (DCB, ELS and FRMM) were presented together with the CBT equations for the calculation of the ERR.
The third Chapter regards the computational and the modelling part of this work. In particular the equations that were implemented in the MATLAB script for the calculation of both the total and mode decomposed ERR were derived. Then the characteristics of the "static" (singular, no damage or crack propagation) ABAQUS model were described. The MATLAB script, fed with the fields' values from the ABAQUS model, gave results that are in agreement with the analytical equations for the total G and the mode decomposition in the symmetric cases. Regarding the asymmetric cases, the numerically calculated total G was correct and also the mode decomposition was in agreement with what predicted by Hutckinson and Suo. However, in this last case, the error was slightly higher (even tough still acceptable) for two reasons:

- in asymmetric cases the integration needs to be performed inside the specimen (at least for one of the two horizontal paths);
- the theory from Hutckinson and Suo itself is affected by a certain error due to some approximations that are carried out to derive it.

After this, damage was introduced at the crack tip by creating another ABAQUS model using cohesive elements. The theory behind the cohesive zones was then explained and the results obtained from the MATLAB script in this case were provided. As it was expected, the introduction of damage didn't alter substantially the value of the total G but the mode partitioned ERR of the asymmetric cases

shifted from the values predicted by Hutckinson and Suo towards those predicted by Williams.
The fourth Chapter describes the sample manufacturing and preparation and the main equipments used. The standard test methods are also explained in a dedicated paragraph. The last part of this chapter deals with the DIC, the hearth of this work. The principle that is at the basis of the software installed on this machine, the hardware components, the samples preparation for the DIC and the specific test method procedure that has to be adopted are carefully described.
In the fifth Chapter are reported all the most important experiments that have been performed together with a detailed description of the experimental configuration and the parameters used for bot the recording and the fields calculation. The first four DCB test gave results that were completely weird. The hypothesis that were made for explaining the reason of such bad results were many: movement of the sample during the test, loads applied instead of moments, way in which the strains are calculated by the software and accuracy of the DIC. The first two problems couldn't be investigated since doing it would have required to use a completely different machine like the one used by Mark Conroy [12]. Regarding the strain calculation this proofed to be correct. After an investigation (three point bending test) the main problem resulted to be the accuracy of the DIC which, for this first experimental configuration, was not high enough and, therefore, only the noise was picked up. In order to increase the accuracy different strategy have been implemented:

- use of a small (20x20 mm) calibration plate;
- decrease the distance between the cameras and the sample;
- increase the quality of the painted pattern (smaller and better distributed dots)
- obtain an higher contrast (by playing with the position of the lights, the aperture of the cameras and the exposure time).

After many trials an optimal experimental configuration was found that was used to perform the last DCB, ELS and FRMM tests. The results obtained in these last tests were good: both the displacement and the strain filed were in very good agreement with what we expected from the theory and the simulations. Despite this new problems arose that prevented to feed the field data from DIC into the MATLAB script for the calculation of the ERR (total and partitioned). In particular:

- the strains that were picked up were (in the best case, so for the axial strain) only four/five times higher than the error of the machine (declared by the company). Such an high error would explode during the calculation of the ERR.
- the displacement and strain data are missing in the zones close to the crack and the external surfaces of the sample. This because the calculation mask

was set to be smaller than the thickness of the sample in order to prevent the noise to appear at the boundaries (the software is unable to see that there is a crack propagating and is considering the material continuous).

It is clear that these problems cannot be easily overcome and the search for a solution might requires a lot of time. In the following lines are reported some ideas that can be implemented.
Regarding the first problem there are two ways to overcome it. The first thing that can be tried is to increase the strains. For example it can be considered to change material: instead of using a unidirectional CFRP (high E) use another material for which, for the same load, geometry etc... the strains that develops are higher (lower E). The other possibility is to increase more the accuracy of the DIC. The 20x20 mm calibration plate is the smallest that is available and going closer to the sample with the cameras is not possible because a part of the surface of the calibration plate would be missed and the residual fit error would increase. Of course there is the possibility to manufacture a smaller calibration plate but this should be very accurate with very small tolerances (difficult). The contras that was achieved in the last experiments was about the maximum for the 10 bit cameras. Therefore, unless new cameras (12 or 14 bits) are purchased, improvements in this field cannot be done. Regarding the paint it is important to notice that the "spraying" technique that has been used is not the best and the most repeatable one: the quality of the result strongly depends on the experience and the pattern is different between the samples. Regarding this aspect, it should be noted that a very simple and cheap technique to create a pattern has been developed by Paolo Mazzoleni [32]. This technique involves the following steps: the speckle pattern is numerically designed on a calculator, the drawing is printed using a common laser printer, the pattern is transferred from the paper to the specimen by mean of a thermo-mechanical process.
Another thing that can be done to reduce the noise and increase the accuracy of the DIC is to average in time adjacent images and then use for the processing only the averaged images [33]. However, the implementation of this thing should be done by the company LaVision since it requires to modify the software StrainMaster.
Regarding the second problem the idea is to export only the punctual displacement values from the DIC and then develop a code that interpolates a field through those data. In this way the local values of the strains can be obtained by simple derivation of the field and the displacements and strains data in the regions close to the crack and the surfaces of the sample can be obtained via extrapolation.

Appendix A

Chapter 3 Models: ABAQUS Results

In this appendix are reported the images which show the results of the ABAQUS models (Chapter 3). In particular, each of the following sections focuses on a particular model: DCB, ELS, FRMM, AFRMM (singular) and AFRMM (damage). Since FRMM is a particular case of the more general AFRMM (singular), they will be treated in the same section exposing only the symmetric case. Moreover, regarding the AFRMM (damage) models, the results of the one with $h_1 = 3mm$ and $h_2 = 7mm$ will be shown.
All the results shown regard models with a mesh size of 0.2 mm (i.e. 25 elements across half beam thickness). To make the deformation more evident a scaling factor of 20 has been chosen.

A.1 DCB

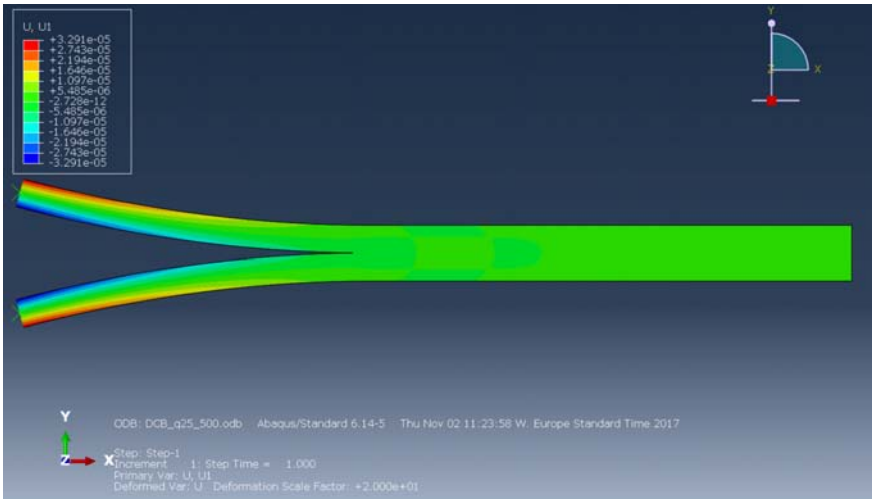

(*a*)

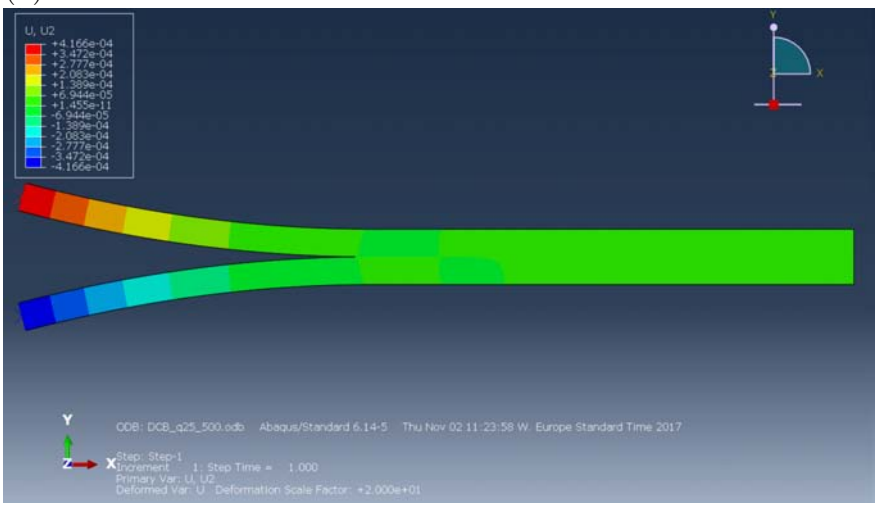

(*b*)

Figure A.1: DCB, displacements in the x (horizontal) direction u_x (a) and in the y (vertical) direction u_y (b).

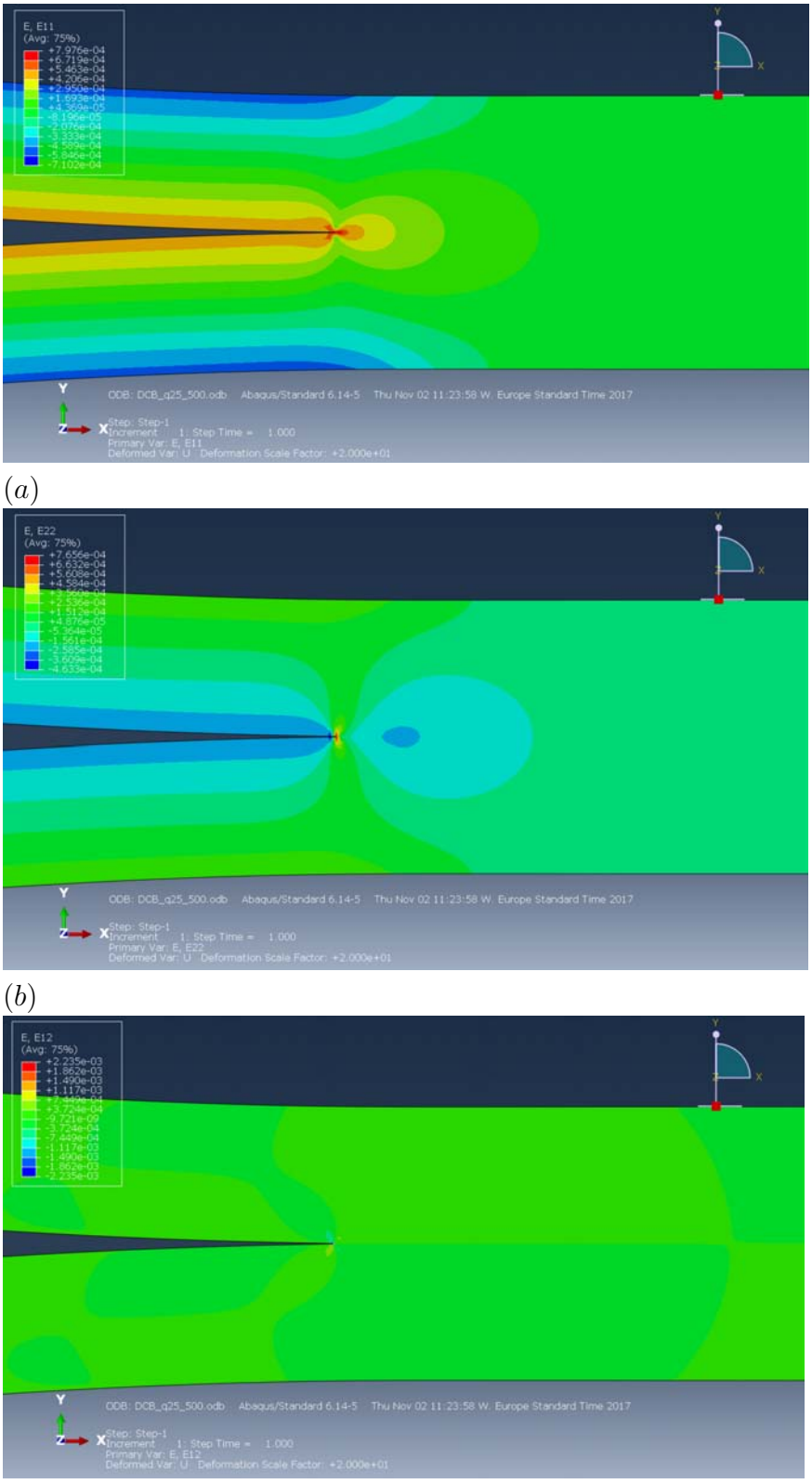

Figure A.2: DCB, axial (a), vertical (b) and shear (c) strains, respectively ϵ_{xx}, ϵ_{yy} and ϵ_{xy}.

A.2 ELS

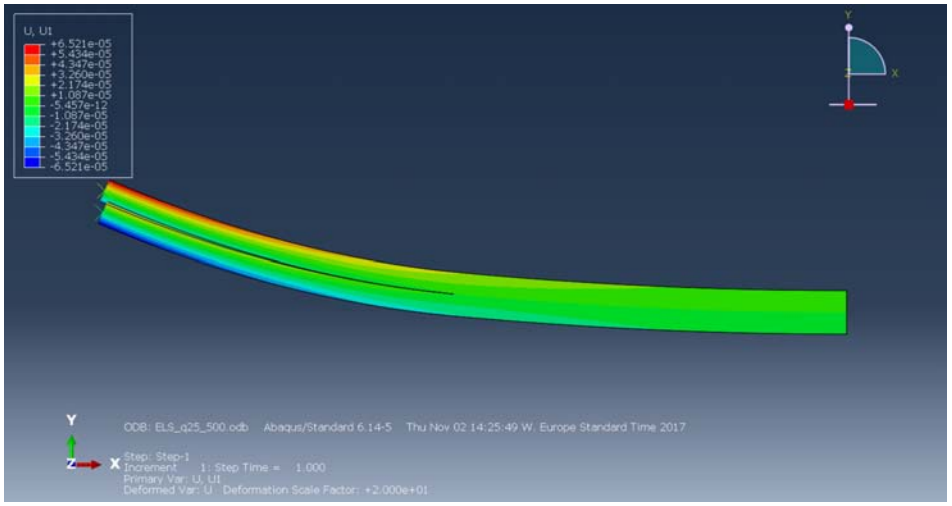

(*a*)

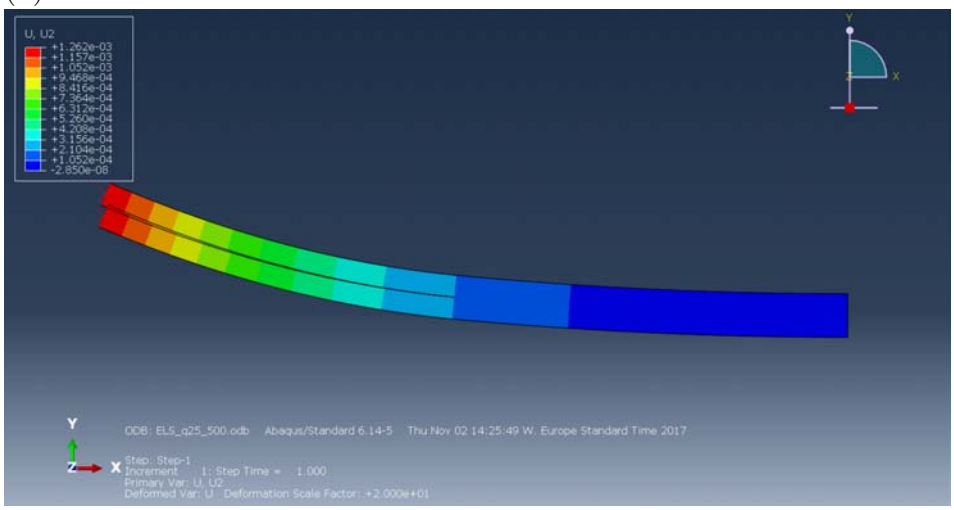

(*b*)

Figure A.3: ELS, displacements in the x (horizontal) direction u_x (a) and in the y (vertical) direction u_y (b).

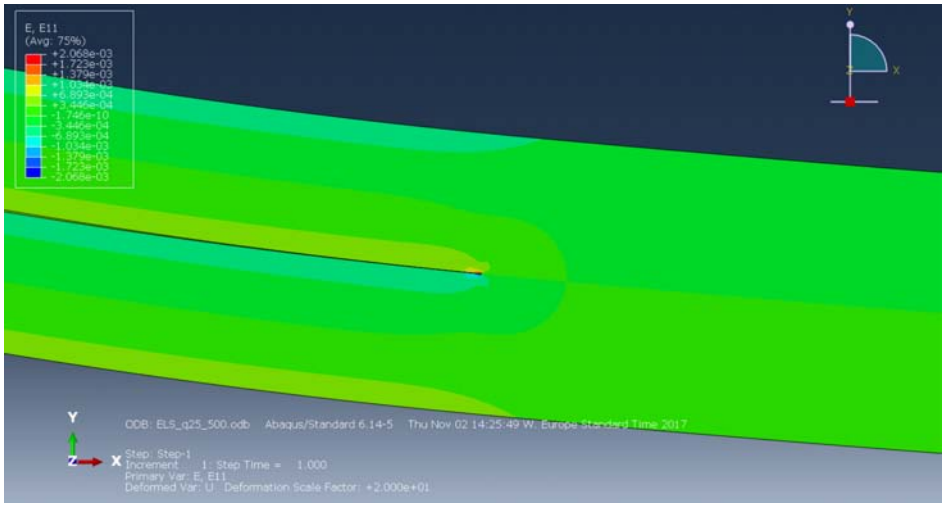

(*a*)

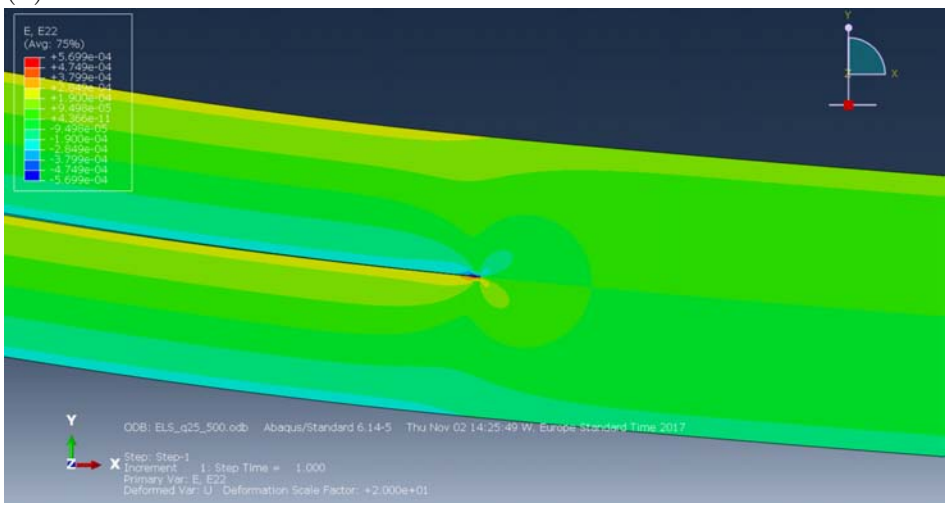

(*b*)

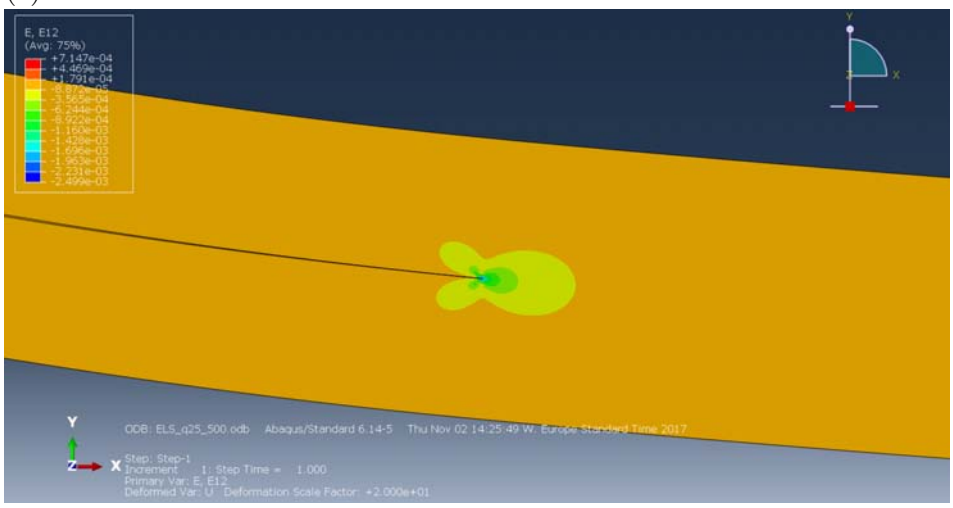

(*c*)

Figure A.4: ELS, axial (*a*), vertical (*b*) and shear (*c*) strains, respectively ϵ_{xx}, ϵ_{yy} and ϵ_{xy}.

A.3 FRMM (also as special case of AFRMM singular)

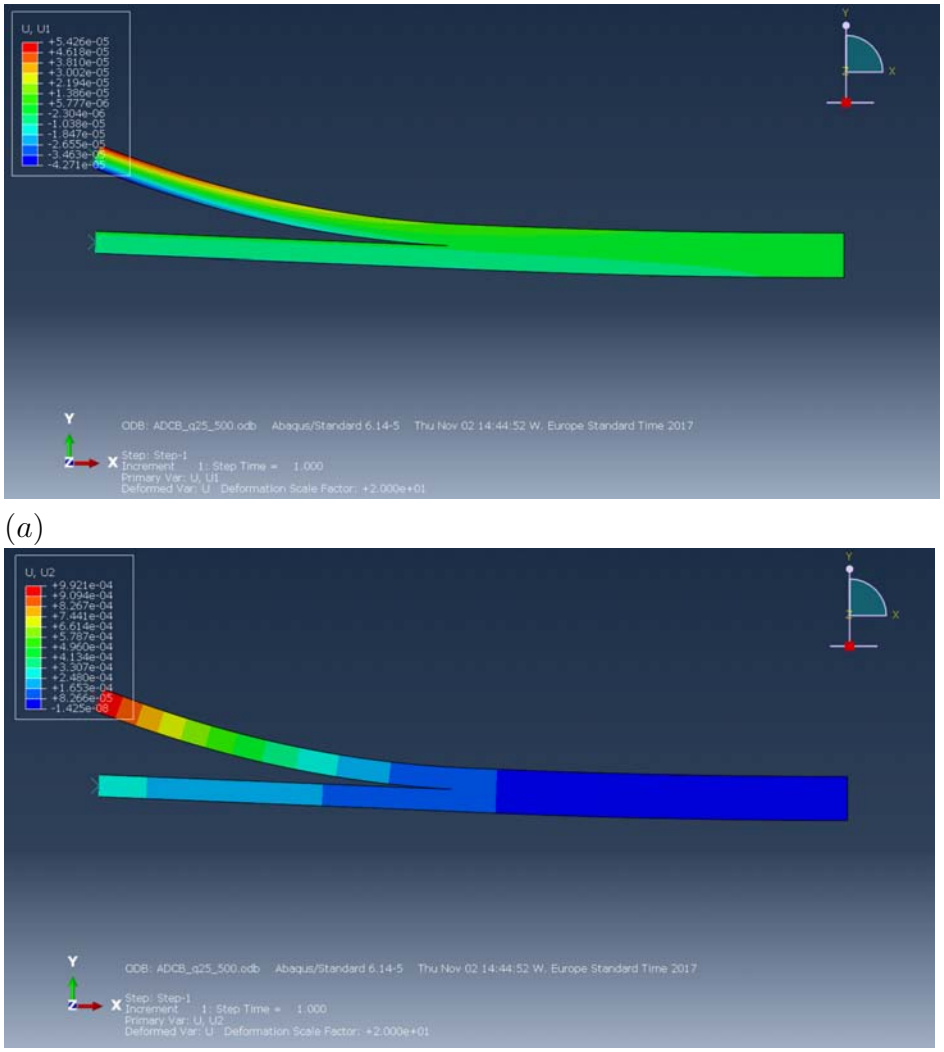

Figure A.5: FRMM, displacements in the x (horizontal) direction u_x (a) and in the y (vertical) direction u_y (b).

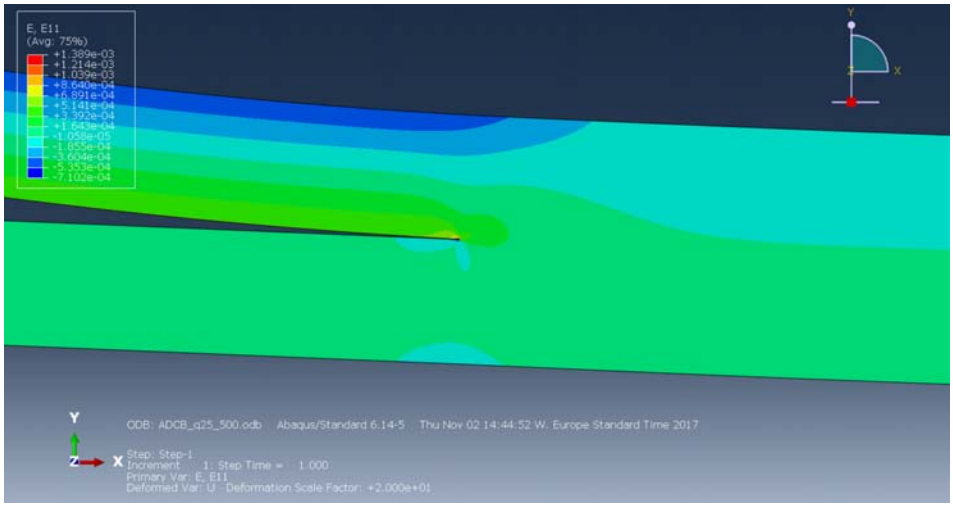

(*a*)

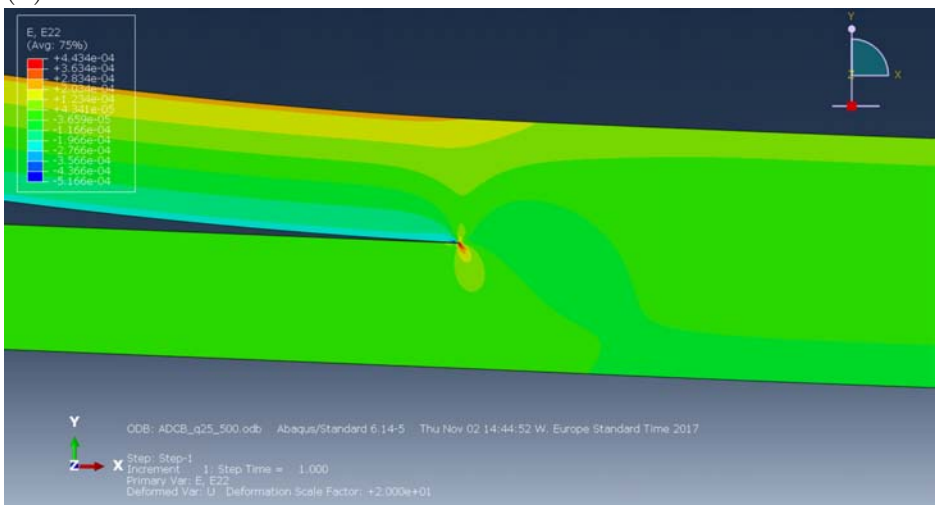

(*b*)

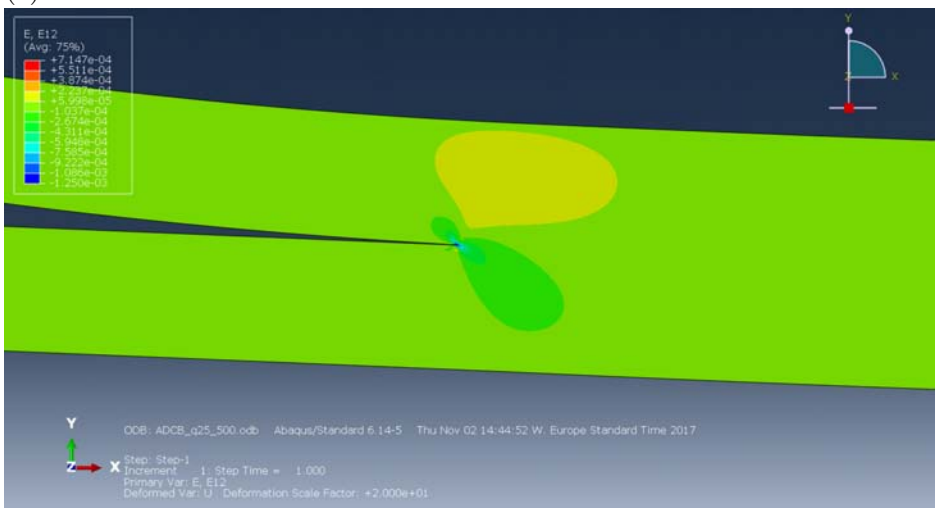

(*c*)

Figure A.6: FRMM, axial (*a*), vertical (*b*) and shear (*c*) strains, respectively ϵ_{xx}, ϵ_{yy} and ϵ_{xy}.

A.4 AFRMM (damage)

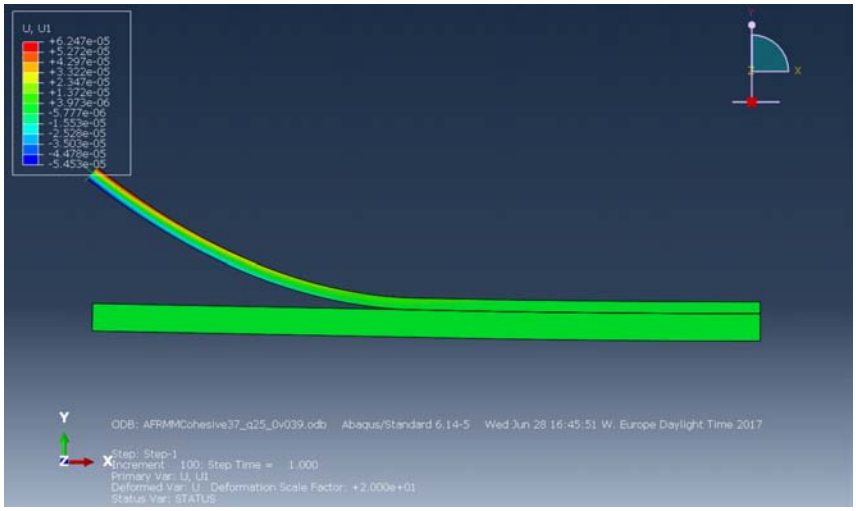

(*a*)

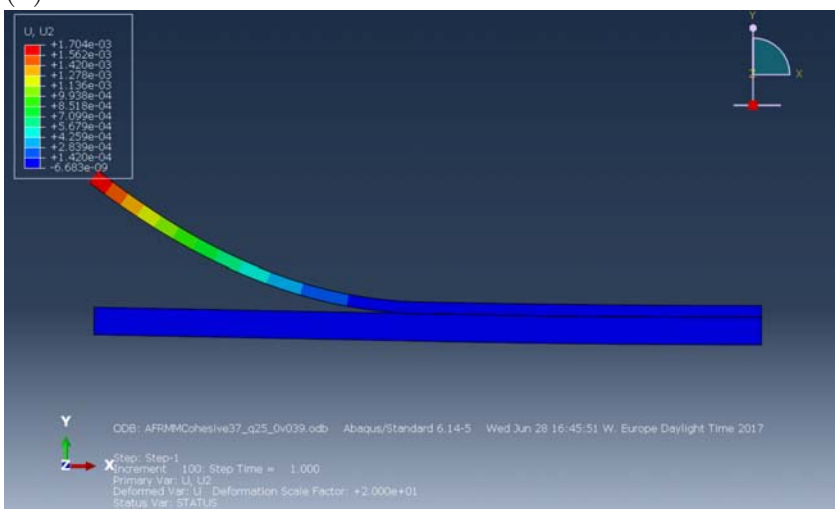

(*b*)

Figure A.7: AFRMMCoh, displacements in the x (horizontal) direction u_x (a) and in the y (vertical) direction u_y (b).

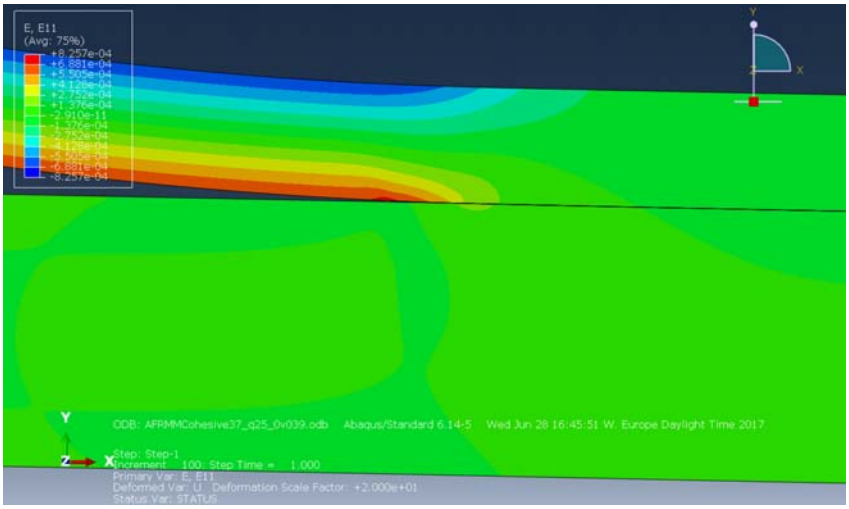

(*a*)

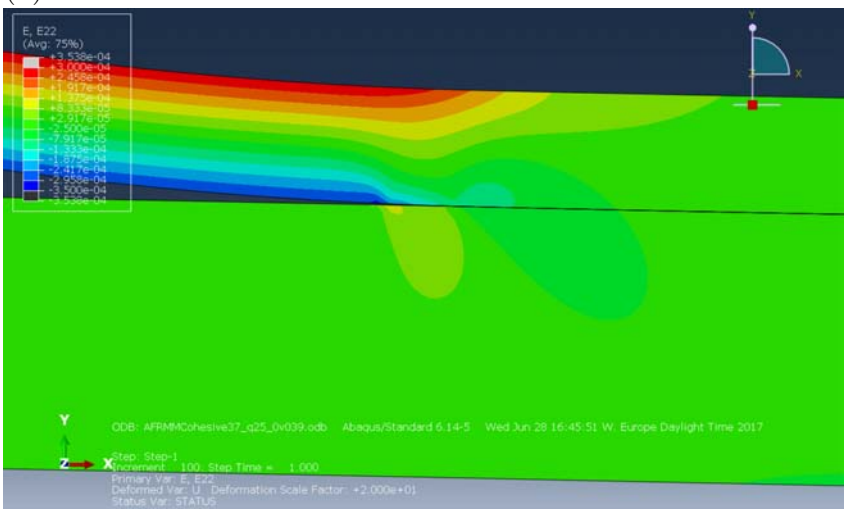

(*b*)

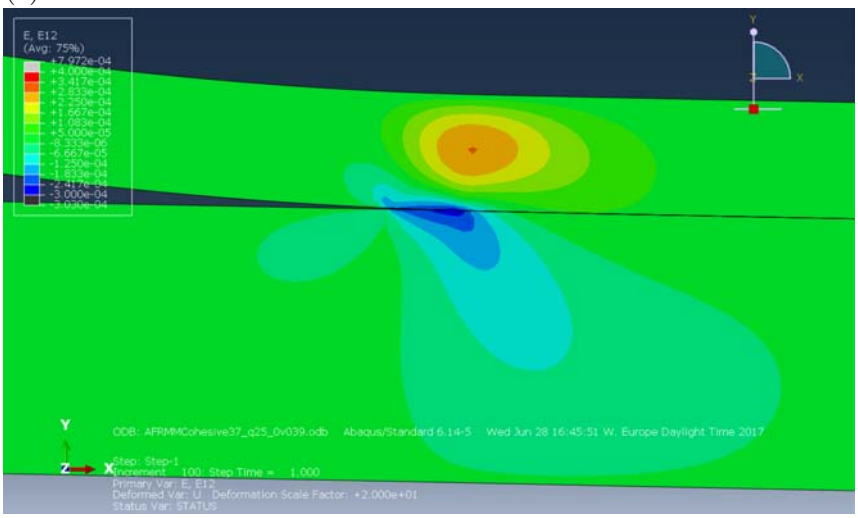

(*c*)

Figure A.8: AFRMMCoh, axial (*a*), vertical (*b*) and shear (*c*) strains, respectively ϵ_{xx}, ϵ_{yy} and ϵ_{xy}.

Appendix B

FRMM ABAQUS Model Using Cohesive Elements

Many tutorials are available on internet for modelling zero thickness cohesive elements in 3D geometries. Also for 2D cases there is a lot of material regarding the modelling of cohesive elements, but no informations were found regarding how to set them to be zero thickness. It is important to notice, however, that having zero thickness is only for visual reasons, which means that it won't affect the numerical solution. In fact, when the stiffness of the element is set (see §3.7), a thickness of 1 is assumed regardless of the physical thickness. Anyway, having zero thickness cohesive elements simplify the handle of the data in the MATLABcode, since it is not necessary to change the node coordinates (i.e. translate the top beam down until it "touches" the bottom one).
This Appendix provides a step by step tutorial for modelling a 2D FRMM geometry using zero thickness cohesive elements. Of course the same procedure can be used to model the various AFRMM geometries; it is sufficient to change the coordinates that are input at the beginning when creating the part.

B.1 Creating the Parts

B.1.1 Bar

The first part that is created is a cracked bar which includes the top beam, the bottom beam and the cohesive layer. In this case, the initial (physical) thickness of the cohesive layer is set to be 0.001 in order to be able to see it easily in the pictures. To create the bar:

- set the module to be part (Module: Part);
- in the top menu go to Part → Create and set: name "bar", modelling shape "2D planar", type "deformable", base feature "shell" and approximate size "1" → "Continue";

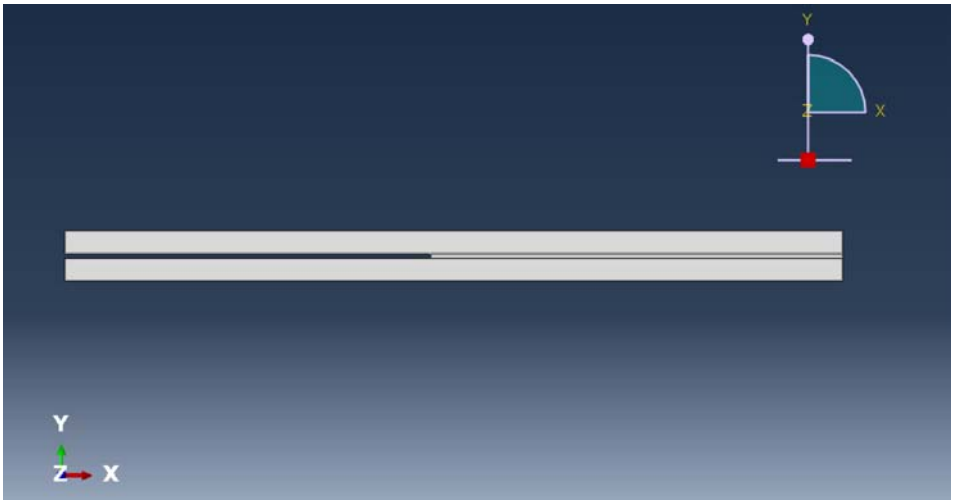

Figure B.1: Cracked bar, we can see the layer which will be later set to be cohesive

- click the icon "create lines: connected" and input the following coordinates: (0,0), (0,-0.005), (0.17,-0.005), (0.17,0.006), (0,0.006), (0,0.001), (0.08,0.001), (0.08,0) and (0,0) and click "Done";

- click the icons "partition face: sketch" → "create lines: connected" and input (-0.007,0.0005) and (0.0825,0.0005) → "create lines: connected";

- click the icons "partition face: sketch" → "create lines: connected" and input (-0.007,-0.0005) and (0.0825,-0.0005) → "create lines: connected" and click "Done".

The result should be like the one in Figure B.1. The bar is created and is partitioned into three parts: the top beam, the layer and the low beam. This partition is necessary to assign different materials properties.

B.1.2 Rigid

The second part that is created is a zero thickness rigid element whose length is half the beam thickness (i.e. 0.005). This part will then be tied to the left edge of the top beam. A rotation will be applied to it and, through it, to the beam. To create the rigid part:

- set the module to be Part (Module: Part);

- in the top menu go to Part → Create and set: name "rigid", modelling shape "2D planar", type "discrete rigid", base feature "wire" and approximate size "1" → "Continue";

- click the icon "create lines: connected" and input (0,0) and (0,0.005) and click "Done";

B.2 Materials and Sections

B.2.1 Define the Materials

The bar is constituted of two materials: the steel (top and bottom beams) and the cohesive material (layer between the beams). To define the properties of the steel:

- set the module to be property (Module: Property);
- in the top menu go to Material → Create and set the name to be "steel" → "Continue";
- in the new window that is opened go to "Mechanical" → "Elasticity" → "Elastic" and set: Young's Modulus "210e9" (210 GPa) and Poisson's Ratio "0.3", click "Ok".

To define the properties of the cohesive material:

- set the module to be property (Module: Property);
- in the top menu go to Material → Create and set the name to be "cohesive" → "Continue";
- in the new window that is opened go to "Mechanical" → "Elasticity" → "Elastic", set the type "traction" and input the penalty stiffnesses: E/E_{nn} "1e15" ($10^{15}Pa$), G_1/E_{ss} "1e15" and G_2/E_{tt} "1e15" (Figure B.2 (a));
- in the same window go to "Mechanical" → "Damage for traction separation laws"→ "Quads damage" and input the maximum stresses: nominal stress normal mode "30e6" ($30MPa$), nominal stress first direction "30e6" and nominal stress second direction "30e6" (Figure B.2 (b));
- still in the same window go to "Suboptions" → "Damage evolution", modify the type into "energy" and set the fracture energy to be "200" ($200J/m^2$), click "Ok" (Figure B.2 (c)) and "Ok" again (Figure B.2 (d)).

B.2.2 Define the Sections

Once the materials are defined it is necessary to create the sections, one for each material. Let's create first the steel section:

- set the module to be property (Module: Property);
- in the top menu go to Section → Create and set: name "steelSec", category "solid" and type "homogeneous" → "Continue";
- in the new window that is opened choose the material "steel" and click "Ok".

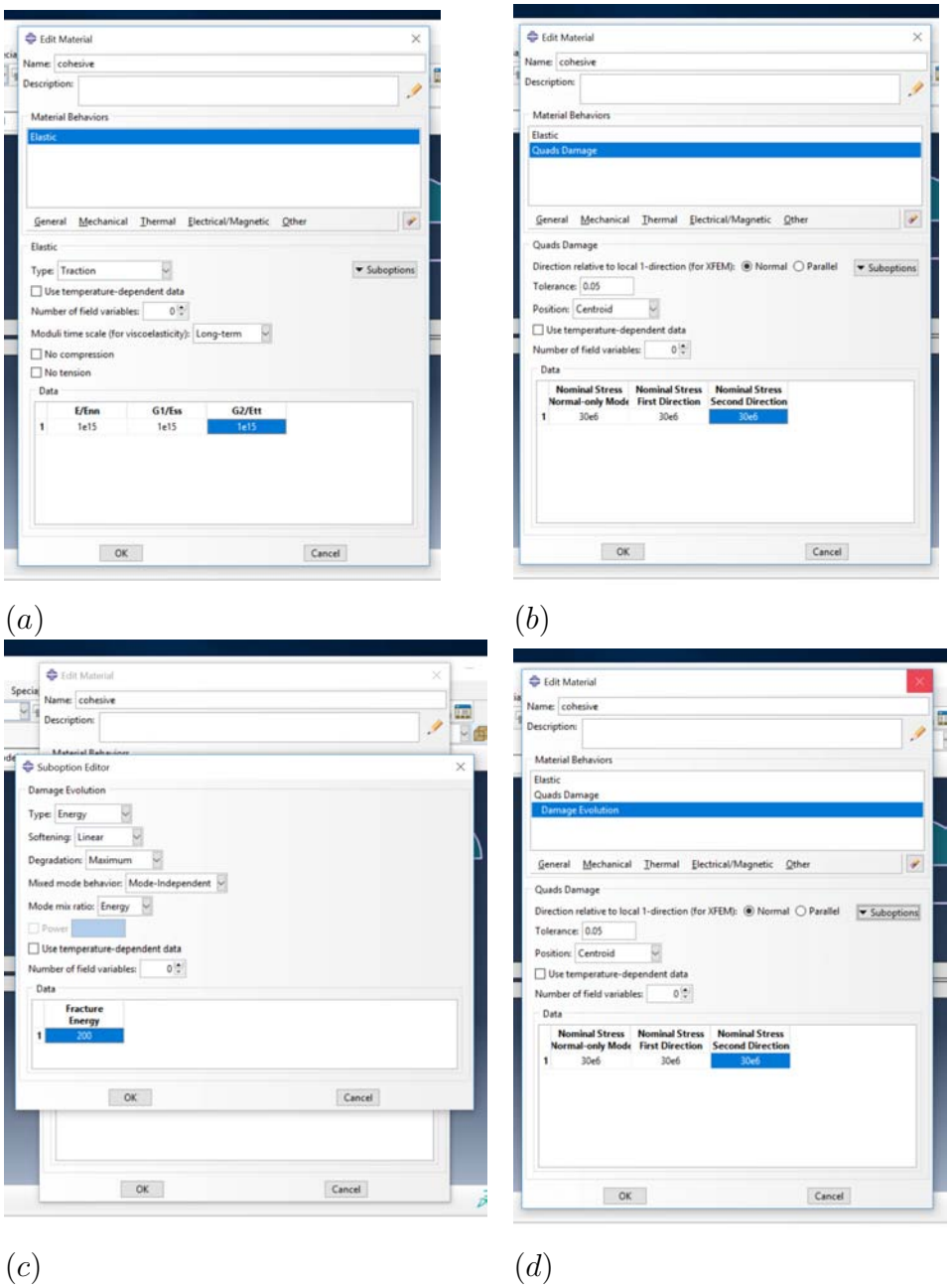

Figure B.2: Steps that need to be followed in order to assign the properties to the cohesive layer. Penalty stiffnesses (a), maximum stresses (b), energy control for damage evolution (c) and final window (d).

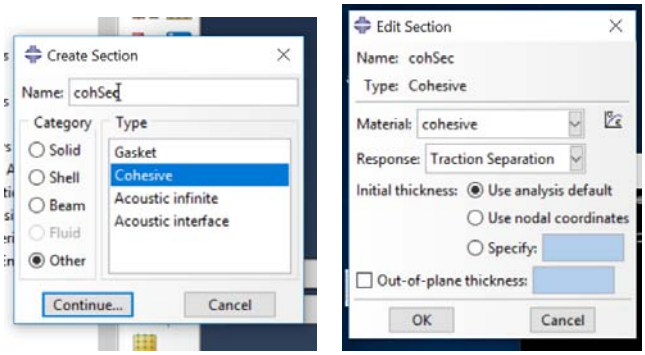

(*a*) (*b*)

Figure B.3: Cohesive section. Set the type as "cohesive" (*a*) and the response as "traction separation" (*b*).

We create now the section for the cohesive material:

- set the module to be property (Module: Property);
- in the top menu go to Section → Create and set: name "cohSec", category "other" and type "cohesive" → "Continue" (Figure B.3 (*a*));
- in the new window that is opened choose: material "cohesive", response "traction separation" and initial thickness "use analysis default", finally click "Ok" (Figure B.3 (*b*)).

B.2.3 Assign the Sections

Once the sections are defined it is necessary to assign them to the parts. In this case the steel section is assigned to the top and bottom bar of the part "bar":

- set the module to be property (Module: Property);
- in the top menu go to Assign → Section and select the upper and lower beam, then click "Done";
- in the window that is opened define the section to be "steelSec" and the thickness "from selection", click "Ok" and then "Done".

To assign the cohesive section to the central partition repeat the steps before but in the window select the layer between the beams and choose the section "cohSec". When defining a cohesive material it is important to specify a material orientation:

- set the module to be property (Module: Property);
- in the top menu go to Assign → Material Orientation and select the layer between the beams, click "Done" and then "Use Default Orientation or Other Method";

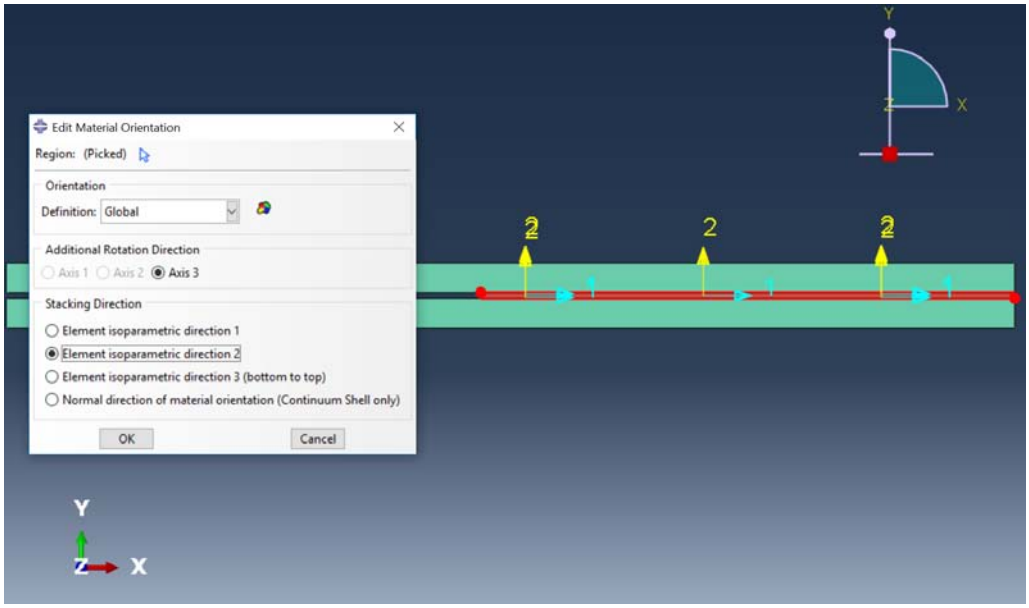

Figure B.4: Assign material orientation to the cohesive layer.

- in the window that is opened set: orientation definition "global", additional rotation direction "axis 3" and stacking direction "element isoparametric direction 2" (Figure B.4), click "Ok" and "Done".

B.3 Mesh

B.3.1 Mesh the Bar

Defining the proper mesh size and feature is of great importance. In particular, since it is better that the cohesive layer contains only one element across its thickness the mesh size is set to be equal to the physical thickness of the layer (in this case 0.001). First of all we define the mesh control:

- set the module to be mesh (Module: Mesh);
- in the top menu go to Mesh → Control and select the whole beam, click "Done";
- in the window that is opened set element type "quad" and technique "sweep", click "Ok" and then "Done".

It is important to define the technique "sweep" in order to be able, later, to edit the mesh of the top beam (i.e. translate it downwards to create the zero thickness layer). More, the sweep technique is used because the length of the cohesive elements is orientation- dependent [34]. After this we define the element type that is different for the beams and the cohesive layer. Regarding the beams:

- set the module to be mesh (Module: Mesh);

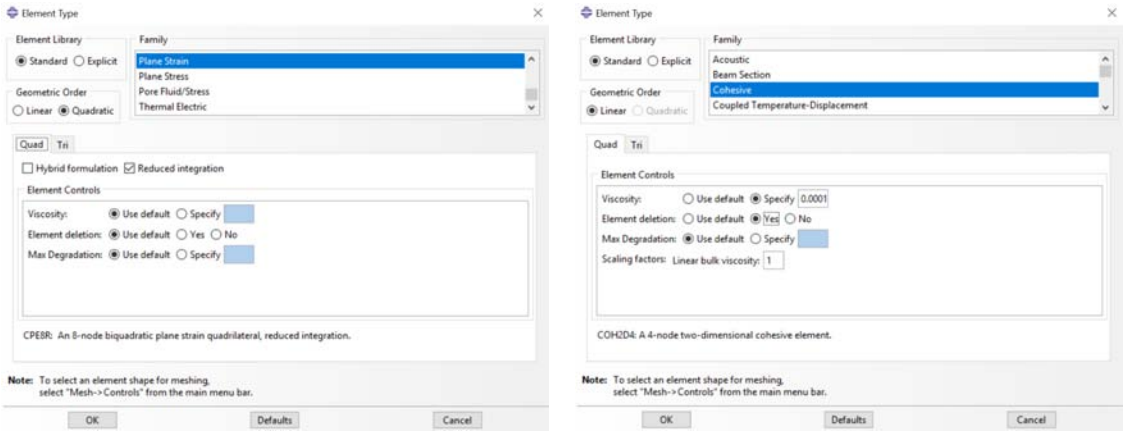

(*a*) (*b*)

Figure B.5: Set the element type. The family is "plain strain" for the beam (*a*) and "cohesive" for the cohesive layer (*b*).

- in the top menu go to Mesh → Element Type, select the upper and lower beam, then click "Done";
- a window called "element type" is opened. Set: element library "standard", geometric order "quadratic", family "plain strain", quad "reduced integration" and leave the rest as default (Figure B.5 (*a*)), click "Ok", "Yes" and "Done".

It is of particular importance to set the geometric order as quadratic in order to reduce the computational error. Regarding the cohesive layer:

- set the module to be mesh (Module: Mesh);
- in the top menu go to Mesh → Element Type, select the layer between the beams, then click "Done";
- a window called "element type" is opened. Set: element library "standard", geometric order "linear", family "cohesive", quad-element controls-viscosity "1e-4", quad-element controls-element deletion "yes" and leave the rest as default (Figure B.5 (*b*)), click "Ok", "Yes" and "Done".

The behaviour of the cohesive elements is corrected by defining the value 0.0001 for the viscosity in order to reduce the number of steps toward convergence[26]. It is also important that, once an element is broken, it deletes (crack propagation); that's why we asked for element deletion. To define the mesh size and mesh the part:

- set the module to be mesh (Module: Mesh);
- in the top menu go to Seed → Part and specify sizing control "0.001" (rest as default), click "Apply" and "Ok";

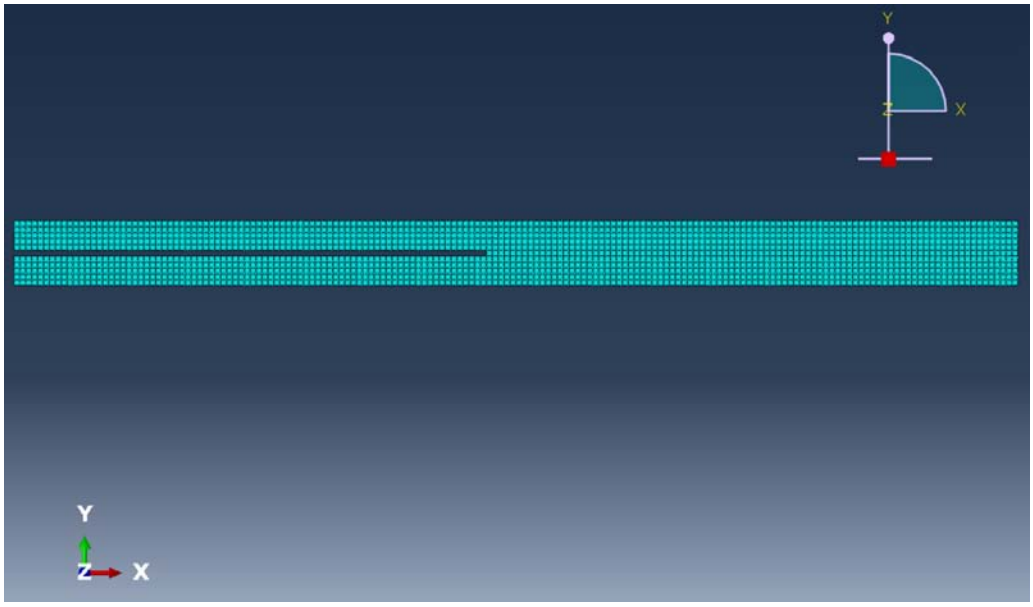

Figure B.6: The bar as it looks like once it has been meshed.

- go then to Mesh → Part and click "Ok".

At the end the result should be as in Figure B.6.

B.3.2 Mesh the Rigid Element

Since we don't care about the size of the elements of the part "rigid", we can use the default one:

- set the module to be mesh (Module: Mesh);
- go then to Mesh → Part and click "Ok".

B.3.3 Surfaces

After having created the mesh we define the surfaces: one for the rigid element and one for the bar. While the first is defined by the geometry, the second is defined by the mesh. That's why it wasn't possible to define it before. For the surface which belongs to the rigid element:

- set the module to be Part (Module: Part);
- in the menu that is int left side of the screen, double click on Surfaces, in the window that is opened enter the name "rigid2top", click "Continue", select the rigid element and click "Done";
- at this point two arrows of different colour appear, click on the colour of the arrow that is on the right side of the rigid element.

Regarding the surface which belongs to the bar:

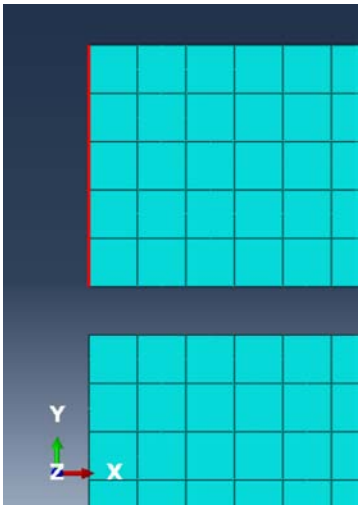

Figure B.7: The "top2rigid" surface is marked with a red line.

- set the module to be Part (Module: Part);
- in the menu that is int left side of the screen, double click on Surfaces, in the window that is opened enter the name "top2rigid" and select the type "mesh" → "Continue", select the surface (Figure B.7) and click "Done"

B.4 Steps and the Output Requests

To create the step for applying the rotation:

- set the module to be Step (Module: Step);
- in the menu that is int left side of the screen, double click on Steps, in the window that is opened enter: name "step1", procedure type "general" and select "static, general", click "Continue";
- a window called "edit step" is opened. Leave everything as default (nlgeom: "off") except in incrementation: modify the number of increments to "1000" and change the initial and maximum increment size into "0.01" (Figure B.8) and click "Ok".

Since the field data from ABAQUS will be used in the MATLAB code, it is necessary to modify the field output requests in order to get also the nodal coordinates x and y for each value of the displacement, strain and stress field. To do this:

- set the module to be Step (Module: Step);
- in the menu that is in the left side of the screen, double click on F-output-1, in the window that is opened leave everything as default and in addition tick: in volume/thickness/coordinates "COORD, current nodal coordinate" and in state/field/user/time "STATUS, status (some failure and plasticity models; VUMAT)" (Figure B.9) and click "Ok".

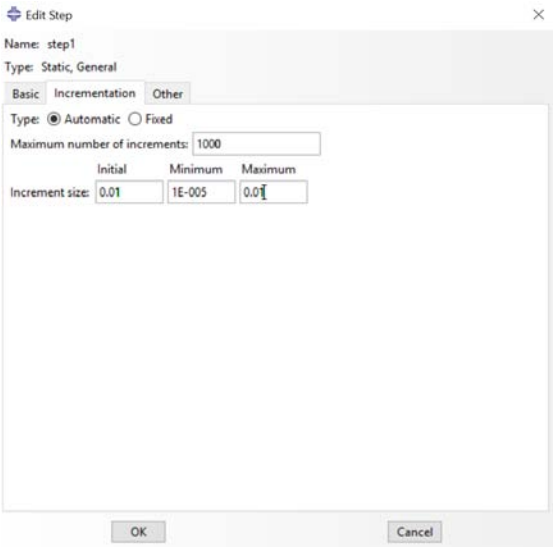

Figure B.8: In order get convergence when the job is run, it is necessary to edit the step by modifying the number of increments and the initial an maximum increment size.

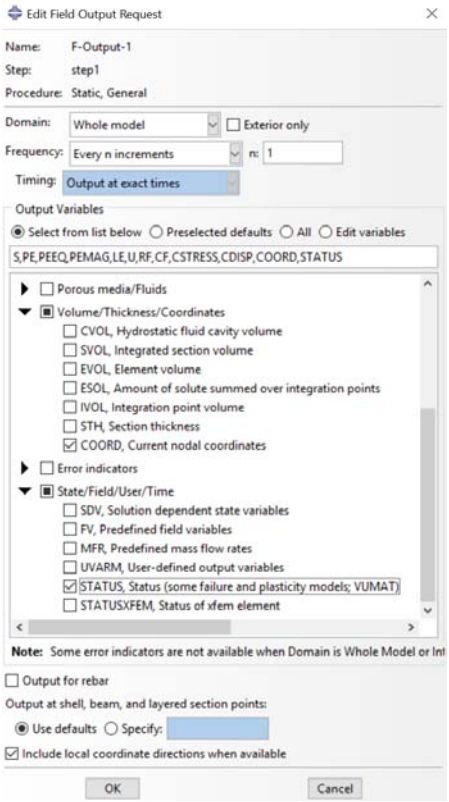

Figure B.9: In the "field output request" window we tick "COORD, current nodal coordinate" and "STATUS, status (some failure and plasticity models; VUMAT)" in order to have the coordinates values (x and y) in the output file and cohesive elements delation when the crack propagates respectively.

B.5 Assembly

B.5.1 Create the Assembly

Now that we have all the parts that we need we can create the assembly:

- set the module to be Assembly (Module: Assembly);
- in the menu that is in the left side of the screen, double click on Instance, in the window that is opened select "bar", click "Apply", select "rigid" and click "Ok";
- in the top menu go to "Constraint" → "Coincident Point", select the point of the bar whose coordinates were (0,0.001) and then the point of the rigid element whose coordinates were (0,0).

B.5.2 Create the Constraint

Now that we have created the assembly we can tie the rigid element to the top left part of the bar by using the surface that we have defined in B.3.3.

- set the module to be Interaction (Module: Interaction);
- in the top menu go to Constraint → Create, set name "constr" and set the type "tie", click "Continue";
- select as master surface "top2rigid" and as slave surface "rigid2top", click "Ok".

B.5.3 Edit the Mesh

As last thing before setting the boundary conditions/applying the loads we have to translate the mesh of the top beam downward to get zero thickness cohesive elements. To do this:

- go to the part bar and set the module to be Mesh (Module: Mesh);
- in the top menu go to Mesh → Edit, in the window that is opened choose category "node" and method "edit", select all the nodes which belongs to the upper beam (Figure B.10 (*a*)) and click "Done";
- in the window "edit nodes" define the offset 2 as the opposite of the initial thickness of the cohesive layer, in this case "-0.001" and untick "project to geometry" (Figure B.10 (*b*)), finally click "Apply";
- go then to the module Assembly, in the left menu, right click in Instance → Regenerate.

The result should be as in Figure B.10 (*c*).

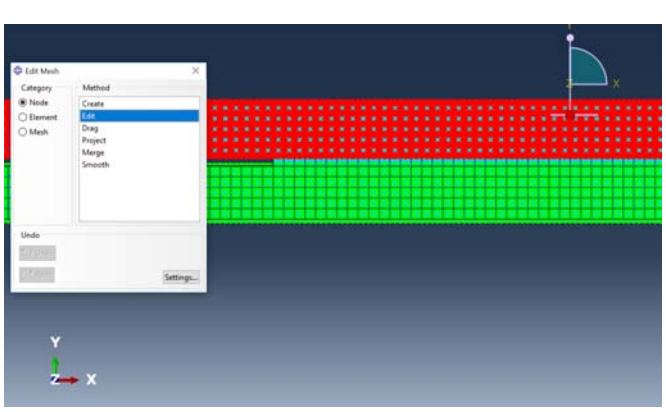

(a)

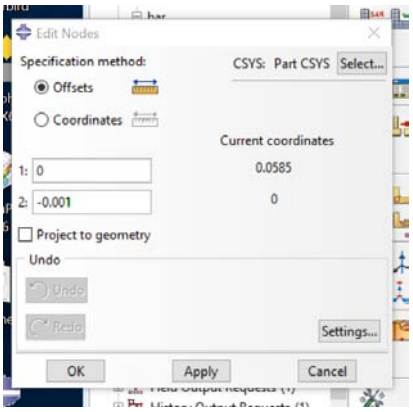

(b)

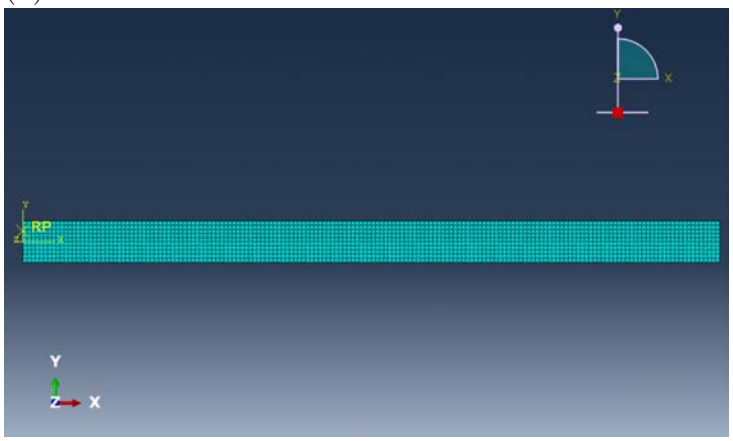

(c)

Figure B.10: Steps that needs to be followed to "squeeze" the cohesive layer. Edit the mesh (a), define an offset (b) and final result (c).

B.6 Boundary Conditions

As last thing before creating the job and running it we define the boundary conditions and we apply the loading. In particular we have to fix the right edge of the beam and we have to apply a clockwise rotation to the rigid element (and therefore to the beam since they are tied). Let's first fix the right edge of the beam:

- set the module to be Load (Module: Load);
- in the top menu go to BC → Create, set: name "BC", step "step1", category "mechanical" and the type for selected step "symmetry/antisymmetry/encastre", click "Continue";
- in the window select the right edge of the beam (Figure B.11 (a)), click "Done";
- int the new window that is opened choose "ENCASTRE" and click "Ok".

Finally the result is as in Figure (Figure B.11 (b)). In this phase it is important to select only the right edge of the steel beams and not the right edge of the cohesive layer otherwise an error might occur when running the job.
We now apply the rotation to the rigid element:

- set the module to be Load (Module: Load);
- in the top menu go to BC → Create, set: name "BC", step "step1", category "mechanical" and the type for selected step "displacement/rotation", click "Continue";
- in the window select the reference point (RP) of the rigid element, click "Done";
- int the new window that is opened tick "UR3", type for example "-0.06" and click "Ok".

B.7 Job and Results

Now that the model is complete, the last thing to do is to create the job and run it:

- set the module to be Job (Module: Job);
- in the top menu go to Job → Create, give a name to the job (for example "job1") and select the model that we have created, then click "Ok";
- in the top menu go to Job → Submit → job1 and wait until the processing finishes.

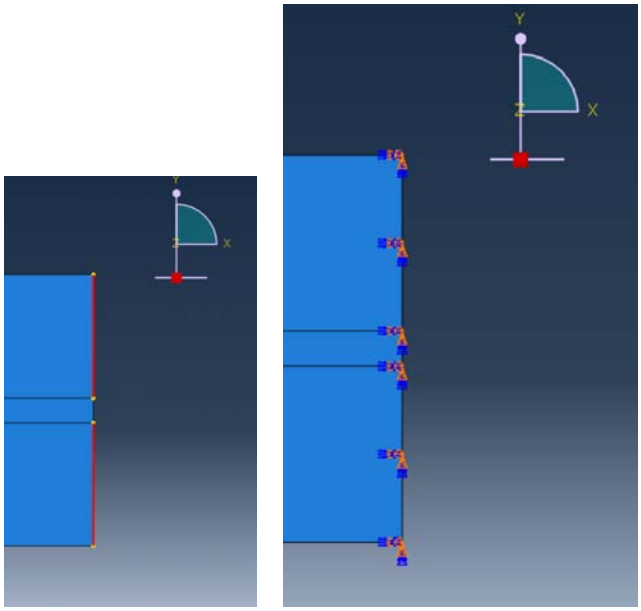

(*a*) (*b*)

Figure B.11: Surfaces to be constrained before (*a*) and after (*b*) applying the boundary conditions.

To visualise the results:

- set the module to be Job (Module: Job);
- in the top menu go to Job → Results → job1, the module authomatically changes to Visualization;
- to plot the results, in the top menu go to Plot → Contours → On deformed shape.

By applying a rotation of -0.06 radians the crack propagates in the x direction for 44 *mm*. A detail of the crack tip at the end of the propagation is shown in Figure B.12. In particular the axial strain is depicted. We can notice that the cohesive elements above the crack tip are stretched, which means that damage is occurring[1].

[1]Please note that the deformation that is shown is about four times higher than the real one.

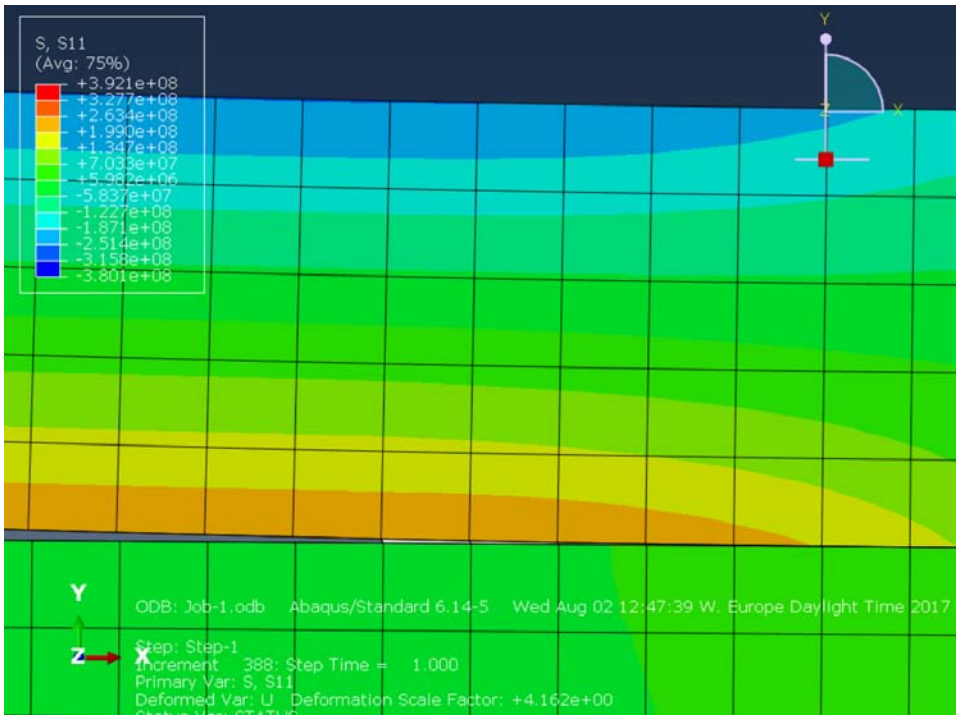

Figure B.12: Result of the model, the axial stress is depicted. We can notice that the cohesive elements are stretched at the crack tip. The scaling factor is around 4.

Appendix C

Nomenclature: Letters, Symbols and Acronyms

C.1 English Alphabet

a_0	Initial crack length $[m]$
a_e	Correction factor $[m]$
$AFRMM$	Asymmetric Fixed Ratio Mixed Mode
B	beam's width $[m]$
CBT	Corected Beam Theory
$CFRP$	Carbon Fibre Reinforced Plastics
$COH2D4$	Linear cohesive elements, 2D
$CPE8R$	Quadratic elements, plain strain, 2D
CZM	Cohesive Zone Model
DCB	Double Cantilever Beam
DIC	Digital Image Correlation
ds	Infinitesimal portion of Γ $[m]$
E	Young's modulus $[Pa]$
ELS	End Loaded Split
ERR	Energy Release Rate $[J/m^2]$
F	Correction Factor
$FRMM$	Fixed Ratio Mixed Mode
FRP	Fibre Reinforced Plastics
G	Energy release rate $[J/m^2]$
G_{ANA}	Energy release rate calculated via an analytical formula $[J/m^2]$
G_I	Mode I energy release rate $[J/m^2]$
G_{IC}	Mode I fracture toughness $[J/m^2]$
G_{II}	Mode II energy release rate $[J/m^2]$
G_{IIC}	Mode II fracture toughness $[J/m^2]$
$G_{I/II}$	Mixed mode energy release rate $[J/m^2]$
$2h$	Total thickness of the beam $[m]$
h_1	Thickness of the upper beam $[m]$

h_2	Thickness of the lower beam $[m]$
I	Second moment of area of half uncracked beam $[m^4]$
I_1	Second moment of area of the upper beam $[m^4]$
I_1	Second moment of area of the lower beam $[m^4]$
J	Energy release rate as computed via the J-Integral $[J/m^2]$
J_I	Mode I energy release rate as computed via the mode decomposed J-Integral $[J/m^2]$
J_{II}	Mode II energy release rate as computed via the mode decomposed J-Integral $[J/m^2]$
K_N	Penalty stiffness in the normal direction $[Pa]$
K_S	Penalty stiffness in the shearing direction $[Pa]$
$LEFM$	Linear Elastic Fracture Mechanics
M_1	Moment applied to the upper beam $[Nm]$
M_2	Moment applied to the lower beam $[Nm]$
M_C	Moment required to apply an ERR equal to the fracture toughness $[Nm]$
M_I	Moment causing pure opening
M_{II}	Moment causing pure shearing
N	Correction factor
n_j	Outward unit vector normal to Γ
P	Load $[N]$
R	Material's resistance to fracture $[J/m^2]$
S	Surface containing the crack tip, 3D
$SACA$	Semi Analytical Cohesive Analysis
SBT	Simple Beam Theory
T_i	Traction vector $[Pa]$
t_{NC}	Stress for damage initiation under pure mode I $[Pa]$
t_{SC}	Stress for damage initiation under pure mode II $[Pa]$
UCD	University College Dublin
u_i	Displacement vector $[m]$
U_s	Strain energy $[J]$
U_e	External work $[J]$
w	Strain energy density $[J/m^3]$

C.2 Greek Alphabet

Γ	Contour containing the crack tip, 2D (integration path for the J-Integral)
Δ_I	Correction factor $[m]$
ϵ_{ij}	Strain tensor
ϑ_C	Angle that causes crack propagation $[rad]$

ρ	Density $[kg/m^3]$
ν	Poisson's ratio
σ	Material's resistance $[Pa]$
σ_{ij}	Stress tensor $[Pa]$

Bibliography

[1] Jones, Robert Millard (1999), *Mechanics of Composite Materials*, Taylor & Francis, Philadelphia.

[2] Sellers, Terry Jr. (1985), *Plywood and Adhesive Technology*, Marcel Dekker, Inc., New York.

[3] Verhoeven, John (2007), *Pattern Formation in Wootz Damascus Steel Swords and Blades*, Indian Journal of History of Science.

[4] Kaw, Autar K. (2006), *Mechanics of Composite Materials*, Taylor & Francis Group, New York.

[5] `https://www.infosys.com/engineering-services/white-papers/Documents/carbon-composites-cost-effective.pdf`.

[6] Donaldson, Steven M. and Miracle, Daniel B. (2001), *ASM Handbook*, Volume 21: *Composites*, ASM International.

[7] `https://www.ihs.com/pdf/Composites-Aerospace-Applications-whitepaper_264558110913046532.pdf`

[8] Kalpakjian, Serope and Schmid, Steven R. (2009), *Manufacturing Engineering and Technology*, Pearson.

[9] Roeseler, William G.; Sarh, B. and Kismarton, Max U., The Boeing Company (2007), *Composite Structures: The First 100 Years*, 16th International Conference on Composite Materials, Kyoto.

[10] `http://aerospaceengineeringblog.com/composite-materials-wind-energy/`.

[11] Mohan, Joseph D. (2010), *An Investigation of Composite-to-Composite Bonding*, PhD Thesis.

[12] Conroy, Mark (2015), *Mixed Mode Fracture in Fibre Reinforced Polymer Composites*, PhD Thesis.

[13] Williams, J. G. (1984), *Fracture Mechanics of Polymers*, Ellis Horwood Ltd.

[14] Williams, J. G. (1988), *On the Calculation of Energy Release Rates for Cracked Laminates*, International Journal of Fracture.

[15] Dillard, D. A.; Singh, H. K.; Pohlit, D. J. and Starbuck, J. M. (2009), *Observations of Decreased Fracture Toughness for Mixed Mode Fracture Testing of Adhesively Bonded Joints*, Journal of Adhesion Science and Technology.

[16] Suo, Z. and Hutckinson, J. W. (1990), *Interface Crack Between Two Elastic Layers*, International Journal of Fracture.

[17] Rice, J. R. (1968), *A Path Indipendent Integral and the Approximate Analysis of Strain Concentration by Notches and Cracks*, Journal of Applied Mechanics.

[18] Weinberger, C.; Cai, W.; Barnett, D. (2005), *Lecture Notes - Elasticity of Microscopic Structures* `http://micro.stanford.edu/~caiwei/me340b/content/me340b-notes_v01.pdf`.

[19] Anderson, T. L. (2005), *Fracture Mechanics. Fundamentals and Applications*, Taylor & Francis Group.

[20] Ishikawa, H.; Kitagawa, H. and Okamura, H. (1980), *J Integral of a Mixed Mode Crack and its Application*, ICM 3, Volume 3.

[21] ISO 15024:2001. Fibre-reinforced plastic composites. Determination of mode I interlaminar fracture toughness, G_{IC}, for unidirectionally reinforced materials.

[22] ISO 15114:2014. Fibre-reinforced plastic composites. Determination of mode II fracture resistance for unidirectionally reinforced materials using the calibrated end-load split (C-ELS) test and an effective crack length approach.

[23] Moore, D. R.; Pavan, A. and Williams, J. G. (2001), *Fracture Mechanics Testing Methods for Polymers, Adhesives and Composites*, Elsevier Science, Amsterdam.

[24] Demirdzic, I.; Ivankovic, A. and O'Dowd, N., *Lecture Notes for the Course "Computational Continuum Mechanics (CCM)"*, University College Dublin (UCD).

[25] `http://abaqus.software.polimi.it/v2016/books/usb/default.htm?startat=pt06ch32s05abo29.html`.

[26] *Lecture Notes of the Course "Modelling Fracture and Failure with* ABAQUS*"*, Technische Universität Graz (TU Graz), 2005.

[27] Brewer, J. C. and Lagace P. A. (1988), *Quadratic Stress Criterion for Initiation of Delamination*, Journal of Composite Materials.

[28] `http://www.hexcel.com/user_area/content_media/raw/HexPly_8552_eu_DataSheet.pdf`

[29] *Product-Manual: StrainMaster*, Item-Number(s): 1003017, LaVision, 2015.

[30] Larma, Marijana (2016), *Application of Digital Image Correlation to Determine Mode Partitioning in Mixed-Mode Fracture of Composite Structures*, Master Thesis.

[31] *Product-Manual: StrainMaster DIC*, Item-Number(s): 1010086, LaVision, 2016.

[32] Mazzoleni, Paolo (2013), *Uncertainty Estimation and Reduction in Digital Image Correlation Measurments*, PhD Thesis.

[33] Xian, W. and Shaopeng, M. (2014), *A Short Image Series Based Scheme for Time Series Digital Image Correlation*, Computing Research Repository.

[34] Barbero, E. J. (2013), *Finite Element Analysis of Composite Materials Using Abaqus*, CRC Press, Taylor & Francis Group.